POLITECNICO DI TORINO

Corso Di Laurea Magistrale In Ingegneria Meccanica

Tesi di Laurea Magistrale

Reliability of Digital Image Correlation methods applied to additive manufactured metallic lattice components

Affidabilità dell'applicazione di metodi di Digital Image Correlation a componenti reticolari metallici prodotti per fabbricazione additiva

Relatore:
Prof. Aldo Canova

Candidato:
Fabio Perlini

Anno Accademico 2019/2020

Abstract

Additive manufacturing (AM) technologies went from being used in the early pre-production and prototyping stages to the main production step in many engineering applications, due to the great design freedom introduced, allowing the creation of components provided with shapes and feature otherwise impossible to produce using traditional subtractive technologies. In this class of features great importance have the lattice structures, which are reticular features comprised of multiple beam of different shapes and arrangements. These are used to create components developed to accomplished specialized task, like heat exchanger and bio-compatible meta-material for prosthetic applications, or to reduce weight in already existing solid components. Due to these specialized uses, and to the high costs of both equipment and raw materials, AM is usually used to produce batches of few components or even single pieces.

These characteristics of both uniqueness and high costs discourage the application of testing techniques that could destroy or made unserviceable said components. As the name implies, Non-Destructive Testing methods (NDT) allow to implement these examinations without damaging the pieces. Inside this category of methods Digital Image Correlation (DIC) allow to acquire information of displacement and movement on a wide area of the component, using equipment composed of commonly used tools like digital cameras and workstations.

Due to the unique behavior of lattice components under stress the interest was focused on how the DIC can be used to acquire information derived from the experiments, and the accuracy of those information.

Using the scientific literature, the accuracy of the application of DIC methods to lattice components has been investigated, along with the preventive measure to adopt in order to obtain the best results possible. We observed a widespread use of the DIC in these applications, from the investigation of the behavior of existing components after optimization, to the small-scale analysis of meta-materials to the influence of the manufacturing parameters to the metallic microstructures.

In general, DIC is a widely applied technique, with results comparable to those of the twin destructive tests and used in many cases in conjunction with the latter to confirm the goodness of finite element models.

The precautions necessary to obtain the best results will be illustrated, from the preparation of the test environment (cleaning, illumination, vibration control) to the execution of the test (calibration, deformation speed and image acquisition speed) to the subsequent processing of the images.

Future development could involve the study of the combination of parameters and algorithm to be used to obtain the best results in specific applications.

Table of contents

1 Introduction

This paper explores the application of a visual testing technique, called Digital Image Correlation, to the study of lattice components produced using Additive Manufacturing technology, with particular interest in powder bed fusion of metallic materials.

Lattice components are parts made of lattice structures, meta-materials structured at the macroscopic and mesoscopic scales, composed of the combination of regular components, like beam, interconnected to create 3-D reticular structures. The resulting macroscopic behavior can be tailored to specific needs adjusting mesostructure parameters and arrangement of the unit elements. These structures are used for various purposes, from the reduction of weight in otherwise solid component, for the creation of prosthesis with part to be integrated into bones or for their shock absorption properties. Giving the internal complexity of these components, Additive Manufacturing technologies are a family of production processes well suited to produce them.

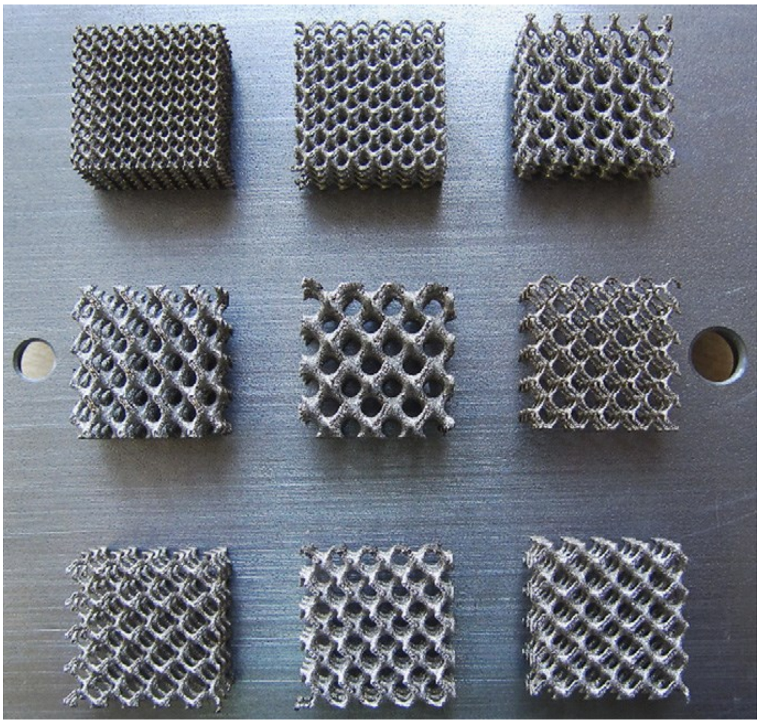

Figure 1.1 Examples of specimen with different lattice mesostructure configurations [1].

Additive manufacturing, also referred to as AM, is a relatively new fabrication technology characterized by the creation of components by the addition of material layer by layer, as opposed to conventional subtractive or formative techniques. It has evolved from the first applications as prototyping tool to the modern days, in which is used to build fully functional component for critical applications, like medical and aerospace, improving the personalization and the economic advantages of the production of small batches while reducing wastes, costs and energy consumption [2]. As will be better explained later in this paper, AM technologies refer to the process which produce a component through 3 main steps: first a computerized 3D solid model describing the components to be manufactured is developed, then exported to the AM machine and adapted to the building setup (changing orientation, position and scaling) and then the part is built layer by layer by the machine [2].

AM is having a big impact on the manufacturing industry, with some big advantages of this technology mostly found in the areas of customized healthcare, reduction of environmental impact for manufacturing sustainability and the simplification of the supply chain, leading to an increased efficiency and responsiveness in demand fulfillment [2].

In the health care industry for instance AM allows the production of customized surgical implants and assistive devices, being suited to produce customized components, resulting in improvements in safety, quality and effectiveness of healthcare for the general population. Compared to conventional machining processes AM is more efficient in terms of raw material consumption and water usage, and it does not require the use of coolant, producing less pollution. The reduction in energy consumption is still debated [3], giving the non-uniformity of the various approaches to evaluate it, but the prospects are promising. In addition, it can reduce significantly the need for warehousing, transportation and packaging, and have the potential to reduce the number of stages in the traditional supply chain offering the opportunities to redesign products with fewer components and to manufacture products near the customer.

An interesting and recent example is the quick manufacturing of a replacement valve for a medical reanimation ventilator device, after a shortage happened in a hospital in Brescia (Italy) during the COVID-19 pandemic [4]. The use of AM technology allowed to obtain fully functional components in short time, since the manufacturer could not provide them in time to replenish the stock. Using these replacements, the hospital continued to provide ventilation to critical patients. Figure 1.2 show the various steps leading to the final components. The original valve was reverse engineered into the first plastic FDM prototype made with an amateur equipment. For both health and accuracy reasons a professional manufacturer was involved, leading to the production of component made of a custom polyamide-based material, using a laser powder bed fusion process.

Figure 1.2 From the right: The reference model, the first FDM prototype, the PBF final products (in grey) [5] [6].

AM processes reduce the exposure of workers to health and occupational hazards caused by traditional manufacturing, like inhaling oil mist or occupational hearing losses, while creating a new family of potential health problems, related for instance to the handling, using and disposal of the raw materials. Some technologies, like Selective Laser Melting and the broad family of the powder bed fusion processes, are inherently less prone to these hazards, being these machines equipped with an isolated chamber in which the materials are processed. Still, specialized training is needed to ensure a safe production especially for the step of the process related to the handling of the raw material (some metallic powders are highly unstable and can ignite in presence of oxygen). For these reasons isolated containers are usually utilized for the transportation and handling too. Another big limitations are the initial costs of the machines (in the order of the hundreds of thousands of euros for big SLM systems) [7] and the raw powders, which have to be finely controlled in shape and dimensions.

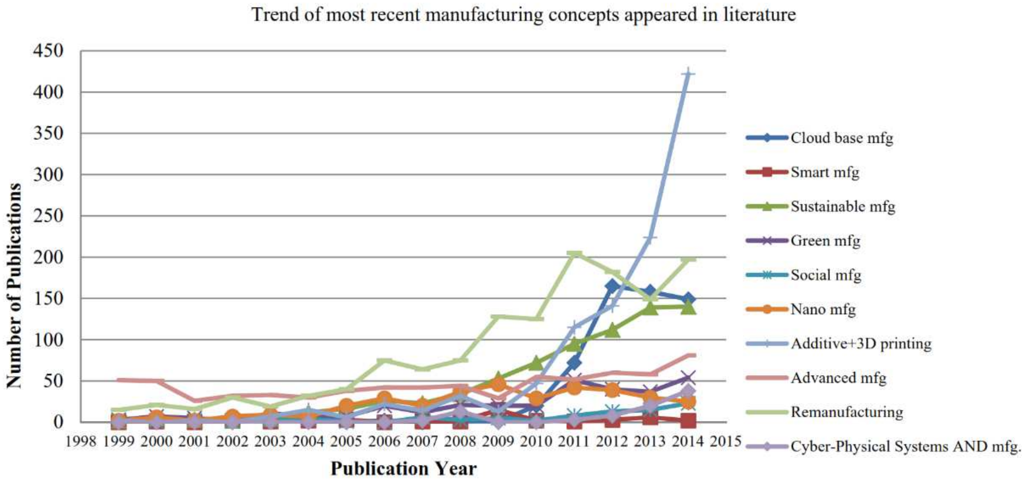

Figure 1.3 The number of publications found in Engineering Village, Compendex, Inspec & GEOBASE databases from 1999 to April 2015 with titles including one of the labels listed on the right [8].

Metal additive manufacturing is surrounded by and increasing interest [8], showing excellent perspectives of growth. The number of companies selling AM systems went from 49 in 2014 to 97 in 2016, amongst the 49% involved with metal AM. This technology has been predominantly used for research, prototyping or advanced applications in the aerospace industry. It is also used in defense and automotive industries [9]. Aerospace is a sector of engineering in which AM has proven great potential, with various application already existing. In February 2020 the European Space Agency unveiled that the 3D-printed thrust chamber assembly of the methane-fueled M10 rocket engine has passed its first series of hot firing tests [10]. This engine will power the upper stage of future Vega vector evolutions from 2025. The thrust chamber was built in two parts in Italy by Avio, using additive layer-by-layer manufacturing of metallic alloys.

ESA state that this technology enables more complex internal geometries to be built in fewer parts, reducing the need for additional machining, speeding up production times and cutting costs. Product inspection is a challenge, but NDT techniques can be used to detect potential obstructions within cooling channels, defects and geometry distortions. Test with subscale models carried out in 2018 demonstrate that AM produces thrust chambers that are comparable to those built in the traditional way and that NDT were successful in detecting defects during manufacturing.

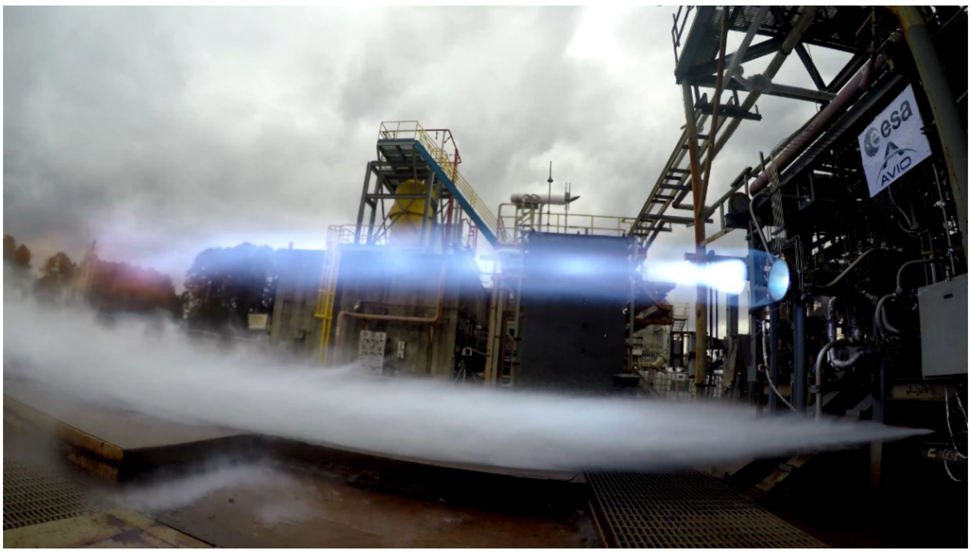

Figure 1.4 Still from a video showing the hot firing of the first full scale thrust chamber of the M10 engine at the Nasa Marshall Space Flight Center in Huntsville [11].

NDT, namely Non Destructive Testing, are a family of inspecting methods designed to leave the component intact after being tested. This definition includes a great amount of different techniques, ranging from the simple first-person visual inspection to computerized tomography. The main advantage of these methods is their ability to leave the components serviceable after testing, resulting in no losses of production. This is critical to AM components, due to the high costs and personalization of the part made with these technologies, especially for the metallic ones.

Inside the NDT family the focus of this paper is on the Digital Image Correlation (DIC), a digital optical method that employs tracking and image registration techniques for accurate 2D and 3D measurements of changes in images, used to measure full-field displacement and therefore strains by comparing different images taken during the evolution of the test. DIC is already utilized in various fields, such as fracture studies, material characterization and components behavior under stress, from atomic level to the monitoring of displacements of entire mountains [12]. Being a full field method DIC is particularly effective in the study of lattice components, in which the macroscopic and mesoscopic behaviors can drastically differ, to relate one to the other. The evaluation of the strain maps of the components allow to know the strain for the single strut, the mean of a certain area or the heterogeneities located on all the surface. One of the main advantages of the application of this technique to lattice specimens is that it only requires non-specialized equipment, like digital cameras and workstations, making it a relatively economic method of testing. As previously mentioned, reticular components may have drastically different behaviors from mesoscopic to macroscopic point of view, making it necessary to investigate these at multiple scales in order to achieve a global knowledge of their behavior.

This paper focus on how the literature describe the use of DIC to acquire information derived from experiments on lattice components, and how the results compare to traditional testing methods. Various researchers already utilized DIC to study the macroscopic and microscopic behavior of lattice components produced using AM, with different reticular patterns, materials and testing configuration. These results may integrate those coming from traditional testing like extensometers or replacing them entirely, for example when studying single struts extrapolated from a surface. With DIC virtual extensometer can be placed in different part of the analyzed images. Many finite elements models have been developed to predict the behavior of reticular structures, and DIC testing has been used to validate the results coming from those models.

Along with the comparison between DIC and traditional testing this paper illustrate the precaution found useful to obtain the best possible results. Being an optical method, the results depends on various parameters related directly to the test setup, such as the quality of the acquiring device, the illumination and cleaning, or related to the execution of the test, such as calibration and aperture.

2 Additive Manufacturing

2.1 Overview

Additive manufacturing is a rapidly increasing manufacturing technology capable of creating, in few hours and without the use of specialized tools, objects of complex geometry, directly from the 3D mathematical model designed on a CAD software.

Referred to in short as AM, the basic principle of this technology is that a model, generated using a three-dimensional Computer-Aided Design (3D CAD) system, can be fabricated directly without the need for process planning or specialized tools, allowing to significantly simplify the process of producing complex 3D objects directly from CAD data. In theory in order to produce good quality parts AM should need only some basic dimensional details and a small amount of understanding as to how the AM machine and process works and the materials that are used to build the part.

As hinted by its name, unlike the traditional machining process, the AM production is obtained adding material, usually layer by layer, instead of removing it, each layer being a thin cross-section of the part derived from the original CAD data. Because of the reality of the process and the material, each layer will have a finite thickness, so the resulting part will unavoidably be an approximation of the original data, and consequently the thinner each layer, the closer to the final part will be to the original. Every major AM commercial machine is based on a layer-by-layer technology, with differences in the materials that can be used, how the layers are created, and how the layers are bonded to each other. Such differences will determine factors like the accuracy of the final part plus its material properties and mechanical properties, and will also determine factors like the speed of the production process, the amount of post-processing needed, the size of the AM machine and the overall cost of the machine and process.

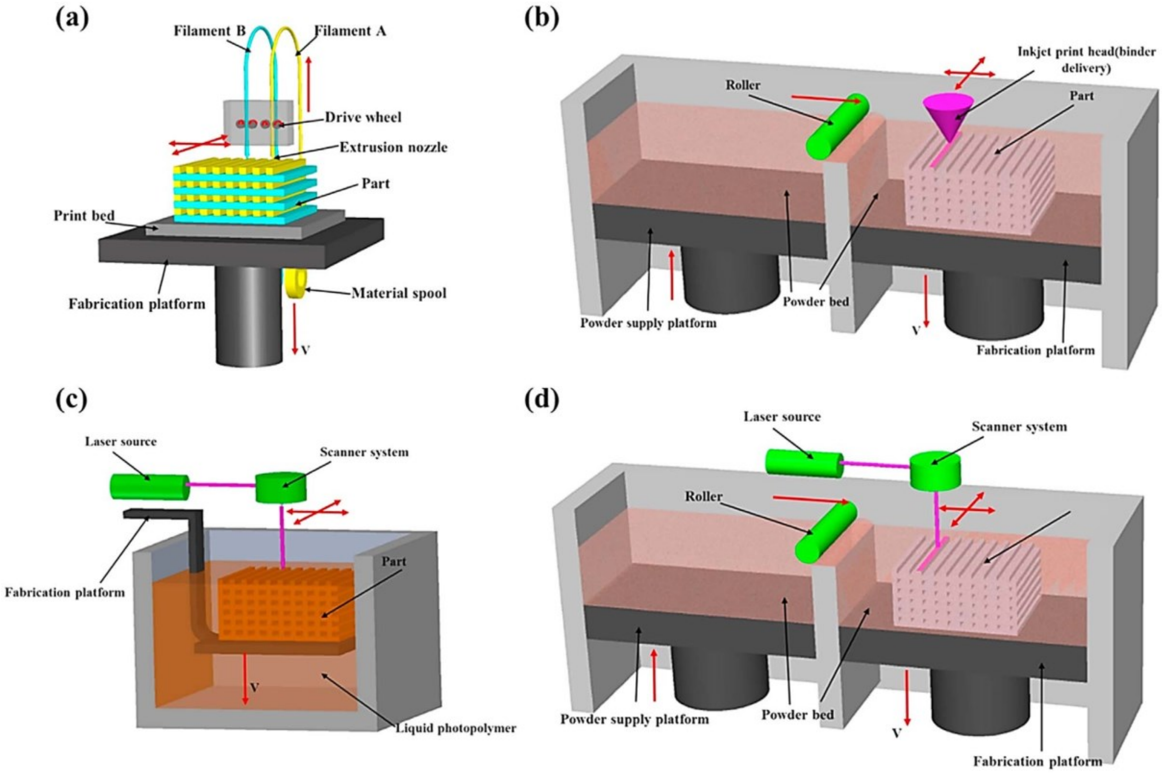

Figure 2.1 Schematic diagrams of four main methods of additive manufacturing: (a) fused deposition modelling; (b) inkjet printing; (c) stereolithography; (d) powder bed fusion [13].

As described in [14] most AM processes involve, to some degree at least, the following eight steps, which will be further explained later.

Step 1: CAD:

All AM parts start from a mathematical model that fully describes the external geometry. The model must be a 3D solid or surface representation of the object. This can either be obtained by the use of a CAD software or by reverse engineering of a previously existing part.

Step 2: Conversion to STL:

STL has become a de facto standard as file format used by the AM machines. This file describes the external closed surfaces of the original CAD model and it's used by the software for calculation of the slices.

Step 3: Transfer to AM Machine and STL File Manipulation:

The STL file in which the part is described is transferred to the AM machine. The file is manipulated in order to achieve the appropriate size, position and orientation for the build process.

Step 4: Machine Setup:

The AM machine need a proper set up before the build process. The setup is related to the build and material parameters, such as timings, layer thickness, energy source and material constraints

Step 5: Build:

The actual building process is automated, and carried out by the machine without major supervision. A general monitoring of the machine is needed in order to ensure there were no unexpected errors during the process, such as lack of material, alignment, software or power glitches and others.

Step 6: Removal:

After the build is complete the parts are removed from the machine. In order to interact safely with the machine this has to be equipped with safety interlock, for example to assure no parts of the machine are moving and the temperatures are low enough for a safe manipulation.

Step 7: Post-processing

After the completion the parts may require additional processing, such as cleaning from dust or excessive material and the removing of the supporting features. Parts may be weak, because of the nature of the process or the material, and may need time and careful manipulation in order to be useable.

Step 8: Application

Parts are now are complete, even if they may require some kind of additional treatment (superficial, aesthetic or thermic) before they are ready for use. Sometimes these treatments may be long and labor intensive, if the finishing requirements are very demanding, but this is no usually the case.

Even if they are designed to operate unattended regular checks and scheduled maintenance are needed, the amount of which is related to the technology used. Since the limited availability of standards, both for materials and process, many machine vendors provide or recommend test patterns, useful to periodically check the regular operative parameters of the machine. It must be noted that many AM machines require careful maintenance. Some may use fragile laser or printer technology that must be carefully monitored and that should preferably not be used in a dirty or noisy environment.

Materials for AM may require special attentions, in the production, handling and storing. Some have limited shelf-life, or may undergo unwanted chemical reactions during the storage or the fabrication process. Some of these materials may be used for more than one build, and this reuse could degrade the properties if performed many times over.

Born as a way to obtain real life model of objects in a short time, AM has improved in final product quality, materials and accuracy, and that helped spreading this technology, being of the reasons to obtain a model to supply information about what is known as the "3 Fs": Form, Fit and Function.

At first the models were used to appreciate the shape of a design (Form), then the improved accuracy of the process allowed to build components provided with the tolerances required for assembly purposes (Fit). The parts could be assessed according to how they eventually work (Function), once even the materials properties were improved.

In an integrated process chain AM can be used to shorten not only product development times and cost, but the production itself, since some of these technologies are recently been developed to the extent that the output is suitable for end use. Furthermore, use of high-power laser technology has meant that parts can now also be directly made in a variety of metals, thus extending the application range even further.

Even if the technology we are referring to is primarily the use of additive processes combining materials layer by layer, the term "additive manufacturing" isn't the only one used to name the technology. Other proposed, previously adopted or commercially used identifications are:

Automated Fabrication (Autofab): Proposed in the early 1990s [15], can also be used to describe other forms of computer numerical controlled (CNC) machining centers since there is no direct reference as to how parts are built.

Freeform Fabrication or Solid Freeform Fabrication: The "freeform" term relates to the independence of the forms from the manufacturing process, pointing to the capability of the processes to fabricate complex geometric shapes.

Additive Manufacturing of Layer-Based Manufacturing: This name is related to the way the processes fabricate parts (adding layers of material), in contrast to machining processes, which subtracts from the initial block of raw material. Not every process is purely additive, with some that could use subtractive processing at some stages. Variation of this have been proposed, such as Additive Fabrication [16], but because of the confusion created in some regions of the world by the term fabrication, associated with sheet metal bending, the AF term has been abandoned.

Stereolithography or 3D Printing: These two terms were born to describe specific machines by their developers, that are Stereolithography (SL) by the US company 3D Systems and 3D Printing (3DP) by researchers at MIT, who developed an ink-jet printing-based technology. These terms refer to the extension on the third dimension of 2D processes (lithography and printing).

Rapid Prototyping: This term refers to the process this technology was designed to improve and/or replace. Because of the improvements in accuracy and materials properties this technology is now used for purposes way outside the "prototyping" definition.

It's worth remembering that even if in literature most of the terms introduced above are interchangeable, different terminology may emphasize the approach used in a particular instance.

To complete the overview are here introduced some of the main advantages of AM processes, compared to traditional manufacturing technologies:

- The speed of the process, not only referred to the time it takes to build parts but to the overall speeding up of the whole product development process.
- Reduction in process steps, since even with parts of great complexity building with an AM machine is generally performed in a single step (other separate steps may involve finishing). Traditional manufacturing processes may require multiple steps for just the creation of the tool needed for the building. Furthermore, with AM changes of the design can be applied later in the development of the production.
- Less resources and processes, since AM doesn't need skilled craftsman to build a prototype, it usually only needs the CAD drawings and a trained AM machine operator. The amount of processes is reduced too, since there's no more need for different building technology, such as molding, forming, CNC machining and hand carving. Also, all these technologies are delicate and prone to errors.

2.2 Additive manufacturing process chain

Every product development process involving an additive manufacturing machine requires the designer/operator to follow a set sequence of tasks. Different levels of sophistication, in the machine and the materials, will require different levels of attention to details in the installation, setup and in general in the following of the steps here displayed. Because of the topic of this paper the main focus will be on metals AM processes.

As briefly introduced before, we will refer to eight key steps in the process sequence:

- Conceptualization and CAD;
- Conversion to STL/AMF;
- Transfer and manipulation of STL/AMF file on AM machine;
- Machine setup;
- Build;
- Part removal and cleanup;
- Post-processing of part;
- Application;

Step1: Conceptualization and CAD

Conceptualization of shape and functionality is the natural first step in the development process of any product. If AM is included in the production process a digital description of the product is needed for the physical part to be made, but generally there are many stages in a product development process where digital models are required, making this step common in traditional manufacturing too. AM technology is a direct consequence of the existence of 3D CAD. After the invention of the digital representation of objects the technology to physically reproduce them has been developed, at first with CNC machining, then with AM, but unlike most other CAD/CAM technologies there is little or no intervention between the design and manufacturing stages for AM. The 3D CAD information, essential for the AM process, can be created in a variety of ways, from a design expert human operator via a user-interface, to an automated optimization algorithm or a 3D scan of an existing physical parts. It is even possible a combination of all of the above. Most 3D CAD systems are solid modeling systems with surface modeling components, and solid models are often constructed by combining surfaces together or by adding thickness to a surface. In order to avoid unexpected results from the AM machines output, the input files have to be created without gaps (e.g., “water tight”), a condition which is achieved by most modern solid modeling CAD tools, but may be a problem with old software.

Step 2: Conversion to STL/AMF

STL file format, used by almost every AM technology, is considered a de facto standard. Being introduced by 3D Systems in the 1990s, the term STL was derived from STereoLithography, the first commercial technology introduced by the above-mentioned company. STL is a simple way of describing a CAD model in terms of its geometry alone, it works by removing any non-shape related data and approximating the surfaces of the model with a series of triangular facets. The size of these triangles can be set in the CAD software, in order to ensure no obvious triangles are shown on the surface of the models. A basic rule of thumb to achieve that is to ensure that the minimum triangle offset is smaller than the resolution of the AM machine.

STL files have some limitations. Being just an unordered collection of triangle vertices and surface normal vectors, they have no information on units, color, material or any other feature. To overcome these limitations a new ASTM/ISO international standard has been developed, resulting in the new “AMF” file format. This new standard includes dimensions, color, material and many other features. From now on, for the interest of this paper, the term STL and AMF will therefore be interchangeable.

Even if the conversion of the design to STL is automatic there is always the possibility for errors to occur, so a number of software tools have been developed in order to detect such errors and to automatically rectify them when possible. This software may be applied as a checking stage since, with complex geometries, it may be difficult for a human to detect such problems when manually inspecting the CAD data, resulting in these errors to appear only after the part has been built. Since the variety of complex shape and design made possible by the AM the possibility of error is great, resulting in the difficulty for any software to precisely distinguish between an error and some odd but needed feature shape. Consequently, the software should highlight any problem, making it possible for the human operator to inspect it before the correction.

Step 3: Transfer to AM Machine and STL File Manipulation

The created and corrected STL file can then be sent directly to the AM machine. Even if this technology ideally allows to proceed straight away with the build at this stage, this is not usually the case, since some additional actions could be required before building the part. Not every AM machine will have all of the following functions, but various STL file manipulation software tools able to perform these functions are available for purchase or even free download.

The above-mentioned actions may include:

Verify that the part is correct: The embedded AM machines software usually include a visualization and manipulation tool.

Reposition of the part or changing the orientation: Usually needed to optimize the working space, even in 3 dimensions when made possible by the technology.

Build more than one part: As mentioned above, the optimization of the working space is key, since in some technology (such as Powder Bed Fusion) much of the working time is caused by the deposition of the powder, more than the laser melting process. The parts can be multiple of the same or completely different STL files.

Scaling the part: The parts may require some coating in post processing, or shrinkage may be involved during the process, and all of these variations must be compensated.

Adding identifying features to the part (text or number): Made possible by adding 3D embossed characters to the parts.

Segmentation of the STL (if the part is too large): Required if the parts are too big for the working space.

Merging of multiple STL files: needed for assembly made of multiple STL files.

Step 4: Machine Setup

There is a great number of different machines available on the market. Some of these are very simple, and designed to run a few specific materials and give the user a limited array of options to vary the build parameters, like for instance the layer thickness. Usually this kind of machines doesn't allow too many changes from build to build. On the other hand, there are machines with numerous setup options available, designed to run with different materials, requiring some parameters to be optimized in order to suit the machine to the type of part that is to be built, or permit the part to be built quicker but with poorer resolution when production times have to be cut. Usually is preferred to have some default settings, or save settings files from previously working setups in order to speed up the machine setup process and prevent mistakes from being made. It should be noted that even in presence of setup errors the parts will usually be built, presenting however an unacceptable quality.

In addition to the software parameters there are physical preparations required for the machine to successfully complete the build. For example, the operator must check if sufficient build material is loaded into the machine, if the material has been correctly prepared (sifted, loaded and leveled in the case of powder), if the build plate is inserted and leveled to the machine axes. Some of these operations may be automated or must be performed by a trained operator, depending on the machine.

Step 5: Build

Despite the high level of automation involved in any AM process the first stages require considerable human interaction and decision making, united with manual control. Once these steps are completed the process switch to the computer-controlled building phase, in which the layer-based manufacturing take place. All AM machines will have a similar sequence of layering and similar mechanisms, which include a height adjustable component, in the form of platform or deposition head, a material deposition/spreading mechanism, and layer cross-section formation. Some machines will separate the material deposition and layer formation and some will combine them simultaneously. As long as no errors are detected during the build, AM machines will then repeat the layering process until the build is complete.

Step 6: Removal and Cleanup

After the parts have been built, they have to be separated from the build platform and extracted from the working space. This stage involves the removing of excess build material which may surround the part. This material can be the same of the parts or a different one (secondary support materials, typical with polymeric AM). These supports are needed for various reasons in several AM processes in order to avoid collapsing or warping of the part during the build process. While the process is constantly evolving and some have been developed to simplify the removing of the support material, a considerable amount of manual work may be required at this stage, united with some technical equipment (EDM machine, bandsaw, milling). The operator must be skilled enough to handle the parts without damaging it. So even if different AM parts may require different level of cleanup, all processes require some.

Step 7: Post-Processing

The above-mentioned cleanup stage may be considered the first of the post processing stage.

Post-processing refers to all the preparation applied to the parts in order to make it usable and fitted for the final application. This stage may involve mechanical (abrasive finishing, application of coatings), chemical or thermal treatments, and the choice between these is related to the application to which the part is destined. Thermal treatments are necessary for metallic AM, to be performed before removing the supports. Some parts may require some machining to final dimensions, if the AM process used couldn't require enough accuracy. Some process needs infiltration or surface coating, due to the fragility of the parts produced. Most of the post-processing stage is labor intensive, but can benefit from the use of power tools and additional equipment (polishing tubs or drying and baking oven).

Step 8: Application

After post-processing the parts are ready to use. It's worth mentioning that even if the parts are made from similar materials to those available from other manufacturing processes, the materials and consequently the parts may not behave accordingly to standard material specifications.

This may be caused by some small voids trapped inside the parts, inherently created by the AM processes, which could be the source for part failure under mechanical stress. Furthermore, some processes may cause for the materials not to bond, link or crystallize in an optimum way, or to degrade during building, and because of the layer-by-layer process in almost every case the part properties are anisotropic. Rapid cooling in metal AM processes results in different microstructures compared to conventional manufacturing. These changing in behavior may be better or worse for a particular application, thus the designer must develop the part accordingly. Furthermore, the technology of AM materials is advancing at an increasing pace, and designer must be aware of the recent advancement in material and processes in order to choose the must suited for their needs.

2.3 Metal systems

Giving the topic of this paper only the powder forming metal systems will be described, along with their specificity.

A characteristic shared between polymeric and metal AM processes is the need for the part to be attached to the base platform during the build, because of the residual stress induced by the high-temperature gradients between the temporarily molten material and its surroundings. A part not rigidly attached to a solid platform may warp as it cools, resulting in a non-even spreading of the powder on the further layers. This leads to the need of substrates to lock the parts in place, and it is also a reason to use supports in the design, which increase the rigidity of the entire part. Because of these residual stresses a thermal treatment is needed after the build, before removing the supports.

Due to the higher energy density required to melt metal high temperature are reached. This involve a tight control on the thermal components of the machine, such as heat shielding, insulation, temperature and atmospheric chamber control.

Metal powder system process different material with various density, heavier ones may include high-density tool steels. This involve a considerable mass to be moved, so the powder handling technology must be designed accordingly. The power requirements for positioning and handling equipment must be quite substantial or gear ratios must be high to deal with this mass. Also, the powder inside the feed chambers could be more or less dense, depending on the position on the vertical axes, due to the compression induced by its own weight, affecting the amount of material deposited at each layer and the density of the completed part. This is why usually the powder is compacted in the feed chamber before starting the machine, and the temperature and powder feed settings are adjusted during the build.

Accuracy of metal and polymer powder systems are comparable. Surface roughness can be likened to precision casting technology, being in the order of a few to a few hundreds of microns. Depending on the requirements the maximum peaks can be smoothened using shot-peening (the average peaks are untouched by this process), while key mating features often require surface machining or grinding. Even if the part density will be high, almost fully dense, some voids may still be present, which may lead to the formation of cracks.

The build speed is generally slower compared to a polymer system, because of the bigger requirements of energy to melt metal powder particles. Since laser powers are in the order of the hundreds of Watts the laser scanning has to be slow enough to ensure enough energy is delivered to the powder bed.

Due to the amount of precision needed to obtain a good quality component AM machines require careful maintenance and positioning. Dirty and noisy (both electrical and mechanical) environment should be avoided. The same attentions must be put in the feed materials handling, as will be explained later in this chapter. Since most of the machines are designed to operate unattended it’s important to perform regular checks and the scheduled maintenance, following the vendors instructions and the test patterns which may be provided in order to periodically confirm the regular operations of the machines. Also, laser-based systems are generally expensive because of the cost of the laser and scanning system, and so is the laser maintenance.

Other components of the AM systems which require careful handling are raw materials. Some materials may be sensitive to moisture and light, resulting in a limited shelf life, due to chemical reaction or degradation. It’s possible to use the spare material from previous build into another one, but a degradation in the quality may occur, making it necessary to observe a procedure for maintaining consistent material quality through recycling.

Materials in powder form must be contained into the machine workspace chamber. This kind of materials could create a breathing hazard, contaminate mechanisms or make the workplace slippery. With metal there is also the possibility for the material to be reactive in powder forms, inducing a fire or explosions hazard. AM systems vendors are increasingly designing easier and quicker material handling, allowing to load the new material into the machine offline or with limited changeover, resulting in less off-service and a more continuous production.

Build parameters are strictly related to the material being processed, so every change must involve a careful build setup and process parameter optimization.

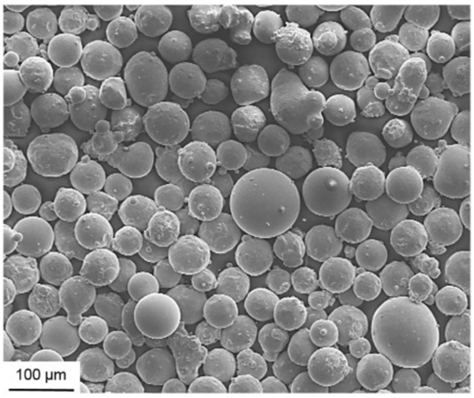

Figure 2.2 SEM image of the 1.4404 metal powder [17].

Due to the peculiarity of the powder AM process a great amount of material used in previous build is available for the following ones, since the powder bed inside the chamber is usually bigger than the parts being built, so a recycling of the material is not only possible but necessary in order to reduce the production costs. It is important to carefully inspect, sift and sieve the material before returning it to the machine, in order to avoid artifacts and other contaminants in the recycled materials. In addition, the thermal history of the unused powder must be considered, since it may cause changes in the powder. Thus, a well-designed recycling strategy based upon one of several proven methods can help ensure that the material being used is within appropriate limits to guarantee good builds [15].

2.4 Design for AM

Additive manufacturing allows a revolutionary freedom in parts creation, leading to a complete rewriting of the designing rules proper of traditional machining processes. The following are some of the changes introduced in the design process by AM processes.

Part orientation

Due to being a layer-based process the same part built in different orientation will result in having different characteristic. Even a simple feature like a cylinder will be profoundly affected by its own orientation in the workspace, leading for example to a well-defined cylinder with a relatively smooth edge if built on its end versus a cylinder with distinct layer stair-step patterning if built on the sides. The part orientation could affect other build characteristics, like the total build time, being in the powder AM systems greatly affected, more than the total build volume, by the total number of layers processed. Since the orientation of the part within the machine can affect part accuracy, it is important to consider which features are critical for the part and in which ones a looser finish could be allowed. Other factors to be considered are: relative precision within different features on the same part, the time it takes to build a part, the amount of supports generated in the selected orientation, or whether certain surfaces should be built face-up. This to ensure good surface finish in areas that are not in contact with support structures, since in general upward-facing features in AM have the best quality, which is one of the few rules-of-thumb that are generically applicable to every AM process.

Removal of supports

Whenever the selected AM technology require supports it is always a good idea to minimize the amount used, in order to reduce the cleanup and postprocess finish, along with the small marks left on the part by the supports. When the supports are necessary, they should be positioned on non-important surfaces. On the other hand, a small amount of supports is needed in order to attach the part in the baseplate, and in doing so avoiding distortions which could result in the failing of the build. Sometimes supports could be located in difficult-to-reach regions within the part, such as hollow cavity inside the geometry, so a planning for their removal could be needed, and the part should be designed accordingly, including access holes (which could be plugged later) or the breaking up of the part, so the supports can be removed before reassembly.

Hollowing out parts

Parts with thick walls may benefit from the use of the AM technology. There are software systems that allow to automatically design these features to include hollow area and cavity, without compromising the part functionality. It can be obtained with the use of honeycomb or truss-like internal structure. This will reduce the build time, the cost from the use of less material, and the mass in the final component. In powder AM systems holes are required to remove excess powder from inside the part.

Inclusion of undercuts and other manufacturing constraining features

This is especially an area in which designing for AM require a different approach compared to traditional manufacturing. While conventional manufacturing would require considerable planning to ensure that a part is fabricated correctly, since undercuts, draft angles, holes, pockets, etc. must be created in a specific order when using multiple-stage conventional processes, if the part is designed for AM this can be ignored. It is otherwise important to remember that this is valid only for parts specifically designed for full AM production, since AM could be used at various stages of the product development process, and AM parts used only for prototyping or aesthetics evaluations must consider all the constraints of the traditional manufacturing.

Interlocking features

Currently one of the biggest limitations for AM processes is the finite dimensions of the build volume, which make it impossible for large parts to be build inside these machines. One solution is to break the design up into segments that can fit into the machine and manually assemble them together later. The focus of the designer will then be on the best way to break up the parts. Parts to be built as separated pieces should be designed with the purpose of facilitate reassembly. This goal can be achieved by incorporating interlocking features and/or maximizing the surface area on which the adhesives will be applied. These areas should preferably be in easy to reach but difficult to observe locations. This break up approach is a viable way to improve the quality of parts which can still fit inside the machine too. Breaking up the part can reduce the amount of supports needed for a build, and the total amount of time too. This is especially true with thin parts expanding in different directions, since thin walls with the wrong orientation may present more significant stair-stepping marks, making it weaker.

Reduction of part count in an assembly

When used for direct manufacturing, AM allow reduction and simplification of part assembly. This involve for instance building the components forming the final assembly in the same build, providing clearance around the moving features. The same apply to complicate parts which would usually need multiple injection if molded.

Identification marking/numbers

When multiple identical parts are made in the same build it is possible to identify them by including identification markers during the design or, with models provided by a third party, by the use of software systems that provides tools for labeling parts by embossing alphanumeric characters onto them as a 3D model. In order to avoid the loss of small parts or to identify parts from the same customer some service providers also usually build all the parts within a mesh box, so they are easy to find and identify during part cleanup

2.5 Powder bed fusion process

After a quick overview of the main characteristics of AM processes, the focus will now be shifted on the metal powder bed fusion processes, being this the main family process used to build the samples studied in this paper. Selective laser sintering (SLS), the first PBF process, was developed at the University of Texas in Austin, USA, and was among the first commercialized AM processes. It has a basic method of operation, which is extended integrating one or more modification of this basic approach in all the other PBF processes in order to avoid specific patented features, enhance machine productivity or enable different materials to be processed.

There are some characteristics shared by all PBF processes, which are the presence of: at least one thermal source for inducing fusion between powder particles, a method for controlling powder fusion to a prescribed region of each layer and mechanisms for adding and smoothing powder layers. Lasers are the most common thermal sources for PBF, and are the one interesting for the purposes of this paper.

This kind of PBF processes are called laser sintering (LS), machines and, even if in this paper only the metal laser process will be addressed, it is worth noting that polymer and metal laser sintering machines are significantly different from each other.

Laser sintering do not provide a full melt of the final part, which requires a secondary thermal treatment. Selective laser melting is an evolution of laser sintering that provide components fully formed after the AM process. Sometimes SLS (Selective Laser Sintering) and SLM (Selective Laser Melting) are confused, using the first to refer to the second.

Initially developed to produce plastic prototypes using a point-wise laser scanning technique, this family of PBF processes were subsequently extended to metal and ceramic powders and other thermal sources have been utilized. As a result, PBF processes are widely used worldwide, have a broad range of materials which can be utilized (including polymers, metals, ceramics, and composites), and are increasingly being used for direct manufacturing of end-use products, as the material properties are comparable to many engineering-grade polymers, metals, and ceramics.

Here follows a brief description of the laser powder bed fusion process, with described the characteristics of a metal laser process.

SLM fuses thin layers of powder, spreaded on the build area using a counter-rotating powder leveling roller. The build area is located inside an enclosed chamber. During the build the chamber is emptied of air and filled with nitrogen, argon or other inert gases, in order to minimize oxidation and degradation of the powdered material, and to avoid combustion of reactive metallic materials. At the build plate level is maintained a liminar flow of gas moving from one side to the other of the chamber. This flow removes combust gases generated from the melting powder, and any loose powder eventually moved from the combustion. Metallic laser processes, unlike polymeric, don’t need for the chamber and the powder to be maintained at an elevated temperature (usually near the melting point for polymers), since these temperatures would be too high for the chamber to sustain it. All the heating power is provided by the laser, and the warping of the parts are avoided using appropriate supports. Once the powder layer has been formed by the roller a focused laser beam is directed, using mirrors, onto the powder bed and the mirrors are moved using galvanometers. The laser source is locked in place, only the laser beam is moved, due to the reflections of the mirrors. The moving laser thermally fuses the material to form the slice cross section. Only the material touched by the laser is melted. After the current layer is completed the build platform is lowered of one-layer thickness, a new layer of powder is laid and leveled using the counter-rotating roller, and the laser beam can proceed to scan the subsequent slice cross section. This process is repeated until the parts are completely built. After the completion of a build a cool down period is typically required, to allow the parts to reach, in the less stressful way possible, a low enough temperature that they can be handled. Handling of metallic powder need special attentions, which will be explained later in this paper. After all the previous stages are done the parts are removed and cleaned of loose powders, and further finishing operations, if needed, are performed.

Metallic materials for PBF

Theoretically all materials that can be melted and resolidified can be used in PBF processes. A brief survey of modern metallic materials alloys workable using PBF processes will be given here, being these interesting for the purposes of this paper. Several types of steels, typically stainless and tool steels (Inox steels, Maraging steels), titanium and its alloys, nickel-base alloys (Inconel 625 and 618), some aluminum alloys (6000 series), and cobalt-chrome (for aerospace and biomedical, or SP2 for dental applications) have been processed and are commercially available in some form. Additionally, some companies now offer PBF of precious metals, such as silver and gold.

Before the invention of metal laser sintering (mLS) a number of proprietary metal powders have been developed. Worth mentioning are: RapidSteel, one of the first metal/binder systems, developed by DTM Corp. in 1996 and consisted of a thermoplastic binder coated 1080 carbon steel powder with copper as the infiltrant. RapidSteel 2.0, introduced in 1998 for the production of functional tooling, parts and mold inserts for injection molding. LaserForm ST-100, characterized by a broader particle size range, with fine particles not being screened out. H13 and A6 tool steel powders with a polymer binder have also been used for tooling applications. Prior to the introduction of modern mLS machines EOS marketed several proprietary materials for their M250 Xtended metal platforms. These included liquid-phase sintered bronze-based powders, steel-based powders and other proprietary alloys (all without polymer binders). On the market were also available proprietary nickel-based powders for direct tooling applications and Cu-based powders for parts requiring high thermal and electrical conductivities.

Even if successfully used in the past, the introduction of mLS and other technology like electron beam melting (EBM) has made these alloys obsolete. Right now, engineering-grade alloys like titanium or steel alloys, nickel based super alloys and CoCrMo alloys can be processed in a number of different manufacturers' machines, making it widely available. Alloys not entirely suitable for mLS are ones that crack under high solidification rates. Also related to the high solidification rates, in some materials the crystal structures produced and mechanical properties are different than those for other manufacturing processes, so these structures may be metastable or too fragile, so heat treatment processes may be needed.

Powder Fusion Mechanisms

Being a technology adopted by different manufacturer, each one has developed his own terminology to describe the mechanism by which fusion occurs, with variants of "sintering" and "melting" being the most popular. However it is impossible to fully describe the powder fusion mechanism with the use of a single word, since there are four different fusion mechanism which are present in PBF processes [18],which include: solid-state sintering, chemically induced binding, liquid-phase sintering (LPS), and full melting, with the most commercial processes utilizing primarily LPS and melting. Giving the topic of this paper a brief description of the full melting mechanism will follow.

Engineering metal alloys (and semi crystalline polymers) are most commonly associated with full melting PBF processing mechanism. As previously anticipated in these materials the entire region subjected to impinging heat energy is melted, to a depth exceeding the layer thickness. Usually the thermal energy of subsequent scans of a laser (next to or above the just-scanned area) is sufficient to re-melt a portion of the previously solidified solid structure. As a result, this type of full melting is very effective at creating well-bonded, high-density structures from engineering metals and polymers. The engineering alloys utilized in metal PBF machines (such as Ti, Stainless steel, CoCr and others) are usually fully melted. Being the whole melting and solidification process extremely rapid the resulting material properties are unique and different from, and sometimes more desirable than, parts made from the identical alloys but with different processes (like cast or wrought). Anyway it should be noted that regardless of whether a technology is known as "Selective Laser Sintering," "Selective Laser Melting," "Direct Metal Laser Sintering," "Laser Cusing," "Electron Beam Melting," or some other name, it is possible for any of these mechanisms to be utilized (and, in fact, often more than one is present) depending upon the powder particle combinations, and energy input utilized to form a part.

Part Fabrication

Four are the most common approaches for using PBF processes in the creation of complex metal components: full melting, LPS, indirect processing, and pattern methods. In the full melting and LPS (with metal powders) approaches, a metal part is typically usable in the state in which it comes out of the machine, after separation from a build plate, which make this mechanism the most interesting for production purposes.

Indirect processing involves the use of a metallic and polymeric powder together, in the form of a mixture or a coating. The polymer is used as a binder for the metal, which will need a furnace processing. Another approach is called pattern approach. The two most common are investment casting patterns or sand-casting molds. These indirect processes won't be described in this paper.

Process Parameters and Modeling

Much of the final quality of the build is related to the process parameters, which has to be optimized. The experience of the operator with the machine and its parameters is critical to the quality of the final component. Being lasers the thermal source interesting for the purposes of this paper we will discuss here parameters and models related to that technology. Anyhow by analogy the same reasoning could be applied to other thermal energy sources, such as electron beams.

Process Parameters

In PBF, process parameters can be lumped into four categories:

1) Laser-related parameters (laser power, spot size, pulse duration, pulse frequency, etc.),

2) Scan related parameters (scan speed, scan spacing, and scan pattern),

3) Powder-related parameters (particle shape, size and distribution, powder bed density, layer thickness, material properties, etc.), and

4) Temperature-related parameters (powder bed temperature, powder feeder temperature, temperature uniformity, etc.).

Even if described separately most of these parameters are interdependent and mutually interacting. A typical PBF machine includes two galvanometers (one for the x-axis and one for the y-axis motion). These galvanometers, as mentioned before, activate one or more mirror, which reflect the laser beam, moving it where needed onto the powder bed. The laser source doesn't move.

The two main scanning modes are contour and fill mode, as showed in Figure 2.3. Contour mode scans the outline of the part cross section for a particular layer, and it is typically done for accuracy and surface finish reasons around the perimeter. The inside of the layer cross section is then scanned using a fill pattern. A common fill pattern is a rastering technique whereby one axis is incrementally moved a laser scan width, and the other axis is continuously swept back and forth across the part being formed. The fill section could be subdivided into squares or strips, or the scans could be randomized. In the squares division each square is processed separately and randomly, in the strips division each strip is scanned sequentially and the strip angle is rotated every layer, while the randomized scans is utilized so that there is no preferential direction for residual stresses induced by the scanning. These strategies are used primarily for metal parts, which giving the high solidification speed are more subordinate to deformations.

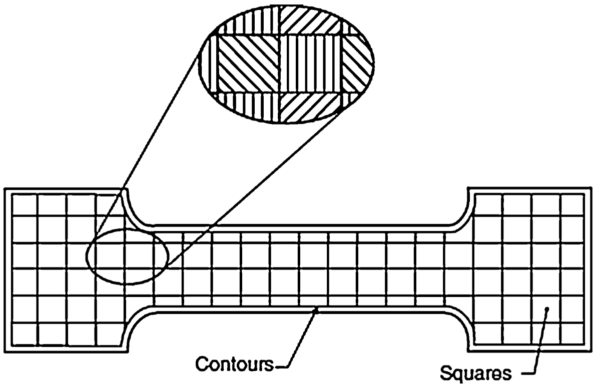

Figure 2.3: Scan strategies employed in PBF techniques

Scan strategy and patterns have a deep impact on residual stress accumulation within the part and not only on the melt pool characteristics.

The position of the part on the build plate may influence the laser path and consequently the distortion in different zones of the part. This effect could be so significant to determine the success of a build, making it failing in some areas of the build plate and successful in other of the same machine.

Characteristics of powder bed (like density and thermal conductivity), laser absorption and powder spreading are heavily influenced by powder distribution, size and shape. For instance, finer particles provide greater surface area and absorb laser energy more efficiently than coarser particles. Due to the number of factors influencing the build (like powder bed temperature, scan spacing, scan speed and laser power) these must be balanced in order to provide the best tradeoff between all the resulting build characteristics, such as the mechanical properties of the parts, the surface finish, the dimensional accuracy, the build rate and the melt pool size. In order to achieve repeatable results, the powder bed should be kept uniform and constant, and in the right combination with the laser characteristics. The usual combination for metal powder is high laser power and low part bed temperatures, which could lead to curling of parts, due to an increased tendency for nonuniform shrinkage and the build-up of residual stresses.

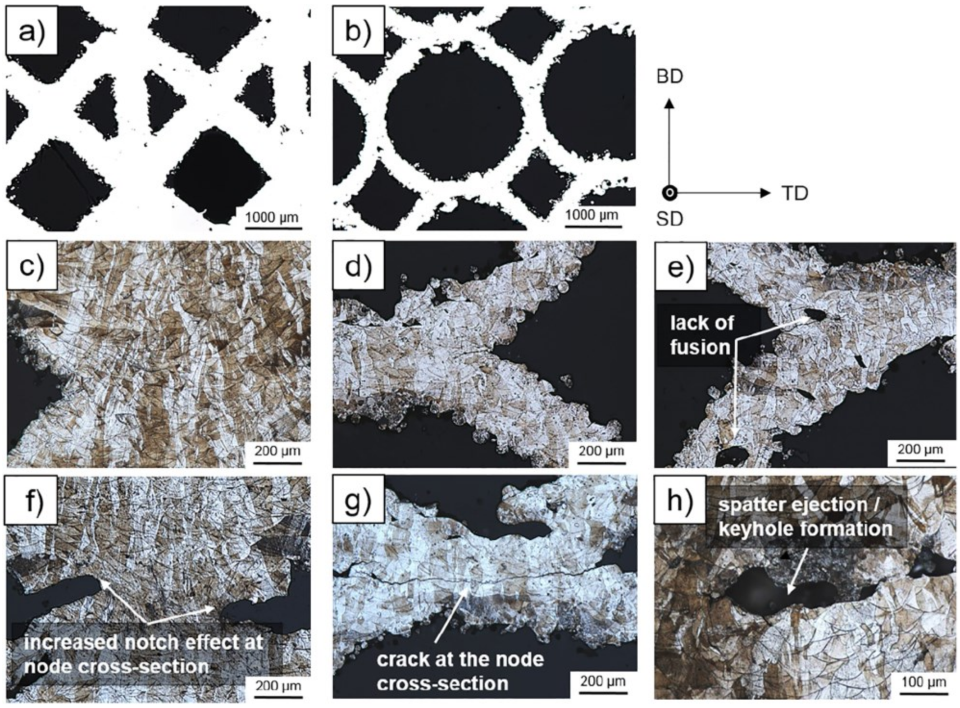

Figure 2.4 Optical micrographs of a), c), f) a f2cc,z lattice structure and b), d), g), e), h) a hollow spherical lattice structure. a) and b) are in polished condition for density analysis, while samples shown in c) to h) are in etched condition [17].

The factors determining the energy input needed to fuse the powder into a useable part are the bed temperature, spot size, scan speed and laser power. The fusion depth and the melt pool diameter are related to the amount of time the laser beam remain in a particular location, and to the laser power and spot size. Lower lasers powers require lower scan speed in order to ensure proper particle fusion. To obtain the desired mechanical properties a sufficient degree of melt pool overlap between adjacent lines of fused material is needed, thus scan spacing should be selected accordingly. Another factor influencing the part quality is the powder bed density, which is related to powder distribution, shape, size and spreading mechanism. Powder bed density may vary between 50% and 60% for most commercial powder. To this factor is also related the bed thermal conductivity, with higher density resulting in higher thermal conductivity and better part mechanical properties. At last it is worth noting the tendency for the market to move towards machine with both continuous-wave and pulsed lasers, in order to benefit from the characteristics of both. For instance, pulsed lasers can partially overcome the tendency of molten metal to form disconnected balls of liquid metal, rather than a flat molten region on a powder bed surface.

Applied Energy Correlations and Scan Patterns

Many are the common physics, thermodynamics, and heat transfer models relevant to describe the PBF techniques. The amount of applied energy which is absorbed by the powder bed, as the laser beam passes, is the main features which determine the melt pool formation and characteristics, and both the melt pool depth and size are a function of absorbed energy density.

Every material needs a series of experiment to optimize the machine performances. It should be noted that when a molten pool of metal is present on a powder bed, a phenomenon called balling often occurs. This is due to the surface tension forces, which will form the molten metal into a ball. This phenomenon is critically important for metal and unimportant for polymer.

Giving the relevance of residual stresses and distortion in laser PBF processes numerous researchers have investigated them, using analytical and finite element methods. These studies correlated the increase of residual stresses and subsequent part deflection with increase in track length, suggesting an high benefic effects from the division of the scan area into small squares or strips (as explained before) and the subsequent scan of each segment with short tracks, adding more reasons for subdividing the layer cross section into small regions for metallic processes. Preferential build-up of residual stresses are partially alleviated by the randomization of square scanning (the choice of which square to scan is random, instead of the scan of contiguous squares one after the other) and changing the primary scan direction between squares. In addition, scanning of strips whereby the angle of the strip changes each layer has a positive effect on the build-up of residual stress. For all the reasons previously mentioned in PBF processes for metals strips and square scan patterns are extensively utilized.

Powder Handling

During the years have been developed multiple different systems for powder delivery in PBF processes, for reasons that goes beyond the need of avoiding the counter rotating roller technology because of the patents connected, resulting in a broader range of powder types and morphologies which can be delivered.

There are four main characteristics any powder delivery system for PBF must possess:

The presence of a powder reservoir big enough to allow to fill the entire build volume, to avoid the necessity of pausing the machine to refill the powder reservoir itself.

The amount of material placed on the build plate by the spreading mechanism must be correct, enough to cover the previous layer but not too much, to avoid waste of excess material.

The layer of powder must be spread so to obtain a smooth, thin and repeatable layer of building material.

The powder spreading must not create excessive shear forces that could disturb the previously processed layers.

Moreover, powder feeding process itself has some typical characteristics, with which the powder delivery system must be able to deal in order to function correctly. These are:

The amount of interparticle friction and electrostatic forces is an inverse function of the particle size, meaning that smaller particles can have less flowability than bigger one. Thus, any effective powder delivery system must keep the powder flowable for effective delivery to occur.

As the surface area to volume ratio of a particle increases, its surface energy increases and the material becomes more reactive. For some metallic materials, such as Ti and Al, this means that the powder will burn if a spark is ignited inside the chamber, or it will become explosive, in the presence of oxygen. For this reason, no sparks should be generated by the powder handling and certain powders must be kept in an inert atmosphere while being processed.

Small particles have a tendency to become airborne when handled, resulting in a cloud of floating particles. These will settle on surrounding surfaces, leading to damage to moving parts, reducing the sensitivity of sensors, clouding of the optics and deflection of laser beams. Airborne particles have also an increased tendency to explode or burn, due to their greater effective surface area compared to packed powers. For these reasons the powder delivery system should be designed in such a way that it minimizes the creation of airborne particles. The size of the particles has to be considered too. Smaller powder particles enable a number of great benefits, like better surface finish, thinner layers and higher accuracy. On the other side smaller powder particles increase all the above-mentioned problems. Thus, every different design for a powder delivery system is a different approach to effectively feed the smallest possible powder particle sizes while minimizing the negative effects of these small powder particles.

Delivery systems

In Figure 2.5 is represented one approach, implemented on the earliest commercialized LM powder delivery system, designed to optimize the solutions to this powder handling and delivery issues.

In the picture are represented the powder reservoir, big as to carry enough material to completely fill the entire build volume. The layer define the amount of powder needed, provided by lowering the platform by the layer thickness and by incrementing the feed cartridge up to a prescribed amount accurately. Now the counter-rotating roller push the raised powder over the build platform, compacting and depositing the powder. If the height of the roller is constant during the build the layer thickness will be determined by the moving of the build platform. The roller, due to its counter-rotating movement, push the powder up, creating a “wave” of powder in front of the cylinder which fluidify the powder, making it more flowable for a particular particle size and shape. The roller transmits small shear forces to the previously processed layers, leaving these relatively undisturbed.

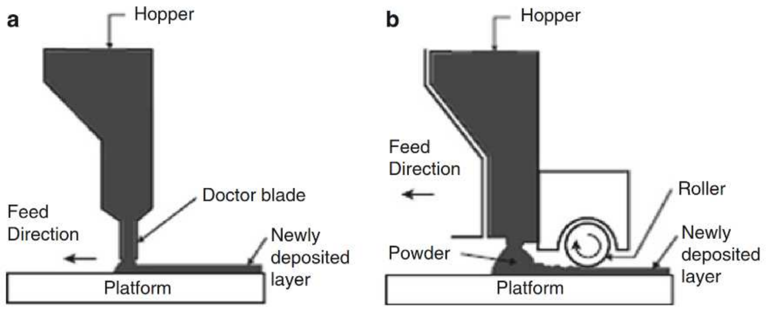

Figure 2.5: Examples of hopper-based powder delivery systems [19].

The doctor blade is another common solution for powder spreading. It consists of a thin piece of metal, used to scrape material across the surface of a powder bed. This solution doesn’t supply powder fluidification, resulting in greater shear forces applied to the previously deposited layer compared to the counter-rotating roller. The powder bed can be fluidized trough an ultrasonic vibration of the blade during the pushing motion. An alternative to the feed cartridge used as a powder reservoir is provided by a hopping feeding system, which delivers powder to the powder bed from above instead of beneath. This system is typically equipped with a powder reservoir separated from the build area, and a feeding system used to fill the hopper. The hopper could either be used to deposit powder in front of a doctor blade or a roller, or those can be integrated with a hopper system, to create an integrated feeding and spreading mechanism. All those systems can be combined with an ultrasonic vibration system to help fluidize the powders. Multimaterial powder bed processing would require multiple hoppers with separate materials, which could change material type layer by layer.

Powder Recycling

Due to the great amount of unprocessed powder left in the build chamber it is important to develop an efficient recycling methodology. The elevated temperature reached in the fused bed of the part being built can cause the surrounding powder bed to fuse. Those elevated temperatures, combined with the presence of reacting atmospheric gases could also change the chemical nature of some types of powder materials. These combined effects cause the change of the properties of many types of powders used in PBF processes when they are recycled and reused. The amount of these changes is various, for some materials are small and thus are considered highly or even infinitely recyclable, in other are huge, therefore the recycling of these material will require a highly controlled methodology, in order to maintain consistent part properties between builds. One of the simplest recycling strategies developed in polymer materials processing involve mixing fresh material, unused material from the build plate and unused material from the powder reservoir in equal third. Unused powder coming from the powder bed could include bigger particles, residue from the fusion of the parts. For these reasons it will typically require a particle sorting method, the most common being a vibratory screen-based sifting device or an air classifier, and after this processing the powder can be mixed with other. Air classifiers are more complex and expensive than sifting systems, on the other hand allow to recycle a larger fraction of material since they mix the powders together more effectively and helps break up agglomerates. Needless to say, the recycled materials must be well mixed together, otherwise parts built from this inconsistent powder will have different properties in different locations. These mixing inconsistencies will be unavoidable with a simple fraction-based recycling approach, due to the different thermal history that powder from different build will have.

PBF Process Variants and Commercial Machines

Giving the large variety of PBF processes developed since its first invention an overview of some commercial or still under development processes will be discussed in the following section. There are parameters and characteristics important to know in order to understand the practical differences between all these processes, such as energy input type, heating process, atmospheric conditions, powder delivery method, optics and other.

Laser-Based Systems for Metals and Ceramics

Commercial laser-based systems for direct melting and sintering of metal powders are provided by many companies, such as 3D Systems (France/USA), Selective Laser Melting (SLM) Solutions (Germany), Realizer (Germany), Renishaw (UK), Concept Laser (Germany), and EOS (Germany).

Being numerous the companies providing these technologies there are numerous competing terminologies to describe them. The most used term is selective laser melting (SLM), with the terms Laser Cusing and DMLS (direct metal laser sintering) used by other manufacturers. In order to simplify the discussion in the rest of the chapter all the technologies mentioned will be referred to as mLS, despite the variant.

First mLS researches, between the late 1980s and early 1990s, were mostly unsuccessful. Processing metal powders is significantly more difficult than polymers, due to the higher laser reflectivity, the propensity to oxidize, the higher surface tension and the higher thermal conductivity. Most commercially available mLS systems are based on the approach developed by the Fraunhofer Institute for Laser Technology (Germany) called selective laser powder re-melting (SLPR), which research developed the basic processing techniques necessary for successful laser-based, point-wise melting of metals. The key for enabling mLS has been the use of lasers with wavelengths better tuned to the absorptivity. In polymer laser sintering CO laser have been used, while Fraunhofer used an Nd-YAG laser instead, resulting in a much better absorptivity for metal powders.

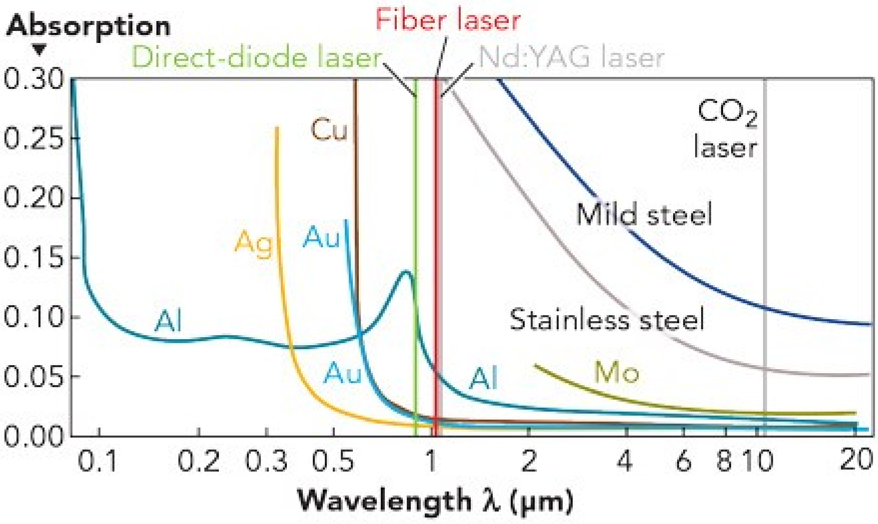

Figure 2.6 Absorption of various metals at relevant wavelengths for industrial lasers [20].

As a result, now all mLS machines use fiber lasers, which have benefits compared to Nd-YAG lasers, being in general cheaper to purchase and maintain, energy efficient, having better beam quality and being more compact. Other introduced factors that enabled the developing of mLS are the different laser scan patterns (compared to pLS), the low oxygen, inert atmosphere control and the use of f-theta lenses to minimize bean distortion during scanning.

As early introduced, one common practice typical of metal LS is the rigid attachment of the parts to a base plate at the bottom of the build platform, to keep the metal part being built from distorting due to residual stress. This reduce the design flexibility for mLS parts compared to polymers, due to the need to remove these rigid supports using a machining of cutting operation in post-process.

Some of the differentiations introduced over the years by the mLS manufacturer to characterize their machines includes maximum build volume, scanning strategies offered, powder handling systems, laser power and number of lasers offered.

Different manufacturers have different approach regarding how much control leave to the users. Some provide only "proven" materials and process parameters, other allow more experimentation by the user. As examples EOS focused on tuning their machine process parameters and scanning strategies for specific materials which they sell to their customers, Renishaw implemented in their machines safety features to help minimize the risk of powder fires, and others like Concept Lasers have focused on the development of specific materials, such as stainless and hot-work steel alloys suitable for injection mold and die cast tooling.

3D Systems has the unique characteristics of being the only manufacturer to allow to directly change the powder bed packing density on the fly, using a roller to spread and then compact powder. Furthermore, has developed machines which can be held at an elevated temperature, thus enabling efficient sintering of ceramic powders, in addition to melting of metal powders. Other like 3D-Micromac (Germany) have focusing their research on multimaterial, small-scale mLS machines.

Process Benefits and Drawbacks

PBF can process a very wide variety of materials, many within the metal family, since, as mentioned, if a metal can be welded is a good candidate for mLS. One of the downsides of PBF metal process is the necessity of supports, needed to keep the part from excessive warping induced from the high residual stresses experienced when processing metals, increasing the costs and time of postprocess. Small internal features (some crucial, like internal cooling channels) can usually be built without supports, which are needed to constrain the part to a substrate at the bottom of the build platform. These needs make the orientation of the part and the location of supports key factors when setting up a build. Because of the residual internal stresses thermal treatments are needed after the build, before removing the supports. This is true with many traditional manufacturing too, so it isn't a real drawback.

Accuracy and surface finish of the parts are strongly influenced by the powder particle size and the operating conditions. Larger particle sizes facilitate powder delivery and processing, with the downside of a worse surface finish and bigger minimum layer thickness and minimum feature size. On the other hand, finer particle sizes will produce smoother and more accurate parts but are difficult to spread and handle. It should be noted that better accuracy will be achieved with low thermal conductivity materials, as melt pool and solidification are more controllable and part growth is minimized when heat conduction is minimized.

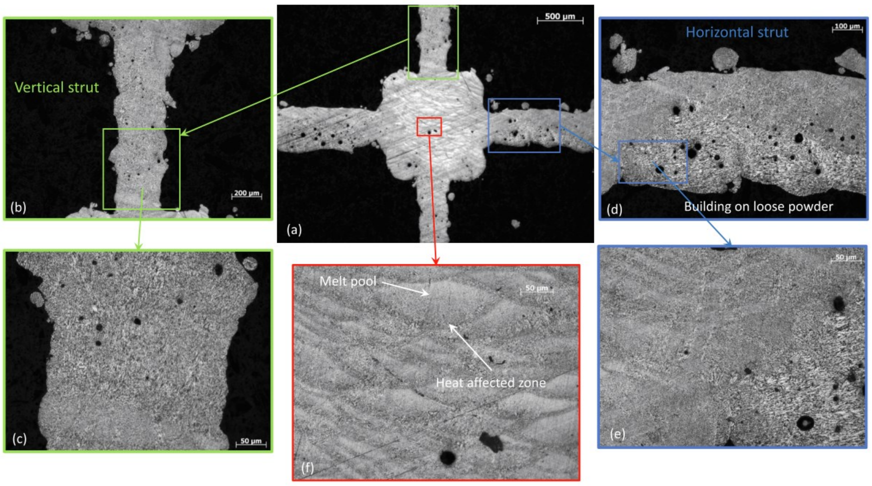

Figure 2.7 Optical micrograph of a SC-BCC sample. Details of microstructure at: (a) strut intersection; (b,c) vertical struts; (d,e) horizontal struts; (f) node.

3 Overview of Nondestructive Testing (NDT) methods

In order to provide the services for which are designed, any mechanical part must offer optimal guarantees of safety and endurance to the conditions of service, either for new or already in-service equipment. A wide variety of NDT techniques are available, and can be implemented, to ensure the quality of a manufacturing process. These techniques allow to ensure the quality of parts or assemblies according to given specifications, allowing not only to detect an indication, but also to classify and locate it.

Most of the NDT techniques provide as an output of the test that is called an "indication". An indication is the result of an interaction between a physical phenomenon and an imperfection. The results of this interaction can be usually observed by means of a signal or an image, which is called "indication", and must not be confused with the imperfection itself. The indication is a representation of the imperfection, and can be very different from the imperfection itself. [21]

3.1 Introduction to Nondestructive Testing

Also commonly referred to as nondestructive examination (NDE), nondestructive inspection (NDI) and nondestructive evaluation (NDE), Nondestructive Testing (NDT) consists of a wide range of non-invasive inspection techniques. It can be used to detect, characterize, or measure the presence of damage mechanisms (e.g. corrosion, discontinuities or cracks), to evaluate material properties or to perform in-line assessments of production's quality.

In the words of the American Society for Nondestructive Testing (ASNT):

> *"Nondestructive testing (NDT) is the process of inspecting, testing, or evaluating materials, components or assemblies for discontinuities, or differences in characteristics without destroying the serviceability of the part or system. In other words, when the inspection or test is completed the part can still be used." [22]*

As introduced, primary characteristic of these testing methods is the ability to leave the sample intact, making possible to apply some of these methods on final products actually being put into service, or during the service itself. It allows the inspection of components in a safe, reliable, and cost-effective manner without causing damage to the equipment or shutting down plant operations (in-line inspection). Characteristics of many NDT techniques is the ability of locating defects and determining their main features, such as size, orientation and shape. Other tests, destructive in nature, are often and traditionally used to determine some of the physical properties of materials, while NDT are more effective in the determination of discontinuities and differences in material characteristics. As the name imply destructive testing involves the damage or the destruction, during the inspection process, of the part or the sample being tested.

As previously mentioned, due to the nature of them, NDT techniques can be performed not only in a dedicated time slot after the production has ended but also during the manufacture, or even on equipment that is in service. While in manufacturing the purpose of NDT is to determine if parts are fit for their future function, during operation it can be used to monitor damage mechanisms, evaluate the current damage state of equipment allowing the engineer to make informed decisions for remaining equipment life evaluations.

It's impossible to briefly mention all the areas in which NDTs are applied. Giving the great amount of different methodology available, nondestructive tests are applicable on a wide range of different components, and every time the parts (or structures) which need inspection can't be sacrificed, for cost, conservation or production reasons. These methodologies allow in-line inspections, to ensure the quality of production processes (such as joining, welding and assembly phases) and the quality of materials, and in-service inspections, used to ensure the necessary integrity of the components during its use.

Even if many processes and technologies are shared with the medical field, the term "nondestructive testing" is not used to describe medical applications (in which, of course, every test is developed to be the least invasive possible).

3.2 Main NDT Test Methods

Because of their specialized nature, test method names often refer to the type of penetrating medium or the equipment used to perform that test.

Some of the current most commonly used NDT methods, as listed by The American Society for Nondestructive Testing, are:

- Acoustic Emission Testing (AE),
- Electromagnetic Testing (ET),
- Guided Wave Testing (GW),
- Ground Penetrating Radar (GPR),
- Laser Testing Methods (LM),
- Leak Testing (LT),
- Magnetic Flux Leakage (MFL),
- Microwave Testing,
- Liquid Penetrant Testing (PT),
- Magnetic Particle Testing (MT),
- Neutron Radiographic Testing (NR),
- Radiographic Testing (RT),
- Thermal/Infrared Testing (IR),
- Ultrasonic Testing (UT),
- Vibration Analysis (VA)
- Visual Testing (VT).

According to the ASNT the six most frequently used test methods are MT (Magnetic Particle Testing), PT (Liquid Penetrant Testing), RT (Radiographic Testing), UT (Ultrasonic Testing), ET (Electromagnetic Testing) and VT (Visual Testing). These test methods will be briefly described in the next pages, followed by a brief introduction of other, less used methods.

Being the main focus of this paper, Direct Image Correlation methods will be illustrated on their own in chapter 4.

Magnetic Particle Testing (MT)

In ferromagnetic materials is possible to use magnetic fields to locate surface and near surface discontinuities, a technique called Magnetic Particle Testing. The magnetic field can be applied with an electromagnet (which create a field only when current is being applied) or a permanent magnet. If there is a discontinuity such as a crack or a flaw on the surface of the part, the magnetic flux will be broken from that place and a new south and north pole will form at each edge of the discontinuity. So, when the magnetic field encounters a discontinuity transverse to the direction of the magnetic field, the flux lines produce a magnetic flux leakage field of their own as shown in Figure 3.1. This variations in the flux lines are made visible thanks to very fine colored ferromagnetic particles. This visible indicator can either be a liquid solution, with the magnetic particles suspended in the solution, or a dry powder. These particles can be colored with a visible dye or a fluorescent dye, requiring this to be put under an ultraviolet light to be visible. Because of the differences in the magnetic behavior of air and ferromagnetic materials, when the magnetic particles are applied to the surface of the part they will be drawn into or onto the discontinuity, producing a visible indication on the surface of the part.

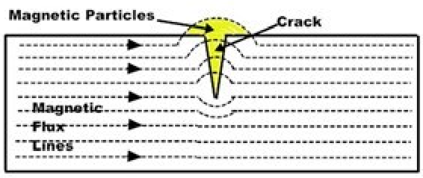

Figure 3.1 Discontinuity in the magnetic flux lines due to crack.

MT Techniques

Yokes

Due to its portability, field inspections are usually performed using a Yoke. A typical use of this technique is the inspections of welding. This device, visible in Figure 3.2 uses an electric coil wrapped around a central core which, when a current is applied, generate a magnetic field extending from the core into the part, down through the articulated legs.

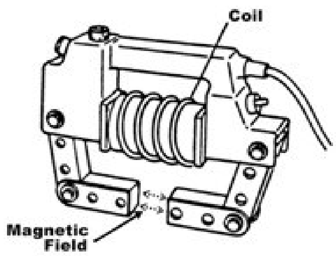

Figure 3.2 Articulated AC/DC Yoke.

The magnetic flux lines run from one leg to the other, making this known as longitudinal magnetization. When the yoke is energized and the legs are placed on a ferromagnetic part a magnetic field is introduced into the part (as shown in Figure 3.3).

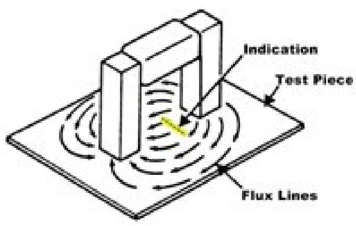

Figure 3.3 Magnetic field introduced by the Yoke.

Discontinuities can be found because of the flux lines, which run from one leg to another. In order to be found these irregularities must be oriented perpendicular to a line drawn between the legs. Because of this characteristic, to ensure no indications are missed the yoke is always used at least twice, with one direction turned 90° in respect to the other. This kind of application if known as “indirect induction”, since only the magnetic field penetrates the part, and all of the electric current is contained in the yoke.

Prods

Prod units utilize the same principles as the yoke in an opposite way. A circular magnetic field is generated around the legs as the current runs through the part. This is known as “direct” induction (Figure 3.4).

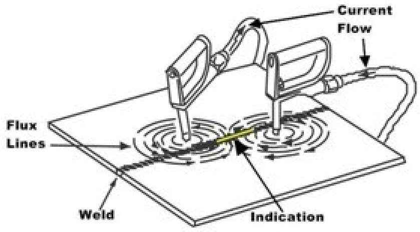

Figure 3.4 Inspection using prod units.

As with the yoke, two inspections are done, the second with the prods oriented 90° to the first application. Unlike the yoke, irregularities oriented parallel to a line drawn between the prods can be found, due to the magnetic field between the prods, which travel perpendicular to a line drawn between the prods.

Coils

Longitudinal magnetic fields are created using electric coils. Due to their shape the resulting flux lines are oriented through the coil. In this configuration, in parts placed in a coil the indications are oriented transverse to the longitudinal field.

Heads

A combination of coils and a set of heads through which electric current can be passed, generating a magnetic field, it’s used in most of the so called “bench units”, also known as horizontal wet bath machines. These are called wet bath machines because of the use of fluorescent magnetic particles in a liquid solution. In order to test a component this is placed between the heads and held in place by the moveable head, moved up to the correct location. The part is then wetted down with a bath solution containing the magnetic particles and while the particles are flowing over the part the current is applied.

Due to the configuration (the current flow is from head to head) the magnetic field is oriented 90° to the current, so indications oriented parallel to a line between the heads will be visible.

Central Conductor

Used in testing hollow parts, such as pipes tubes and fittings. As shown in Figure 3.5 it’s composed by a conductive circular bar, placed between the heads with the part suspended on the bar.

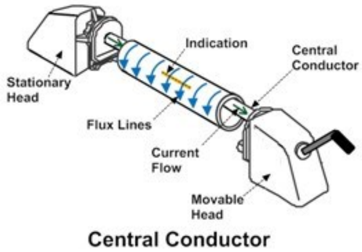

Figure 3.5 Inspection of a pipe using the central conductor method.

The current is then applied, after the part is been wetted in the bath solution, and will travel through the central conductor. This technique allows both the inner and outer diameter of the part to be inspected at once. The magnetic field produced by this configuration is perpendicular to the current flow, making it wrapping around the test piece, so indications running axially down the length of the part can be found.

Liquid Penetrant Testing (PT)

This technique uses the properties of very low viscosity liquid to penetrate into fissures and voids open on the surface of objects on which they are in contact, due to their surface tension. The fluid is subsequently called the penetrant. After the application the penetrant is allowed to sit on the surface for a specified period of time (the "penetrant dwell time") before being cleaned of the excess, making sure not to remove any liquid that has flowed into voids. Any excess is then removed, and an indication is created by the penetrant that will flow back out of the voids after being trapped in it. The part is then lightly coated with a developer, and given time ("developer dwell time") to allow the penetrant from any voids or fissures to seep up into the developer, creating a visible indication. After the developer dwell time the part is visually inspected, with the use of a black light for fluorescent penetrants. Developers provide a color contrast to the penetrant being used, and usually are fine-grained, white talcum-like powders. The visible dye penetrant process is shown in Figure 3.6. When performing a PT inspection, it is imperative that the surface being tested is clean and free of any foreign materials or liquids that might block the penetrant from entering voids or fissures open to the surface of the part. It should be noted that penetrant testing can be performed on both magnetic and non-magnetic materials, with the exception of porous ones, in which does not work well.

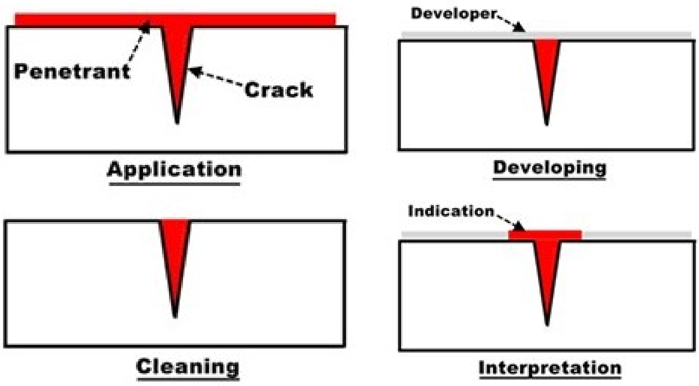

Figure 3.6 Schematics of a liquid penetrant testing analysis.

PT Techniques

Solvent Removable

Solvent Removable penetrants are those penetrants that require a solvent other than water to remove the excess penetrant. After the dwell time the part is cleaned with a cloth dampened with penetrant cleaner, and after the cleaning the developer is applied. These penetrants are usually visible to the naked eye, commonly red colored and used in pair with white developer.

Water-washable

Water-washable penetrants have an emulsifier included in the penetrant that allows the penetrant to be removed using a water spray. They can either be applied by dipping or submerging the part in a penetrant tank (for small parts) or by spraying or brushing for large parts. After the part is covered with the penetrant is placed on a drain board during the penetrant dwell time. The penetrant is washed with a water spray to remove the excess, usually in a dedicated rinse station. The water is then removed with a fan or a warm air dryer. When dry the part is coated in developer and, after the developer dwell time, inspected.

Post-emulsifiable

Post-emulsifiable are penetrants that do not have an emulsifier included in its chemical make-up like water-washable penetrants. In order to remove the excess penetrant from the part's surface an emulsifier is applied to the surface prior to the water-washing step. Emulsifiers can be lipophilic (oil-based) or hydrophilic (water-based). After the emulsifier dwell time the water washing and developing process is the same as for the water washable penetrants.

Radiographic Testing (RT)

Industrial radiography, similarly to medical radiography, use a penetrating radiation to expose a test object, recording on a medium placed against the opposite side of the object the radiation that passes through the object being inspected. Objects composed of materials with different density or having different thickness require different penetrating radiations. For parts made of denser materials or with thicker features will be used gamma radiation, while thinner or less dense material can be inspected using electrically generated x-radiation (X-rays). The sensitivity of x-rays is nominally 2% of the materials thickness. [23]

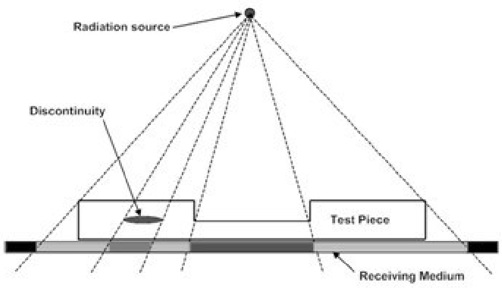

Figure 3.7 Radiation exposing the receiving medium after crossing the test object.

Gamma radiation is given off by decaying radioactive materials, with the two most commonly used sources of gamma radiation being Iridium-192 (Ir-192) and Cobalt-60 (Co-60).

Traditionally the recording media used to be (and in many cases it still is) industrial x-ray film, while now digital radiation detectors are common. Whatever the recording media being, the radiation passing through the test object exposes the media. The resulting effect will be lighter areas where less radiation has penetrated the part and darker areas where more radiation has passed through. This will result in having darker spots in the image where defects or voids are in the part.

RT Techniques

Film Radiography

Like film photography, film radiography uses a physical support to obtain an image of the part being tested. This film is composed of a thin transparent plastic coated with a fine layer of a reactive material, usually silver bromide, on one or both side of the film. The reactive material undergoes a reaction when exposed to radiation, that, after the developing process, allows it to convert to black metallic silver. During the developing process the silver in fixed to the plastic that after drying becomes a finished radiographic film. Different components will require different methodology in order to be tested, and therefore different specifications will apply. For instance, ISO 17636-1 specifies fundamental techniques for examination of fusion welded joints in metallic materials by conventional X and gamma-ray techniques with a film. [21]

In order to obtain good quality images, the respect of some requirements is necessary. The area of interest in the part must be within a certain density range, to obtain enough contrast so that the image could be “read”. Other parameters to be considered are the thickness of the part being inspected, the strength of the radiation and the distance of the source from the film. If not managed correctly these parameters can lead to the necessity of repeating the exposure of the part.

Computed Radiography

In Computed Radiography technique (CR) the film is replaced by an imaging plate, which makes it a mixed technique, using both physical and digital technologies. X or gamma photon flux create a latent image which is captured by some phosphorus crystals (phosphor layer consist in a mix of bonded fine grains of fluor, barium and bromium doped with europium). When phosphorus crystals interact with photons incident on the plate the trapped electrons at a higher energy level form the latent image. Then a high-resolution laser beam, which stimulates the trapped electrons, scan the plate. That is photo stimulated luminescence, which entails a brightness located in the visible spectrum. A photomultiplier then measures the light, digitize and store it in a computer's memory as a function of the laser beam position on the plate. This technology allows to reuse the plate, after being erased by an internal white light source, which induce a return of the trapped electrons to their original energy level. The number of measured light photons is proportional to the number of trapped electrons being proportional to the number of X or gamma photons which interacted with the plate [21].

Computed Tomography

While conventional radiography takes a planar image of a three-dimensional object, computed tomography reconstructs an image from a cross sectional plane of an object. In Figure 3.8 is briefly illustrated the difference between radiography and tomography. After digital reconstruction of multiple views taken at different viewing angles, these are used to develop the CT image. This technology allows the position of internal discontinuities to be determined without the need of multiple expositions from different angles. The triangulations are performed by the computer, using every point in the plane as viewed from many different directions. Full 3D reconstruction of the object and of its content is then now possible. This allows not only to perform NDT but also advanced metrological analyses of the parts and its internal items and then comparison with CAD design. [21]

Some of the main advantages of the use of CT for Ti6Al-4V specimens manufactured by AM are summarized by J. Waller [24] as follows:

- Detection of deep or embedded defects;
- Interrogation of inaccessible features;
- Confirmation effectiveness of post-process, treatments often required to make usable parts;
- Characterization and qualification as manufactured parts;

On the other side, CT can't reliably detect cracks, since cracks oriented perpendicular to the X-ray beam may not be detected. Also being based on the differential attenuation, CT is not able to detect an imperfection providing a too weak attenuation. This may happen for example in presence of close atomic number between imperfection and parent metal and different metallurgical phases in the same component. [21]

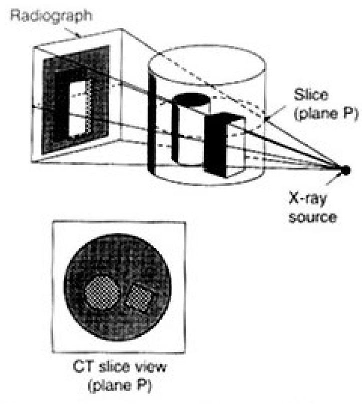

Figure 3.8 Differences between computed tomography and traditional radiographic imaging.

Digital Radiography

Digital radiography (DR) avoid the use of physical supports for the creation of the image. It directly digitizes the radiation that passes through an object into a digital image. Direct digital imaging uses a various array of different technologies, such as amorphous silicon, charge coupled devices (CCDs), and complementary metal oxide semiconductor (CMOSs). This technology allows for the image to be available for viewing and analysis in seconds, since there is no time needed for scan of physical supports. It also allows for a superior resolution than the other techniques.

Ultrasonic Testing (UT)

Ultrasonic testing uses technologies well-established in other fields, such as fish finders and naval SONAR. The part being inspected is hit with ultra-high frequency sounds, which will reflect back to the sending unit when it hits a material with a different acoustic impedance. The reflected sound can be presented on a visual display for analysis. In order to locate the reflector (the indication with the different acoustic impedance) the speed of sound through the part and the time required for the sound to return to the sending unit are required.

Different frequencies lead to different observations. While high frequencies have low penetrating power, they have high sensitivity (the ability to "see" small indications), at the same time lower frequencies penetrate more deeply but have less sensitivity. The frequencies used are too high to be heard, and are commonly between 1.0 to 6.0 MHz [23].

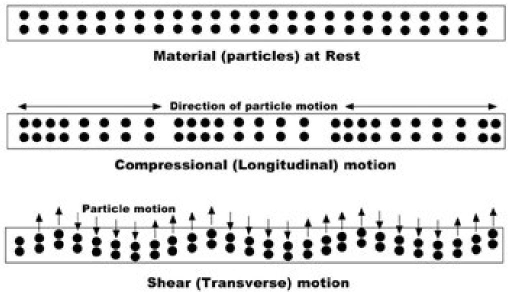

Figure 3.9 Schematic view of sound waves moving the body's particle.

Different types of sound waves are used to detect different indications. The two most commonly used are shear and compression wave (Figure 3.9). Shear (transverse) waves, which travel at approximately half the speed of longitudinal waves, cause the atoms to vibrate perpendicularly to the direction of the sound, while compression waves cause the atoms in a part to vibrate back and forth, parallel to the sound direction.

A transducer is used to introduce the sound into the part, converting electrical impulses from the UT machine into sound waves. The returning sound is converted into electrical impulses fit to be represented on screen. With the proper calibration of the machine this technique allows an experienced operator to determine the type of discontinuity that caused the reflection, and to determine the distance from the transducer to the reflector. Due to the properties of air a gel is needed between the face of the transducer and the surface of the part to allow the sound to be transmitted into the part. Application on AM processes have been studied, for example by H. Rieder et al. [25] whom used ultrasound with sensors set underneath the building platform in order to monitor the SLM process.

UT Techniques

Straight Beam

This technique is used to locate discontinuities (reflectors) inside the part and to analyze thickness of objects. The characteristic of this inspection is the use of longitudinal waves to interrogate the test piece. Internal reflector will generate a reflected sound that will travel to the transducer faster than the sound coming back from the wall of the part, and this result in an indication. Since the different purpose, digital thickness tester even if using the same process will give an output as a digital numeric readout.

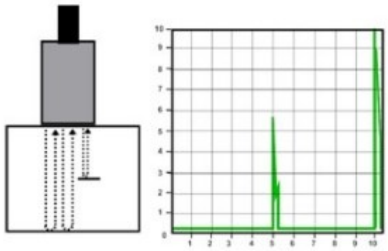

Figure 3.10 Indication on a straight beam ultrasonic technique.

Angle Beam

Angle beam inspection uses the same type of transducer but, due to the way it is mounted, the sound beam is transmitted into the part at a known angle. Different part's shapes, dimensions and features will require different inspection angles, with 45°, 60° and 70° the most commonly used. Frequency and wedge angle are usually specified by the governing code or specification, but if not, the operator will select a combination that will adequately inspect the part being tested.

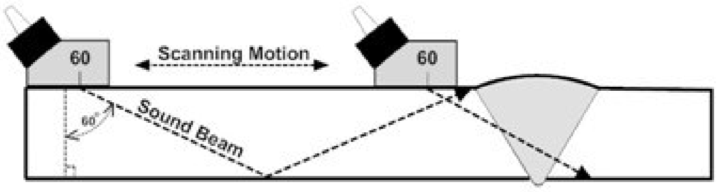

Figure 3.11 Movement of the sound beam inside the test part.

In angle beam inspections the sound beam has to pass through the full volume of the weld, so the assembly formed by the wedge and the transducer is moved back and forth towards the weld. Reflectors more or less perpendicularly aligned to the sound beam will send back different sound to the transducer.

Immersion Testing

Immersion Testing use the water in which the part is being submerged, using a tank, as coupling medium to allow the sound beam to travel from the transducer to the part. The UT machine travel down the length of the tank using a movable platform placed on the side of the tank.

The transducer is mounted on a waterproof tube that can be moved around the tank, and the combination of the movable platform and the tube allow the transducer to be moved on the X, Y and Z-axes. To obtain the necessary accuracy all directions of travel are gear driven. The transducer on the tube is swivel-mounted, which allows it to be oriented so the sound beam enters the part at the required angle. Multiple transducers can be used at the same time. Part with specific geometry can use peculiar mounting mechanism, such as powered rollers for round parts, which allow the full circumference to be tested.

Through Transmission

Through transmission use two transducers placed in front of each other, with the part being inspected in the middle of them, as showed in Figure 3.12. One of the transducers is a transmitter and the other is the receiver. Reflectors inside the part can then be located because they will cause a reduction in the amount of sound reaching the receiver, resulting in a signal with a lower amplitude.

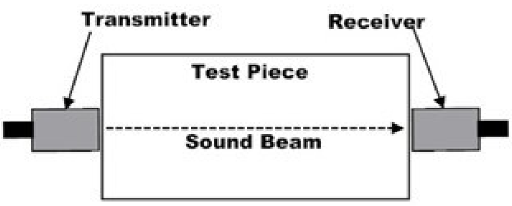

Figure 3.12 Through transmission testing method.

Phased Array

Phase array inspections give a visual representation of a slice of the part being inspected. It uses a probe with multiple elements, each one individually activated. The sound beam can be moved by varying the time when each element is activated, allowing the resulting data to be combined.

Time of Flight Diffraction

Time of Flight Diffraction (TOFD) uses two transducers set at a specified distance from each other. The sensors are placed on opposite sides of the feature to be tested (usually a weld). One is the transmitter while the other is the receiver. The transducers travel along the length of the weld while remaining at the same distance from it. This technique allows a greater accuracy in the determination of defect's size and location compared to conventional UT methods. In order to obtain it two sound waves are generated, one travelling through the weld at an angle then back up to the receiver and the other along the part surface between the transducers. Cracks embedded in the weld cause diffraction in the sound from the tips of the crack, generating low strength sound wave that, after being picked up by the receiving unit and amplified can be run into a computer to be analyzed.

Electromagnetic Testing (ET)

Electromagnetic testing is a general test category that includes Eddy Current testing, Alternating Current Field Measurement (ACFM) and Remote Field testing.

It should be noted that even if being an electromagnetic test, magnetic particle testing is considered a stand-alone method due to its widespread use.

All of these techniques use the induction of an electric current or magnetic field into a conductive part. In order to understand the results, the resulting effects are recorded and evaluated.

ET Techniques

Eddy Current Testing

Eddy current testing uses the small current created around the magnetic flux field inducted into a coil when an alternating current is applied in it. This secondary current, called "eddy" current, have a flow pattern that will be affected by discontinuity encountered in the test piece. The discontinuity can be characterized detecting and using the change in the eddy current density

A simplified schematic of eddy currents generated by an alternating current coil ("probe") is shown in Figure 3.13.

Different shape or features will require different type of coil (encircling coils are used to test tubular and bar-shaped products), and this technique has limited penetration and works best on smooth surfaces.

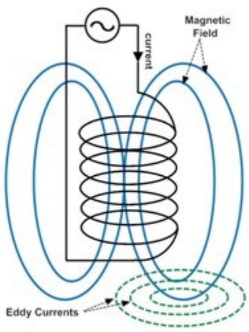

Figure 3.13 Schematic of eddy currents induced in the test piece by the probe

To test tubular objects the part can be fed through the coil, allowing the entire cross-section of the object to be analyzed, but circumferentially oriented discontinuities may not be detected in this configuration, due to the direction of the flux lines.

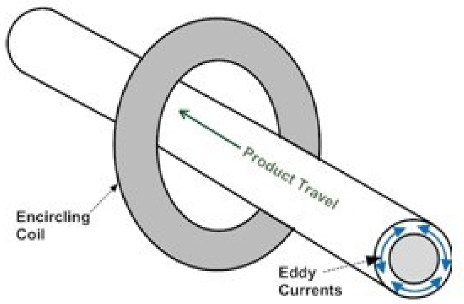

Figure 3.14 Eddy currents induced in a circular test piece

Alternating Current Field Measurement

Alternating Current Field Measurement (ACFM) analyze the magnetic field created by a specialized probe that introduces into the surface of the test piece an alternating current. This field will be uniform in part with no discontinuities, while any discontinuity open to the surface will make the field flow under and around them, causing a disruption of the field that can be detected by sensors embedded in the probe. The data can be analyzed by software that can determine depth and length of the discontinuity. This technique can be used even if many layers of coating are present on the surface and compared to eddy current methods provides better results on rough surfaces.

Remote Field Testing

Remote Field Testing (RFT) use the strong skin effect present in ferromagnetic tubing to inspect them. While for non-ferromagnetic tubes eddy current method tends to provide more sensitivity, RFT provide better results throughout the thickness of the tube, with approximately the same sensitivity at both the internal and external surfaces of the tube.

Visual Testing (VT)

Because of its immediacy is the first and most commonly used test method in industry, and is strictly integrated in most of the other test methods, since most of them require an operator to look at the surface of the part being inspected. It consists in the evaluation of discontinuities by the visual observation of the surface of the object. Since the limitations of direct vision, some aides may be used. These could include various enhancer, like optical instruments such as magnifying glasses, mirrors, vision sensor and computer-assisted viewing systems. This method allows to detect cracks, misalignment of parts or physical damages.

Acoustic Emission Testing (AE)

Acoustic emission (AE) is the sound waves created when a material undergoes stress (internal change), as a result of some external force. The related test uses multiple sensors (piezoelectric ceramic elements) to locate discontinuities in the part analyzing the different ways in which a part vibrates, and therefore emit sound, after an excitation cause is been applied to the part. The excitation cause is an external force, such as a knock with an “hammer” (impulsive load) or a rapid temperature or pressure change. This variable load creates stress waves, which generate elastic waves in the material (small material displacements or plastic deformation). These waves are then detected by an array of sensors attached to the part surface. This method is particularly effective for continuous surveillance of load-bearing structures [23].

Guided Wave Testing (GW)

Guided wave testing on piping uses the reflections of one or more ultrasonic waveforms, inducted into the pipes by a controlled excitation and travelling along the length of the pipe, to detect changes in the pipe stiffness or cross-sectional area. The guided wave is introduced into the pipe using an exciter coil or a transducer ring assembly. This system allows the configuration to be controlled using a computer with installed a proper control and analysis software, to drive the exciter mechanism and to analyze the results. After being designed for the specific diameter of the pipe being tested this system allow the test to be conducted without the need to remove coatings or insulation, and to inspect the pipe wall volume over long distances.

Laser Testing Methods (LM)

There are three main inspections techniques performed using lasers: Holography, Shearograpy and profilometry.

LM Techniques

Holographic Testing

Holographic testing compares a part's image with an undamaged reference sample taken earlier. A laser scans the part surface to detect changes as it deforms under stresses of various kind. The laser beam is reflected, as it scans across the surface, back into the sensors that can then record differences in the surface. It results in a topographical map-like visualization with extreme accuracy, in the order of fractions of microns. This technology is able to detect and evaluate residual stresses, disbands, delaminations, cracks and voids.

Laser Profilometry

Laser Profilometry uses a high-speed rotating laser light source equipped with a miniature optics, to scan the internal diameter surface of a tube, and a computer with high-speed digital signal processing software. This technique is used to detect, in tubes and pipes cracks, pitting, erosion and corrosion. The surface is scanned in two dimensions and a lens focuses the reflected light onto a photo detector, resulting in a signal proportional to the spot position in its image plane.

The resulting data is a high-resolution three-dimensional image of the part surface (the surface topography of the part), generating by the change in position (due to parallax) of the focal spot on the photo detector as the distance from the laser to the ID surface change.

Laser Shearography

Laser Shearography compares two images, taken during the application of laser light to the surface of the part, one at rest and one of the parts being tested. The image is recorded using a CCD and stored on a computer. The two patterns are superimposed and defects, if present, can be revealed by the patterns developed. This method has the great advantage of the high resolution, allowing defects of few micrometers in size to be detected.

Leak Testing (LT)

It detects through leaks using one of the four major LT techniques: Bubble, Pressure Change, Halogen Diode and Mass Spectrometer Testing, which will be briefly described below.

LT Techniques

Bubble Leak Testing

It relies on the visual detection of a gas (usually air) leaking from a pressurized system.

The application of this technique changes in relation to the size of the part needing inspection. It's not possible to submerge large objects, so they will be inspected by pressurizing and spraying them with a soap solution that create bubbles to the area being tested, while small parts can be pressurized and immersed in a tank of liquid. For large flat surface the pressurizing effect will be created using a vacuum box, which create a negative pressure from the inspection side. The location of the leak will be revealed by the formation of bubbles.

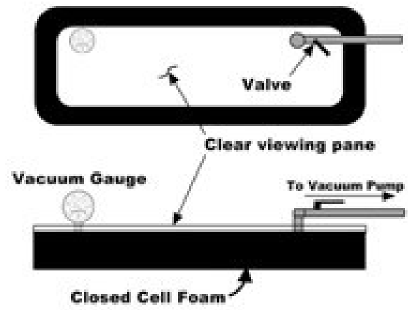

Figure 3.15 Basic schematic of a vacuum box.

Pressure Change Testing

Pressure Change Testing it's possible only in closed systems. A variation of pressure (either positive or negative) is imposed in the system by either pressurizing it or pulling a vacuum, then the evolution of the pressure of the system is monitored. Leak in the system are indicated by loss of pressure or vacuum over a set period of time. The temperature is monitored too, since change in temperature can lead to variation in pressure.

Halogen Diode Testing

Halogen Diode Testing use a halogen diode detection unit to locate leaks in systems pressurized with a mixture of air and a halogen-based tracer gas.

Mass Spectrometer Testing

Mass Spectrometer Testing involves different techniques, all involving a mass spectrometer to analyze samples of gas. It can either be done by surveying with a sniffer the surfaces of a pressurized test part or by creating a vacuum within the test chamber. In the first case the part is pressurized with a helium or a helium/air mixture within a test chamber, then the sniffer sends an air sample back to the spectrometer, while in the second a vacuum is created within the test chamber so that the gas is drawn from the system to the chamber through any leaks. The spectrometer is used to sample the vacuum chamber and any helium present will be ionized, allowing even very small amounts of helium to be detectable.

Magnetic Flux Leakage (MFL)

Magnetic Flux Leakage can be used for tank floor inspection, piping and tubing inspection and other. It works analyzing the anomalies created by discontinuities in normal flux pattern in ferrous material saturated by magnetic field. Tank floor inspection use a combination of multiple magnetic field generators (called "bridges") and sensors located side by side across the front of the machine. (as shown in Figure 3.16). The magnetic field generated by the bridges saturate the tank floor, and any leakage of field generated by loss of material (due to pitting or corrosion) or reduction in thickness can be picked up by the sensors.

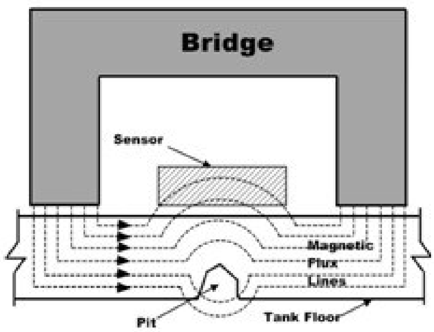

Figure 3.16 Sensor positioning in a magnetic flux leakage testing method.

For tubing and piping inspection an inspection head is used, which is made up of a position transducer and a drive, and a sensor coil. These are connected by cable back to the power source and a computer for signal processing. The head, placed around the part to be inspected, have the drive coil energized which results in the creation of a magnetic field in the part. The head is then moved along the length of the part, and any change in the magnetic flux density caused by variations in the wall thickness can be picked up by the sensors and recorded into the computer. A position transducer is used to locate every signal so that the area in which a defect is detected can be marked for further evaluation. One of the great advantages of this technique is the possibility to be performed without removing the insulation, which results in a fast and economical way to inspect pipe or tubing of long runs.

On very basic machines, each sensor will be connected to an audio and/or visual display that lets the operator know there is an indication; more advanced machines can have both visual displays and recording capability so that the results can be stored, analyzed and compared to earlier results to monitor discontinuity growth.

Neutron Radiographic Testing (NR)

Unlike conventional radiography (gamma or x-ray based), neutron radiography uses as a penetrating medium an intense beam of low energy neutrons. Neutrons penetrate most metallic materials (they appear transparent on the resulting image) but are attenuated by materials with a high hydrogen content, like most organic materials and water. These properties allow them to be seen even if included in the component being inspected. This technology can be used in combination with conventional radiography, making visible both the structural and internal components of the test piece.

Thermal/Infrared Testing (IR)

Thermal/infrared testing measure how heat flows through, to or from an object, measuring the surface temperatures based on the infrared radiation emitted by the object itself. It's useful to detect various detrimental conditions, such as inclusions, voids, delaminations, corrosion damages and disbands. To detect the infrared radiations are used thermal imaging devices, also called infrared camera, since most of the radiations are longer in wavelength than visible light.

Some prescriptions are to be followed in order to obtain an accurate measurement. For example, the part being investigated should be in direct line of sight with the camera, with nothing interposed between the parts and the camera's lens.

Vibration Analysis (VA)

Vibration analysis monitors the behavior of rotating machinery, monitoring its vibration signatures and analyzing the subsequent data to determine the condition of that equipment.

Usually three kind of data are acquired: displacements, velocity and accelerations, each one with its relative sensor. Different data lead to the possibilities of knowing different aspects of the behavior of the part.

Displacement detect changes in clearance tolerances and shaft motion and are detected with sensors that uses eddy current, one sensor per axis.

Velocity sensors are commonly used to detect the speed with which the axis is rotating. Older and basic ones use a magnet-coil combination, which generate an electric signal through the movement in a magnetic field, while more sophisticated ones use time-of-flight technology.

Accelerometers are used to detect vibrations and dynamic behavior of moving components or assembly. Basic ones use the low voltage current generated by a piezoelectric crystal during its moving. A piezoelectric crystal converts sound waves to electrical impulses, and vice versa, and so it does with vibrations. The low voltage current is passed through a pre-amplifier and sent to a recording device.

4 Digital Image Correlation

4.1 Introduction and general overview

Generally speaking, the term "digital image correlation" refers to the class of non-contacting methods that acquire images of an object, store images in digital form and perform image analysis to extract full-field shape, deformation and/or motion measurements [26].

More specifically to this paper it can be described as an optical method that employs tracking and image registration techniques for accurate 2D and 3D measurements of changes in images. Being often used to measure full-field displacement and strains, it is widely applied in many areas of science and engineering. It has the ability to provide both local and average data of the test subject, allowing to gather a greater amount of information about the fine details of deformation during mechanical test, compared to traditional collection methods (such as extensometers and strain gauges).

In this paper DIC methods are interesting because of their nature of being optically-based technique with which it is possible to measure the evolving full-field 2D coordinates on the surface of a test piece during a mechanical experiment. Once obtained, the coordinate fields allow to calculate derived field quantities-of interests, specifically displacements, strains and strain rates. DIC estimates full-field coordinates and displacements from a sequence of digital images taken of a pattern on the surface of a test piece, by solving an optimization problem, typically based on a transport model such as optical flow [27].

In order to obtain any kind of DIC measurements the pattern on the surface of the test piece is expected to follow the deformation of the underlying test piece. A set of full-field coordinates, representative of the shape, motion and deformation of the surface of the test piece can be obtained correlating the images of the piece taken during the test. To acquire 2D coordinates of the surface a single camera system can be used, and this setup is known as 2D-DIC. Every lens/camera system needs to be calibrated before any measurement is made, and this procedure is conduct using imaging features of known separation lengths, usually called calibration targets. The calibration is needed to correct for distortions caused by the lens or others.

The two most common categories of DIC methods implemented in the software developed to perform this correlation are known as local and global. A local method considers the coordinate solution at a point to be dependent only on a small subset of the image in the vicinity of that point, while being independent of the solution at all other point of interest. On the other hand, the solution at one point in the global method has some dependence on the solution at other points in the vicinity of the point of interest. Being the most used, we only refer to local methods.

A user-defined region-of-interest within the images is analyzed by the software. This region contains a set of interrogation (or measurement) points. In local DIC, each interrogation point is centered within a subset of the image, and some regular spacing (step size) is introduced between these interrogation point. Overlapping may happen between neighboring subsets.

A numerical correlation is performed between the image before deformation, called reference image, and the images taken during/after motion. This correlation is performed by first approximating the pattern in each subset using an interpolant function, and then allowing that function to deform from the reference image based on a subset shape function. To perform the matching between subsets in the reference image with the corresponding subset in the deformed/translated images a combination of a matching criterion and subset weights is used.

With the resulting data is possible to calculate various derived field quantities, the most common (and interesting for the aim of this paper) being strains.

As will be better illustrated later in this chapter, the measurement setup and the data processing parameters both influence the potential bias errors and the noise floor (the minimum resolution achievable), therefore no DIC experiment is complete without the uncertainty quantification analysis and the subsequent determination of the resolution of the quantities of interests.

The result will be a full field description of displacements (and the derived quantities of interests) induced by the experiment in a test piece, along with the uncertainties of those measurements.

The purpose of this paper is not to write a DIC algorithm, but to understand the methodology and investigate the applicability and the results, so the focus will be on how to obtain the best accuracy using the method.

4.2 The DIC process

To obtain a rigorous and reliable mathematical characterization of the captured images it is important to consider how said images are captured and recorded.

The light reflected on the test subject go through a series of camera lenses, and is then converted into digital signals by some sort of light sensor. The digital signal is then analyzed by the DIC mathematical algorithm and reported in data accessible to the final user.

Along all these processes and transformations many variables have influence on the results. The firsts must consider the way the light enter the recording device, and the deformations induced to the light by the lens used in the recorded device and the relative position of sensor and focal point. Therefore, the developing of any imaging correlation algorithm must include concepts of geometrical optics.

As illustrated in [26] this developing starts with the definition and analysis of a simple optical system that consist of a single, ideal lens (thin lens), which can be a good approximations under some conditions, moving then to more realistic model of thick lens. The objective is to use ray optics to obtain the formulae relating object positions to sensor locations. It is possible to combine and simplify these two optical models into the so-called pinhole model, under the hypothesis of neglecting the effect of blur due to defocus. The pinhole projection models are applied to develop a formulation including variations in the image caused by the recording device. These include the effect of distortion on image positions, rigid body transformation between several coordinate systems used to represent various elements in the imaging process and the transformation between image plane coordinates and skewed sensor coordinates.

Another factor to consider is the recording device. Giving the topic of this paper only the single camera models will be taken into account. As defined in [26] a camera is typically an opto-electronic device consisting of several sub-systems. The combination of a series of lenses, optical filters and shuttering elements forms the optics, which collect light from the object and focus the image onto the sensor plane. The light is then acquired and processed into digital images by the camera hardware. The incident illumination is converted into an electrical signal by some sort of sensor, such as for example a CCD (charge coupled device). The signal coming from the CCD is converted, using an A/D device, into an array of discrete digital intensity data. This digitization and storage process may happen in a hardware integrated into the camera or in an external device.

In order to acquire and then obtain reliable data the recording setup must be calibrated. Being so the computer vision community has found great interest in the problem of camera calibration, and a large number of calibration methods have been proposed over the years. Some linear calibration methods algorithm only requires a planar calibration target to implement them, making them attractive to the final user for their simplicity. Every camera calibration procedure must be adapted to accommodate changes in the camera model, measurement objective function or distortion correction procedure.

Both the two-dimensional (2D) and three-dimensional (3D) computer vision employ the aforementioned pinhole camera model, along with a distortion models and general optimization procedures. The basic hypothesis for two-dimensional computer vision is that the motions of a planar object occur within the object plane. This requirement is usually observed, since in most practical 2D applications the object plane is nominally parallel to the camera sensor plane.

As previously mentioned, in order to correct modest inaccuracies in a target grid or camera lens a full camera calibration procedure can be used. This procedure can be greatly simplified by using high quality lenses combined with a scientific grade digital image acquisition system, since this setup will likely reduce the effects of image distortion. Furthermore, correction parameter for the most used camera and lenses have generally been developed by the users, and are available for both commercial and free-to-use software.

Image matching in DIC

Digital image correlation takes advantage of image matching techniques to detect changes in images. Image matching is a discipline of computer vision developed with the goal of finding correspondence and similarity between different images, and is used in many different applications, like industrial process control, automatic object recognition, geological mapping, autonomous guided vehicles and stereo vision. Giving the amount of different applications a wide variety of approaches and algorithms are used, with many specialized to a given task. Digital image correlation is one of those, for which the algorithms are developed to take the physics of the underlying deformation processes into account. It must be noted that in engineering applications the resolutions are much higher compared to most of the other, giving the miniscule motions that are often studied. For example, in order to accurately measure the stress-strain curve for many engineering materials, length changes on the order of 10^{-5} m/m have to be resolved. This have led to the development of many algorithms specifically designed to provide high resolution with minimal systematic errors.

In order to obtain an effective image matching algorithm some limitations intrinsic to the digital nature of the data analyzed must be overcome. The grey value of a single pixel in an image can be found at thousands of other pixels in a different image, making it generally impossible to find the correspondence between single pixels in two or more images. The correspondence is then found analyzing a small neighborhood around the pixel of interest. This limitation is called “aperture problem”, which is a special case of the more general correspondence problem, giving that there are many situations in which a unique correspondence between features in two images cannot be established. The object surface must possess certain properties in order to solve the correspondence problem uniquely. The preferred textures are random, giving that the repeating textures can lead to misregistration problems and the ideal surface texture should be isotropic. The patterns used in digital image correlation must adhere to the surface and deform with it to avoid loss of correlation even under large translations and deformations.

Some examples of speckle patterns are shown in Figure 4.1.

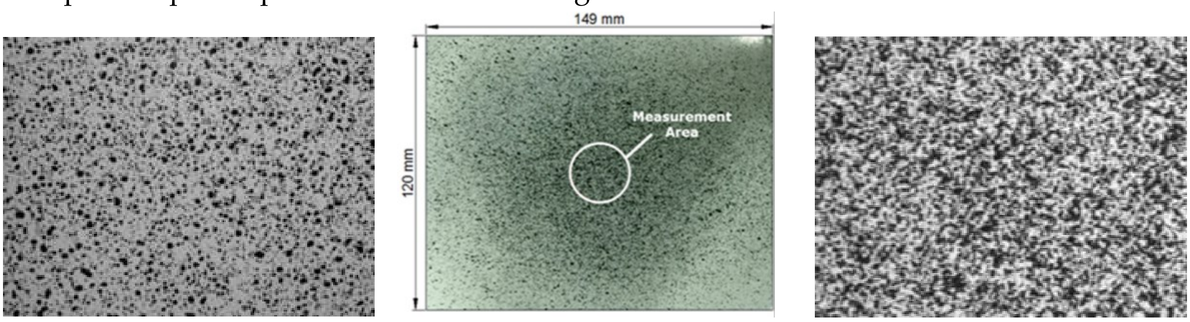

Figure 4.1 Examples of typical speckle patterns [26], [28].

Good speckle patterns have high information content and, since the entire surface is textured, the information for pattern matching is not only available on a comparatively sparse grid but everywhere on the surface. This allows the use of a relatively small aperture for pattern matching, commonly referred to as a subset or window.

To obtain an image matching algorithm, it is needed to translate into mathematical terms what for a human observer is a relatively simple task namely the ability to identify motion in successive images. This is not a problem of easy solution, and many different approaches have been developed in time. Worth mentioning are the differential methods, in which is made clear that motion estimation in regions of constant gray values is not possible, and the template matching, which is based on minimizing the gray value difference between a small subset from one image (template) and a displaced copy in another image.

Introducing the subset shape functions

The previously mentioned algorithms are limited to the determination of the average in-plane displacement of a typically square subset between two images. In the usual engineering applications, the specimen might experience rotation, compression, shear or elongation, therefore the measurement of complex displacement field is interesting. As a result of those transformation an initially square reference subset might assume a rather distorted shape in a later image after deformation. The phenomenon in which the similarity between the original subset and the transformed one decreases is often time referred to as decorrelation.

By the incorporation of the subset shape functions into the matching algorithm an iterative digital image correlation algorithm can easily cope with complex deformation fields, making it the preferred choice for stereo matching and deformation measurements. As a result of the analysis of polynomial shape functions has been concluded that subset shape functions behave as low-pass filters applied to the displacement fields encoded in the images, resulting in a limitation of the spatial resolution of the method. This limitation must be considered by the experimentalist, whom must apply appropriate speckle patterns such that small subsets can be used for matching. This is particularly true when affine shape functions are used to approximate non-linear displacement fields.

Pattern matching: Changes in intensity and efficiency optimization

It is critical to develop effective matching algorithms able to accurately measure the correct correspondence between subsets even if the intensity values undergo significant changes, because differences between the intensity of images recorded at different times or coming from different devices can exists even under ideal experimental conditions. These changes may be localized and not affecting the entirety of the image in the same way, and may be caused by various reasons, such as changes in specimen reflectivity due to strain, changes in lighting or changes in the orientation of the specimen. In stereo imaging this is of particular concern, giving that difference in camera angle to the object results in localized brightness differences in most cases. Optimization criteria have been developed to permit accurate template matching even with the above-mentioned differences, based on the assumption that all lighting changes are approximately constant over the size scale of the subset.

Approaching any calculation algorithms, the computational efficiency is of central importance, and must be increased as much as possible. This is particularly true with digital image correlation applications, being a full-field method, therefore involving the need to compute a large number of displacement vectors throughout the image. As an example, approximately 40,000 displacement vectors must be computed to run analysis on 5 pixels centers in a typical 1024 ×1024 pixels image. As higher resolution cameras are being increasingly available and inexpensive, the number of data points that need to be analyzed keeps increasing. Besides, during dynamic deformations events usually even several hundred images can be captured, with the resulting need to repeat the image matching algorithm several million times.

Matching bias: Interpolation bias

Generally, the phase accuracy of the interpolation filter used to reconstruct gray values at non integer locations strongly influence the accuracy of digital image correlations methods. Analyzing the interpolation bias in a numerical study [26] can be useful to understand how much error one can expect due to the phase errors in commonly used interpolation filters. The quality of the data is important, since the input data must not contain any interpolation bias itself to isolate the interpolation bias due to filters.

For this analysis a series of input images have been generated by applying a Fourier filter. A set of 20 images were generated for each pattern, with a subpixel shift increments of 0.05 pixel between images. A digital image correlation algorithm, implementing different interpolation filters, has been used to determine the shift of each image with respect to the original one. The images were taken from specimens prepared for tension testing using black and white spray paint. One of the images presents a very fine-grained texture, while the other present much larger speckle size. The image with the fine texture results in an interpolation bias an order of magnitude higher compared to the other. For the fine texture, cubic B-spline interpolation produces interpolation bias of approximately 1/40 pixel, and the optimized four coefficient interpolation filter approximately 1/50 pixel. Despite their computational efficiency the use of four-tap filters should be avoided because of the non-acceptable amount of bias. For pattern with small speckles a bias well below 1/200 pixel is achievable using optimized six and eight coefficient filters, with the eight one showing approximately half the error compared to the six coefficients filter, which justifies the additional computational expense.

Strain measurements, which are the purpose of the use of the DIC in this paper, are directly influenced by the interpolation bias. If, instead of the true displacement $u_t(x)$, a biased displacement $u_b(x) = u_t(x) + \Delta u(x)$ is measured, the resulting strain becomes

$$\varepsilon_b = \frac{\partial u_b(x)}{\partial x} = \varepsilon_t + \frac{\partial \Delta u}{\partial x} = \varepsilon_t + \frac{\partial \Delta u}{\partial u_t}\frac{\partial u_t}{\partial x}$$

The relative strain bias $\Delta\varepsilon_b = (\varepsilon_b - \varepsilon_t)/\varepsilon_t$ can now be found as

$$\Delta\varepsilon_b = \frac{\partial \Delta u}{\partial u}$$

i.e., the relative bias in strain due to interpolation bias is proportional to the slope of the displacement bias shown in Figure 4.2.

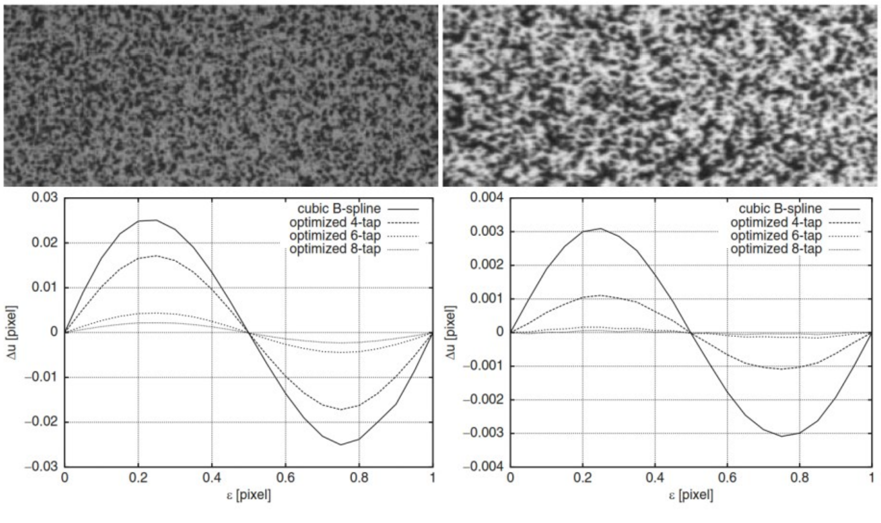

Figure 4.2 Comparison of interpolation bias as a function of subpixel position for different interpolation filters. The pattern used is shown above the two plots.

An absolute error of 1/40th of a pixel, as produced by cubic B-spline interpolation for the finer of the two speckle patterns, may seem reasonable and acceptable in some applications. In reality the slope of the bias approaches 20% at the integer positions, meaning that a strain errors of 20% of the actual strain level must be expected when cubic B-spline interpolation is used for this particular speckle pattern. This again emphasizes the importance of proper interpolation filters in digital image correlation applications.

Matching bias: Bias due to noise

Giving the electronic nature of the recording procedure, images used for DIC are always contaminated by some noise.

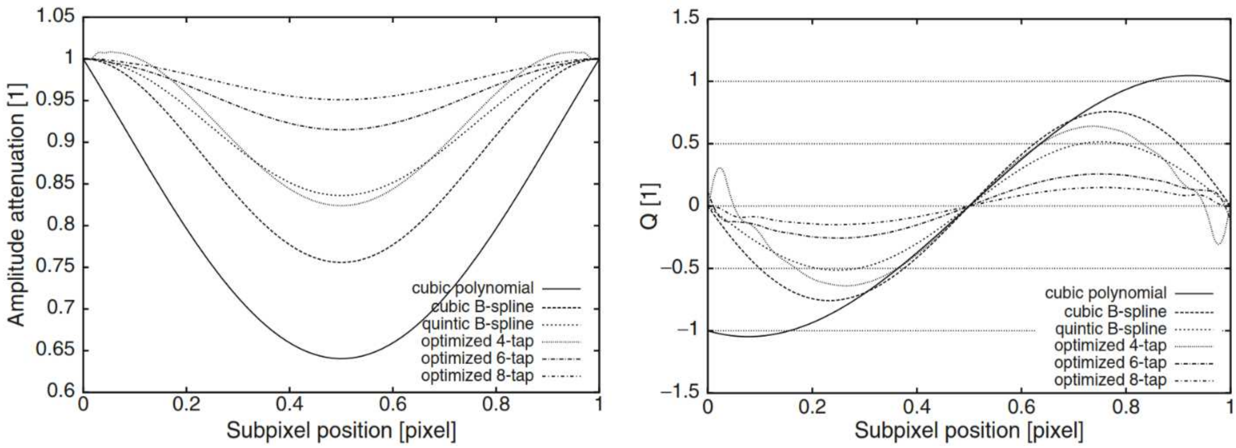

Figure 4.3 Integral of the squared amplitude attenuation of various interpolation filters as a function of subpixel position (left) and the corresponding derivatives with respect to the subpixel position (right) [26].

Different interpolation algorithms behave in different ways. As illustrated in Figure 4.2, cubic polynomial interpolation introduces the highest amount of bias, and, unlike B-spline filters, has the unfortunate property of a discontinuity at the integer location. While the optimized interpolation filters family shows the least amount of bias, the four-tap filter shows small oscillations near the integer position. The optimized filters are then the preferred choice for digital image correlation, giving their substantially improved phase accuracy and the significantly less bias compared to the B-spline filters with the same support.

4.3 DIC application overview

The main purpose of a DIC algorithm is tracking a pattern in a sequence of images. As previously introduced, this pattern is also called "speckle pattern".

In its most basic form generic DIC experiment is comprised of three steps [29]:

1) Creation or definition of the pattern on the sample (for the following tracking) and experimental setup preparation;
2) Acquisition of images of the sample during the test (at different deformation or motion instant);
3) Processing of the images to obtain the sample surface's displacements.

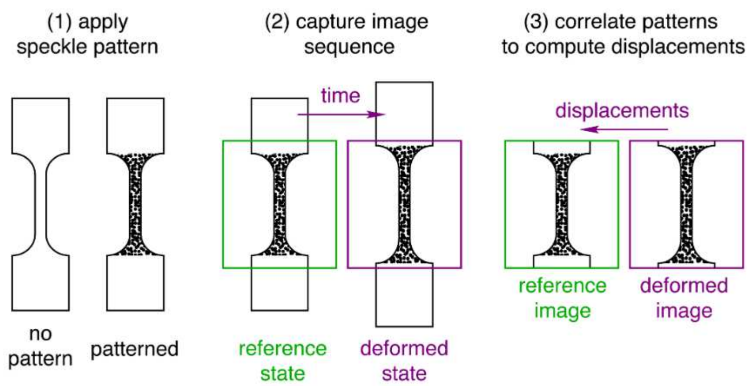

Figure 4.4: Three main steps of DIC for strain analysis.

(N.B.: All the images [30] in this section are licensed under Creative Commons Attribution 4.0 International (CC-BY-4.0) [31], unless otherwise stated.)

Prior to the test a reference image must be acquired, consisting of the test piece positioned on the test machine with the speckle pattern applied (or clearly visible, if made of the piece bare surface). This will be the baseline to which the second image will be compared. DIC algorithm will then calculate the displacements of the pattern between the reference and deformed images, after matching the pattern between the two images.

The following is a simplified model of a DIC analysis:

1. A reference image is taken, provided with a natural or printed pattern of dots used for tracking.
2. Inside the pattern a subset (a portion) is selected to be used for the tracking procedure.
3. The center of the subset on the reference image is defined, and the displacement will be calculated from that point (in red in Figure 4.5).
4. After deformation the subset in the deformed image is matched to the subset from the reference image.
5. Once the matching process is completed the subset center's relative displacement between the two images is calculated by the DIC algorithm.

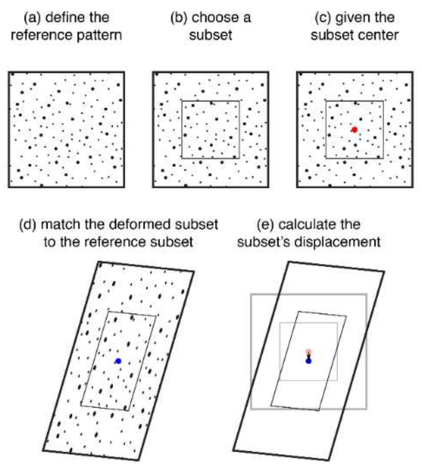

Figure 4.5 Analysis of the displacement for a single subset.

In Figure 4.5 the displacement is represented as the difference between the red (reference) and blue (after deformation) dots. This operation needs to be then extended to multiple subsets and DIC points.

While in the previous example only one subset's displacement has been computed, by tracking multiple subsets DIC allow the computing of a field of displacements. As an example, in Figure 4.6 four equally sized subsets, arranged in a two by two grid, are analyzed using the same procedure as before. This result in additional four more points with displacement information, obtaining a total of five data points.

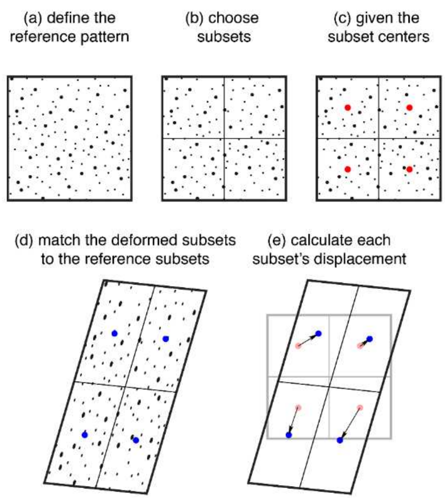

Figure 4.6 Analysis of the displacement for multiple subsets.

For every subset there is a point for which the displacements have been calculated. As made clear in Figure 4.7 there are five different subsets, resulting in five different points. These are also called DIC points. Being the displacement at each of these point a vector, the components of these vectors can be decomposed.

There are two different possible analysis: 2D-DIC and 3D-DIC. In a two-dimensional analysis of displacement, the Cartesian coordinate system in which the components are written is composed of vertical displacement (v) and horizontal displacement (u). The third-dimension displacement (w) can also be measured with a more articulate type of DIC that uses triangulation. The 3D-DIC will only be briefly mentioned in this paper.

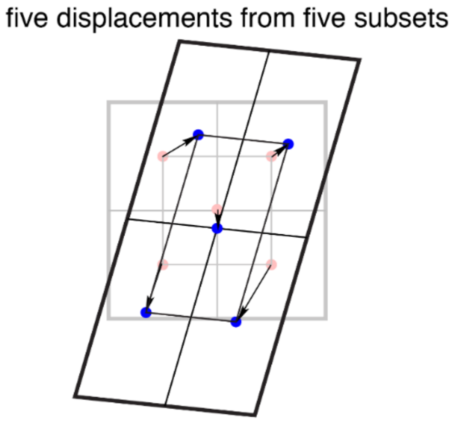

Figure 4.7 Displacements identification in a five subsets image.

For the purpose of this paper DIC is utilized to study the mechanical properties of solid components, with particular interest in uniaxial tension tests, in which the deformation of a material is related to the force applied. The classic methods to measure said deformation are strain gauges and extensometers, with the big limitations of these providing a localized single measurement of displacement in the material. DIC can be used too, and being a full-field method has the ability of providing many displacement measurements across the material. Knowing the displacement across the entire material this method can provide information on local deformations caused by localized phenomena, like cracking, stress concentrations, plastic instabilities and inhomogeneity.

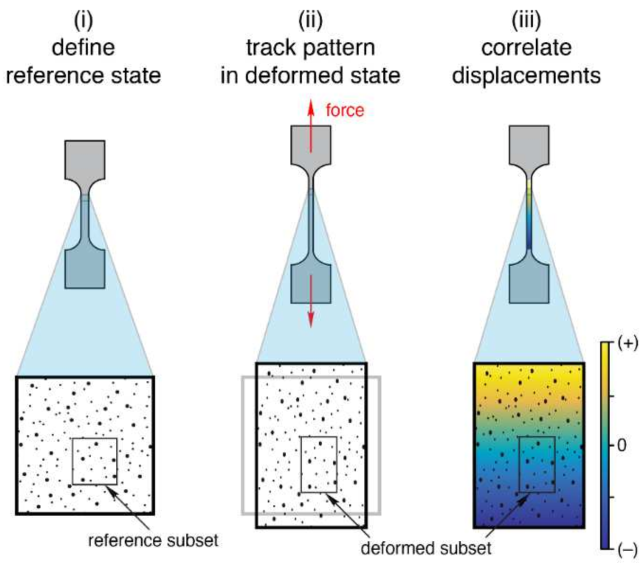

Figure 4.8 Modifications in the subset during a tensile strength test.

Choosing the appropriate parameters: Step and subset sizes.

There are many parameters to be chosen by the operator during a DIC calculation. Two of the main ones are the step size and the subset size, both measured in units of pixels. The step size is the distance between subset centers, while the subset size is the dimension, meaning the height and width, of the subset square in the reference image. As illustrated in [26], the main factor for choosing these dimensions is that each subset should contain at least three speckles.

There are other factors to be considered while making the choice of the subset size. While smaller subsets result in better spatial resolution, bigger ones give better pattern matching. This because smaller subsets require less spatial smoothing of the image data, and bigger ones provide more uniqueness for a larger area of features in the image. This require to decide in advance which one of these behaviors is preferred for the analysis. On top of that, larger subsets require more computation time. Meanwhile the step size has a much stronger effect on spatial resolution than the subset size because smaller step sizes yield more DIC data points and thus higher spatial resolution. The diagram below shows a range of step sizes for the same field of view and subset sizes.

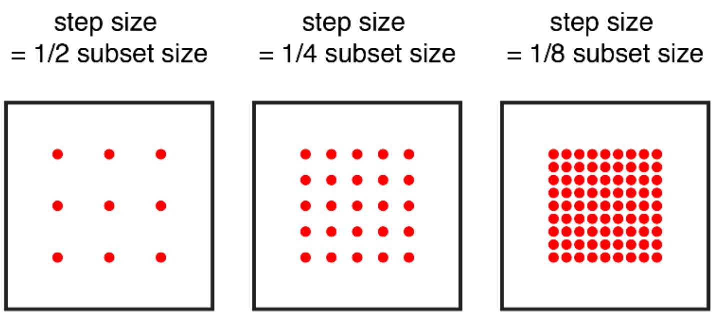

Figure 4.9 Range of step sizes for the same field of view and subset size.

Limits in spatial and temporal resolution

Since for our purposes DIC is used to obtain displacements it is worth mentioning that as in every optical method the smallest possible displacement measurement is limited by the quality of the experiment's images. The DIC algorithms themselves are able of detecting sub-pixel displacements, on the order of 0.01 px, using interpolation on the image data. The actual smallest displacement measurements that can be expected from DIC are on the order of 0.1 px. This is known as noise floor, and is caused by the inevitable experimental variables error proper of any test.

This limit has a direct influence on the exposure time. To avoid a blurred image, and the resulting loss in displacement accuracy, these should be captured with an exposure time that limits the sample motion during the exposure time to less than the noise floor, or better to half of it.

Influence in strain calculations

If, such as is the case of this paper, computing strains is the purpose of the displacements obtained using DIC, it should be known that filtering operators can lead to errors in the results. Generally, spatial strains are computed from the displacements with a spatial derivative that has a filtering operator. Highly-localized deformations, with discontinuities or sharp features, can be blurred by the filtering in the strain calculation, resulting in the smoothing of those feature by the spatial filtering, and key phenomena like slip bands can be hidden [32].

4.4 DIC algorithms categories

There are multiple ways to categorize DIC algorithms. The most used are by the dimensions of the calculated displacements and by the pattern matching technique.

Two-dimensional DIC (also known as 2-D DIC) use images collected by just one camera, for which only two dimensions of the displacements can be known. Once multiples cameras are used depth can be evaluated with triangulation, and this technique is called three dimensional DIC. Clearly the basic assumption of 2-D DIC has to be that the sample's deformations are constrained to a plane that is parallel to the camera. Being this rule not always respected in real life measurements, a large amount of error can be expected from out-of-plane motion [33]. Another main reason of error found in DIC measurements are images distortions, caused for example by the barrel distortions of camera lenses. The specimen may contain geometric discontinuities or gradients in material properties without affecting the test result's quality.

To obtain out of plane deformations for 3-D DIC analysis triangulation is used, and no error is introduced by these deformations as long as the sample remains in focus. As for the above-mentioned lens distortions, in 3-D DIC these are corrected through a calibration procedure. This process also allows to connect the length scale of the images to the physical length scale of the imaging system, while in 2-D DIC the length scale is introduced by operating a conversion between the pixel size of the images to the physical size of the images, a process inherently less accurate.

Despite the misleading name, 3-D DIC cannot measure displacements within the three-dimensional volume of a material but only on the surface. To obtain the measurements within a solid the images of the inside of the material must be taken, requiring specialized imaging systems like X-ray tomography. This method is called digital volume correlation, and is the extension of DIC from pixels to voxels, which are three-dimensional pixels, which changes in the algorithms to allow the capture of displacements through the volume. A comparison among 2-D DIC, 3-D DIC, and DVC is illustrated below.

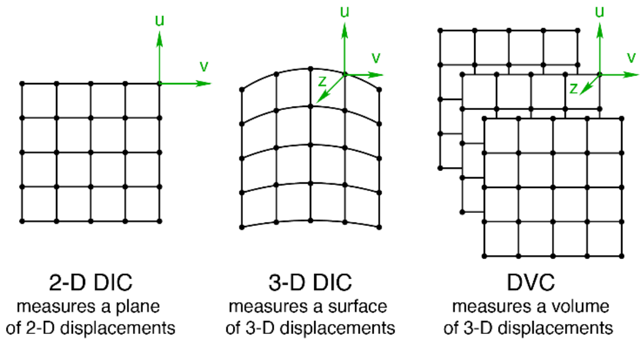

Figure 4.10 Graphical representation of 2-D, 3-D DIC and DVC.

A second way to categorize DIC algorithms is by the pattern matching technique. Local DIC was the first to be introduced, and is the more popular. Local DIC separate the pattern into multiple subsets that are individually matched, while global DIC matches the pattern in one go using a finite-element based approach.

4.5 Speckle pattern: Characteristics and application

Being the components that DIC uses to detect translations and deformations, the nature and quality of the speckle pattern must be taken into particular consideration.

The speckle pattern is the set of features on the sample surface that DIC tracks to match reference and deformed images. If a sample's surface has the right features these form a natural speckle pattern, but in most cases these are artificially applied to the sample. Since the quality of DIC results is strongly dependent on the speckle pattern a series of guidelines can be suggested, some generic and some more specific, dictating the characteristics possessed by an optimum speckle pattern [30].

1. The pattern covers the sample surface in the area of interest.
2. The pattern moves and deforms with the sample, but does not exert a significant mechanical stress on it, meaning that the pattern describe accurately the sample's deformations without impeding any movement.
3. The features that comprise the pattern (the *speckles*) are random in position but uniform in size.
4. There are also requirements to the dimensions of the speckles. Their size must be at least 3-by-3 pixels and less than 7-by-7. The smaller end of the spectrum to avoid aliasing [34], the bigger to achieve a relatively high density of DIC points [35]. Said sizes are not averages but are rather the range of the smallest and largest speckles [35].
5. The pattern has good grayscale contrast, which reduces error [26]. One way to visualize this contrast is a histogram: with the number of pixels plotted with respect to grayscale level, the pattern has a mix of dark and bright pixels, indicated by two peaks in the histogram's spectrum, and the separation between the two peaks is broad. Ideally, the two peaks look like a bimodal Gaussian distribution. Nowadays the histogram visualization is easily accessible in real time even in low-end digital cameras.
6. To help the camera sensor avoiding aliasing the speckle edges these should be softened rather than sharp and distinct with the background [36].
7. The pattern is stable in the testing environment and for the duration of the test (especially important in high-temperature experiment).
8. The pattern has a speckle density of about 50%. When the pattern has either too few or too many speckles, then this results in features that are either too big or too small [35]. In Figure 4.11 are depicted examples of different densities.

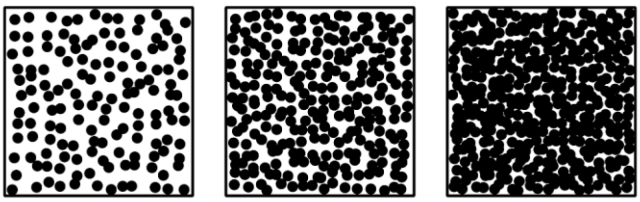

Figure 4.11 Examples of artificial speckle patterns generated with the Speckle Generator software from Correlated Solutions, Inc.

Speckle patterning techniques

While useful to avoid additional manipulation of the test piece, usually the natural pattern made by the piece's surface is not the best achievable. The main of many techniques available to apply artificial speckle patterns are listed below. Some of the most common ones are paint, inks (and dyes), powder particles and lithographed patterns.

Paint

Due to its accessibility, low costs and easy applicability painted speckle patterns are widely adopted. High quality speckle patterns can be obtained simply spraying paint on the test piece's surface. Since the best results are achieved having the most contrast possible only black and white paints are recommended, specifically black speckles on white background, since black paint maintains better contrast over white paint [37]. It is possible to take advantage of the different mechanical properties of paint at different moments of the drying process because as the paint dries it hardens, losing the ability to deform with the sample [38], so for tests imposing high deformations on the sample the experiment should be performed within 24 to 48 hours from the painting.

Another advantage of spray paint is the ability to produce a large range of speckle sizes, depending on the tool used to apply the paint. The most commons are cans of spray paint, which can produce large speckle, in the range of 100 to 1000 microns. Increasing the technology (and costs) of the tool the size of the speckle will decrease, with artist grade airbrushes allowing speckle size between 10 to 100 microns, with more pressure creating smaller speckles.

Inks and dyes

For extreme deformations, such as the ones found in hyper elastic material like polymers and elastomers, ink and dyes are used, since paint is not stretchy enough to track with the sample. Unlike paint ink and dyes tend to permeate the sample material's surface. These can be applied in many ways, such as spraying, masking or stamping, and can be used stencil to define the pattern.

Powder particles

Even if not on topic with this paper, it is worth knowing that some materials, if sticky or moist, may use powder particles as speckle pattern, working better than paint or dyes. As basecoat alumina or magnesium can be used, while for dark speckles the most popular choice is graphite powder. This kind of application can achieve smaller speckles than painted patterns, with powder particles smaller than 10 microns using a combination of filters and compressed air [39].

Lithographed patterns

Lithography combine a high degree of control in the microscale patterning [40] while allowing to achieve small speckle size.

To better illustrate as said before two examples are examined.

In Figure 4.12 on the left a carbon fiber that has been speckled with gold nanoparticles of around 50 nanometers in diameter. This is overall a good quality pattern, having both uniformly-sized speckles and random pattern positioning. However, there are occasional clumps of nanoparticles that would detract slightly from the correlation quality.

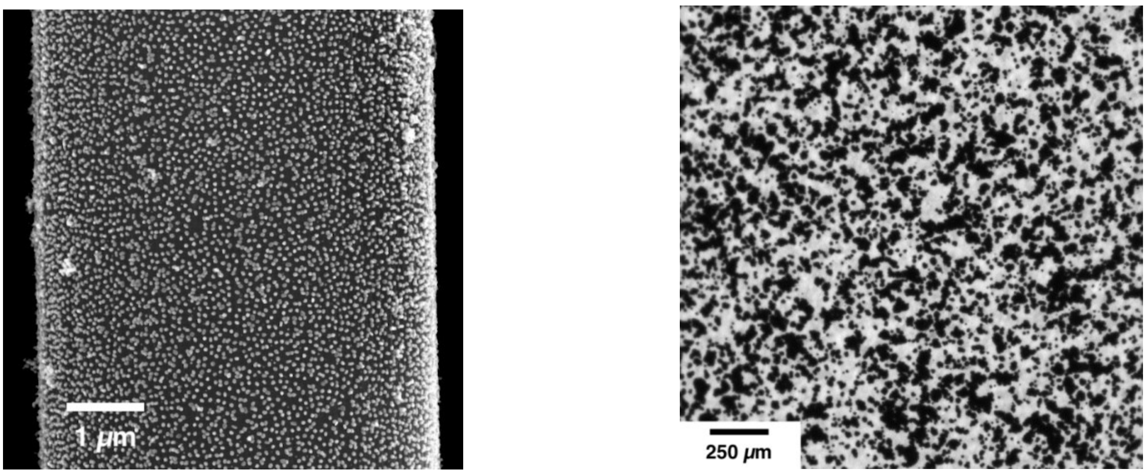

Figure 4.12 On the left: Carbon fiber speckled with gold particles. On the right: metal sample with airbrushed speckle pattern made of paint.

On the right is an airbrush-painted speckle pattern on a metal sample. This pattern, even if still providing a good randomness in the speckle positions suffers from non-uniform speckle size, with speckles too small and other too large. As already mentioned, the speckles should not be larger than 7 pixels and smaller than 3 (in diameter). This variations in dimensions will result in a worse spatial resolution than the maximum possible for the given field of view, even if this pattern would likely still correlate and produce results.

4.6 Image acquisition

Being an image-based method, the quality of DIC results are strongly and directly influenced by the quality of the images used for the analysis. As a result, generally speaking good images lead to good results, but there are some DIC-specific precautions for obtaining an optimized analysis.

The first consideration is selecting the appropriate image magnification, depending on the experiments and the length scale of the samples and phenomena being investigated. The algorithms for DIC are inherently length scale independent, so the physical length scale conversion arises from the image magnification. As a matter of fact, it is possible to perform DIC from the length scale of meters all the way down to single atoms. For the purpose of this paper cameras are used to capture DIC images, which are also the most commonly used devices. The right setup, therefore equipment, must be selected to obtain high quality data.

The following section illustrate a few selection criteria for optimized optical DIC systems, made of cameras, lenses and lights.

Cameras, lenses, and lights: Best practices.

- DIC algorithms have no use in color data, so black-and-white cameras are the best choice.
- The preferred qualities for the camera sensor are high dynamic range, high quantum efficiency and low noise.
- Telecentric lenses are to be preferred. These are low distortion lenses, in which the sample's magnification does not vary within the lens depth of field of view.
- Use mid-range apertures in lenses with adjustable apertures to minimize the distortions.
- Any unwanted movement must be avoided. The recording device must be rigidly mounted on its support, along with any cable.
- Multi-camera systems must have the same viewing area to facilitate the calibration
- The area of interest can be large, consequently its most important part must be the best-focused area.
- Lighting should be evenly distributed along the sample's area of interest, with enough light to achieve enough exposure but not too much, to avoid the introduction of saturated pixels, which preclude the ability of DIC to perform sub-pixel interpolation at that pixel.
- The test piece must be maintained thermally stable. Some kind of lighting, like halogen or high-intensity LEDs can generate a significant amount of heat.
- Heat waves can distort the images. Using a fan to blow air over the DIC setup is recommended to prevent said distortion [41].
- The use of polarizing filters to perform cross polarization increases contrast, decreases error, and attenuates saturated pixels that prevent sub-pixel correlation [42].

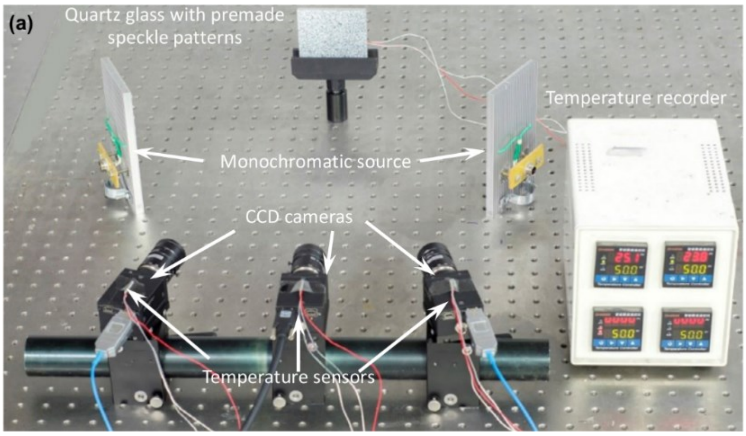

Figure 4.13: An example of a 3-D DIC system [43].

In Figure 4.13 three CCD cameras are visible in the center, with a set of two monochromatic source. (grey panels on the sides). Every component has its own temperature sensor.

4.7 Calibration procedures

To calibrate a 2-D DIC a line of known length is needed, since the calibration procedure is a length scale conversion from the pixel space of the DIC to the image's magnification. Small errors in the line length can create large errors in the resulting displacements, so for the line length measurement to calibrate the setup an accurate reference such as a precision ruler should be used.

For 3-D DIC, the cameras must be calibrated with respect to one another in space, so a line is no longer sufficient. A plane of known dimensions, or better a calibration grid, is therefore used, as illustrated in Figure 4.14.

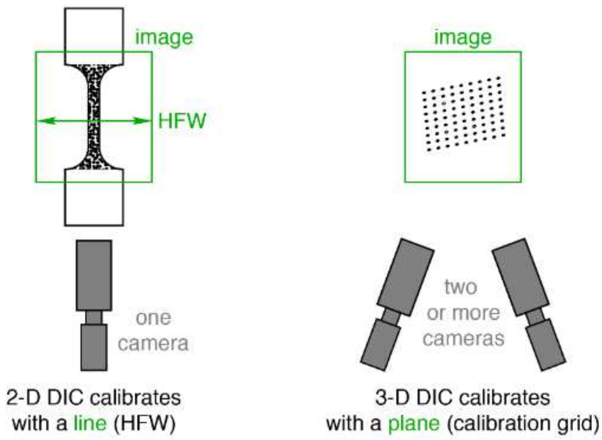

Figure 4.14 Calibration devices for 2-D and 3D DIC.

For 3-D DIC, the calibration procedure varies among DIC software packages, but general best-practices are listed below.

- The smaller the horizontal field width, the higher precision is required to the calibration grid, which must always be of rigid materials. For horizontal field width larger than 25 mm a printed grid on paper is good enough.
- Glass calibration grids needs backlighting with a diffuse or indirect source.
- During the calibration the highest the contrast the better the results. Set the light intensity accordingly (just before saturation).

- Usually between 25 to 50 calibration images are needed, each with the calibration grid moved and rotated in the field of view.
- The calibration grid must stay still during the acquisition of the images, so a stand of some sort is needed.

4.8 Method validation and error evaluation

Like for any measurement procedure, the accuracy of DIC results must be estimate. For DIC is particularly relevant since results can vary among setups, speckle patterns, correlation parameters and other conditions. While it is usually not possible (or very difficult) to evaluate the contributions of every individual error sources in DIC experiments, appropriate measurements allow to estimate the overall error of an experiment.

Among all the possible error evaluation and validation methods available the two more interesting are the following:

1. Using repeated, static images (no motion or deformation between images) it is possible to capture false positive errors, measuring the noise floor and speckle pattern. The mean and distribution of the displacements represent the noise floor, and because of noise and error the noise floor cannot be 0 but at best 0.1 px [44].
2. Compare the displacements (or strains) from DIC with a second measurement. Using precise rigid body translations on the sample from a trusted source is possible to obtain a direct comparison with displacements. These sources could be a precision linear stage or a Vernier micrometer.

Extensometer and strain gauges (for small strains) can be used to compare the resulting strains and deformations.

5 DIC on additive manufactured lattice components

Even if the focus of this paper is the application of DIC and the reliability of the resulting data, it had been deemed useful an overview of every analyzed article. This allow to illustrate every approach to the design of lattice structures, the purpose of the components and how any difficulties have been overcame, united with the adopted best practices. The knowledge of the purpose and characteristics of every components and its application lead to a better understanding of the reasons why the DIC analysis has been adopted.

5.1 Topology-optimized casing

In [45] the goal was to analyze the behavior of a casing-like geometry after a homogenization-based topology optimization, aimed at substituting the solid body with an optimized layout of lattice structures.

The optimization was performed to take advantage of the ability of AM to build designs otherwise impossible to fabricate, like internal lattice structures, allowing various benefits, such as great reductions of weight. For components that must satisfy a fixed surface profile, like casings, lattice structures provide a way to lightweight the underlying solid structure while supporting a skin with the desired profile, with the lattice density adjusted accordingly to functional and structural requirements. A standard topology optimization cannot provide adequate distributed support for the external skin, as shown in Figure 5.1.

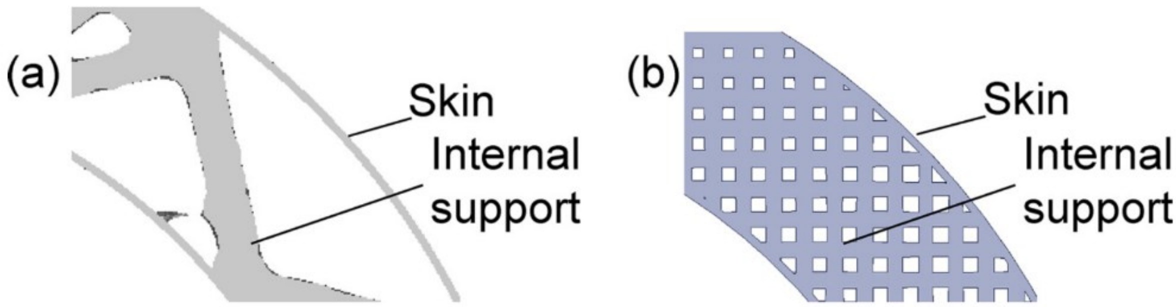

Figure 5.1 Supporting an external surface (skin) with internal support structure optimized via (a) standard SIMP or level set topology optimization and (b) lattice density homogenization.

To overcome the discrete behavior of lattice structures an asymptotic homogenization approach is used to describe the properties of both elasticity and yield strength in an average sense. This allow to create a volume with fixed exterior skin, filled with variable density lattice. With this approach there is no need to represent the internal lattice structures until a post-processing step, since optimization is performed on the effective density of the lattice. The unit cells are then created from ligaments with sizing corresponding to local optimized density.

The paper presents both wide-view and high-resolution digital image correlation for the inspection of lattice's deformation and failure. The ideal design was a casing, but the analyzed design was simplified to ease the experimental measurement, since the focus was on validating the design methodology and understanding the resulting mechanical behavior. The results can be extended to more realistic part designs and to future components obtained from machine with larger build platforms, so the fundamental relationships between design and metal powder bed additive manufacturing was investigated.

For more accuracy in the results the part was built in a single build, without welding or joining, so the size was selected to allow the build in a single piece in Inconel 718 in an EOS M290 DMLS machine.

The analyzed design is made of a ring-like component, representing a 60 mm section of the casing, with two 39 mm holes and flats near the holes, to allow the machine to grip the piece from the inside with two bolts and flat plate washers to evenly distribute the bolt force as a pressure loading.

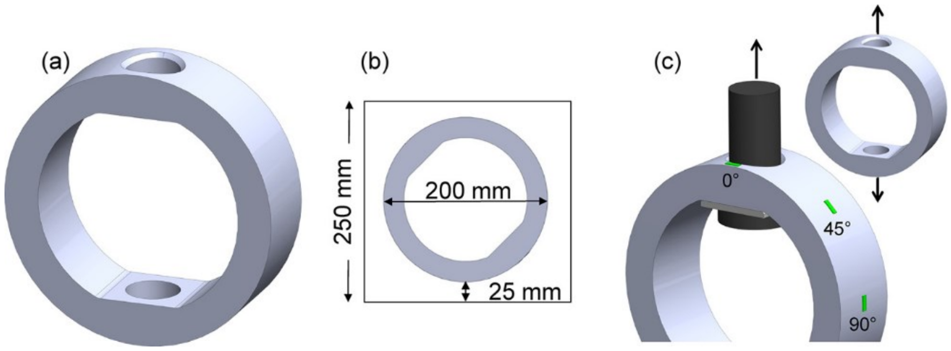

Figure 5.2 (a) Rendering of the test piece. (b) Comparison between the build chamber of EOS M290 and the test subject. (c) Loading plan including bolt and washer, with strain gauge placement labeled according to angular position.

As showed in Figure 5.2 (c) strain gauges were placed in three different positions on the outer surface. DIC was used during mechanical testing, acquiring images of the front and back faces of the casing, normal to the primary cylindrical axis.

To better understand the behavior of the optimized component a finite element analysis was performed using ANSYS Workbench v17 on the solid casing geometry, using material's properties identified in previous in-house tests on additively manufactured coupons of Inconel 718. The regions of highest relative stress are located on the inner and outer surfaces at the top near the bolt hole and at the bottom near the 90° position.

A subsequent analysis defined the lattice density necessary to guarantee the appropriate mechanical behavior. High lattice density is required near the bolt hole and near the bottom (90° position), corresponding to the regions of high stress, while lower density was allowed elsewhere.

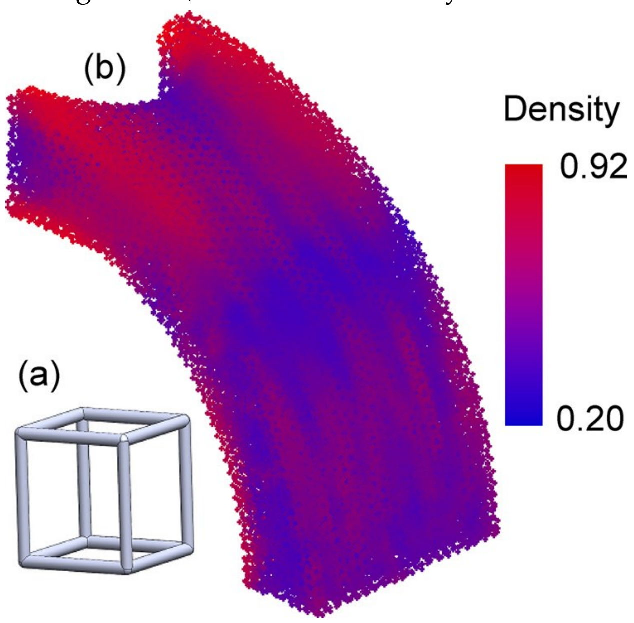

Figure 5.3 (a) Cubic unit cell. (b) Optimal density distribution.

The resulting lattice structure was based on the resulting local density, and accordingly to the available computing power of the workstation and the characteristics of the AM machine, for both the minimum dimensions and longest ligament length that could be built horizontally without extra support structure being required to mitigate thermal distortion. The lattice was then provided with an inner and outer layer of 1 mm of solid material, and reinforced around the bolt holes. The mass of the final design was 53% lower than that of the baseline fully-dense casing. The design process is illustrated in Figure 5.4.

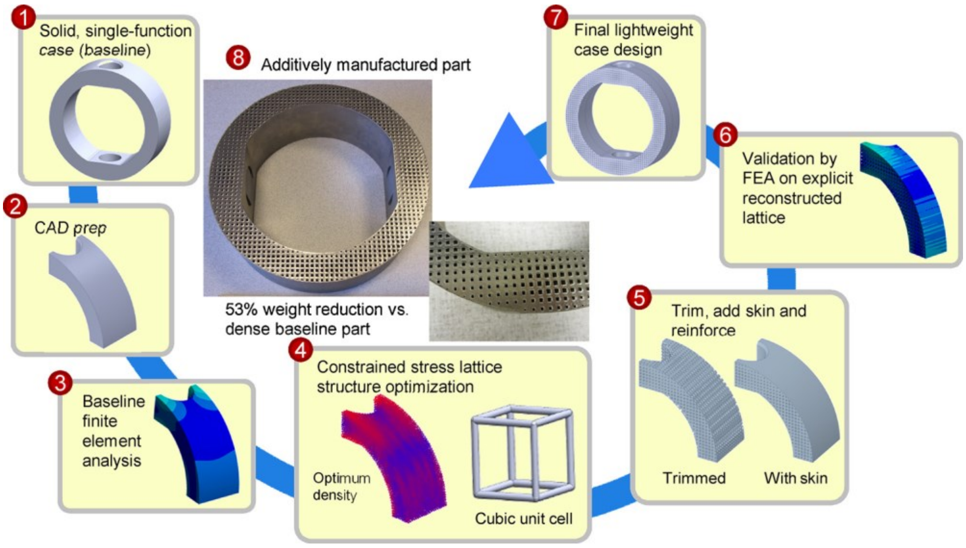

Figure 5.4 Design and manufacturing cycle of the specimens,

To understand the mechanical behavior at the unit-cell level a second FE analysis was implemented, with a high-fidelity model of the part with full resolution of the lattice, and the same loading and boundary conditions described for the baseline fully-dense model were used. The results are showed in Figure 5.5.

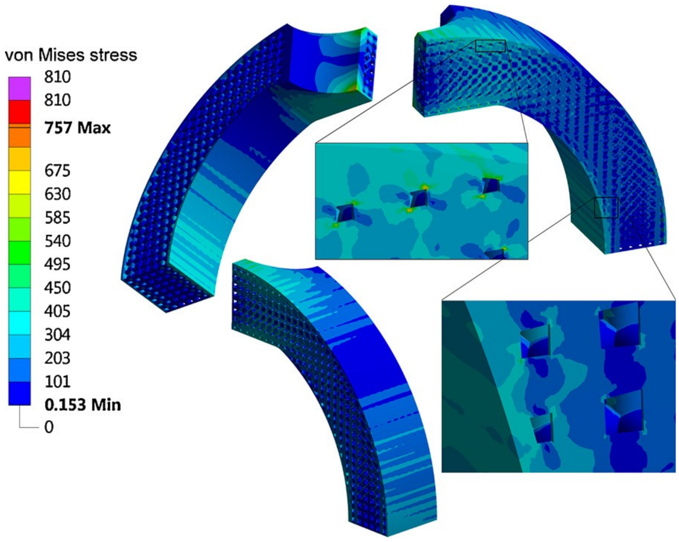

Figure 5.5 Von Mises stress in high fidelity symmetric FE model of casing at design load.

The results are similar in magnitude and location to the full-dense ones, with von Mises stress in all regions of the part lower than the upper limit of 810 MPa used in the optimization, because of the safety factor of 1.43 and the minimum density of 0.20 imposed in the optimization process. This results in a heavier final product but allow the skin to be supported without any additional structures, in addition the part is stronger overall.

Two copies were tested, to assess both the global and local behavior. The DIC images were acquired using a GOM Aramis 5M DIC system, placed immediately in front of the test article to capture the deformation of the front face. The two tests were performed to provide complementary information, the first with a field of view of 260x225 mm, covering the entire front face, the second with a smaller field of view of 35x30. The first was performed to measure the global strain information, with the open areas between the lattice structures filled with clay to apply an even speckle pattern. The second examined a smaller region on the right side of the front face, to provide more detailed sub-unit-cell strain information.

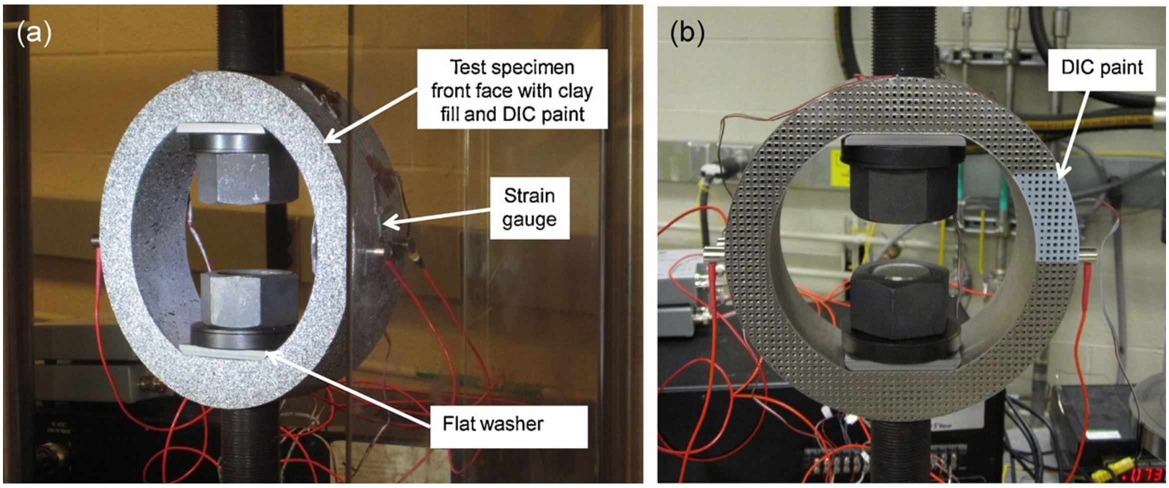

Figure 5.6 (a) Test article 1 with front face entirely painted for wide field of view in DIC measurement, (b) test article 2 with small painted region for narrow field of view in DIC measurement.

To provide a direct comparison to the high-fidelity FE model the distance between the two flat faces of the test article were measured using a virtual extensometer derived from the DIC data, adjusted for some minor initial out-of-plane rotation caused by the aligning of the test article with the load axis.

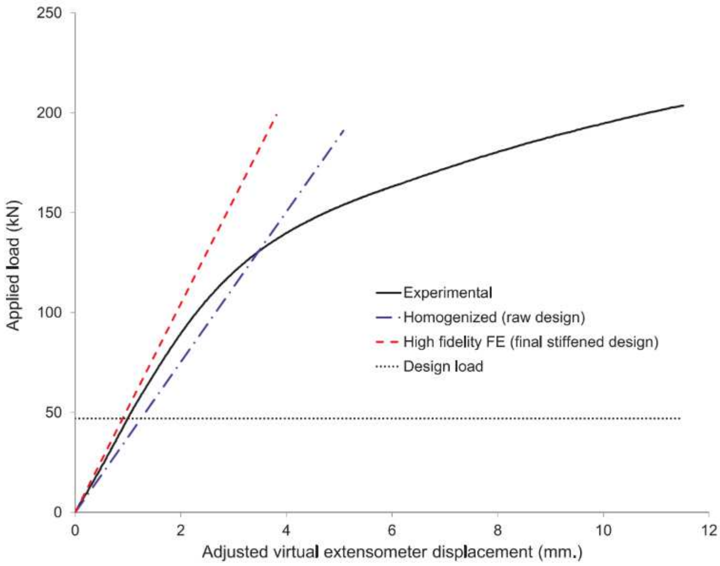

Figure 5.7 Observed load-displacement curve for test article 1

The results show a linear behavior well above the design load, as intended in the design process. The experimental data at low loads agrees with the high-fidelity FE prediction, with deviations only above the design load (horizontal dotted line). The difference in slope between the experimental and the homogenized model are probably due to the increase in overall stiffness of the reconstructed design when the skin and bolt-hole reinforcements were added. The data collected from the three strain gauges agrees with the high-fidelity model prediction, especially at the 45° and 90° positions.

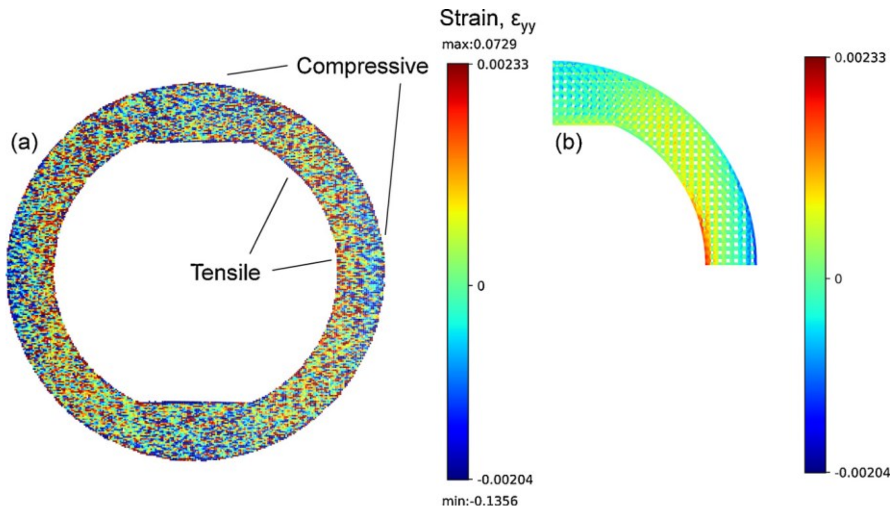

Figure 5.8 (a) Test article 1 experimental wide-area digital image correlation (DIC) measurement of y-direction strain, ε_{yy}, at the design load of 47 kN. (b) High-fidelity finite element model (symmetric quarter section) prediction of the same quantity.

In Figure 5.8 (a) are represented the wide-area DIC measurements of the y-direction strain (ε_{yy}), derived from the images acquired from the front flat face of the test subject 1.As visible a great amount of noise is lowering the image's quality. This noise was caused by the holes being close to the measurement resolution, the relatively small strains compared to the overall dimensions and the large field of view. Despite all of that bands of tensile and compressive regions are visible, and this behavior was corresponding to the-high-fidelity FE model, showed in Figure 5.8 (b).

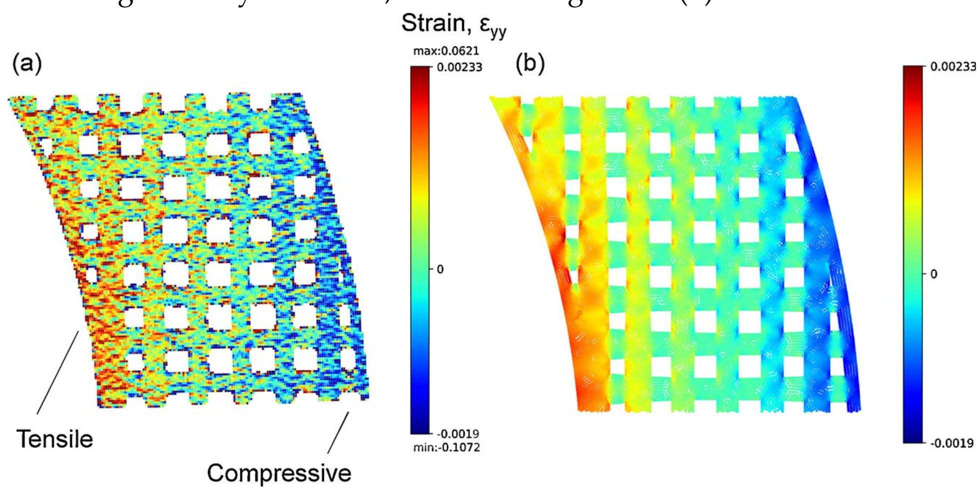

Figure 5.9 (a) Test article 2 experimental high-resolution digital image correlation (DIC) measurement of y-direction strain, ε_{yy}, at the design load of 47 kN. (b) High fidelity finite element model prediction of the same quantity.

A close view of the strain field of the test subject 2, represented in Figure 5.9, highlights the good correspondence between the FE model and the DIC measurements of ε_{yy} at the design load, using data derived from the experiment. Like in the wide-area results some noise is present in this close view too, but the data are overall better in quality, because of the reduced field of view compared to the lattice unit cell size. The different areas of tension and compression stresses during the test are visible on the inner and outer layer of the casing, as predicted in the high-fidelity FE model in the same locations.

The DIC was also used to collect data from the test on article 1 using wide-view at different loadings until failure, in this case at the design load of 47 kN, an intermediate load of 84 kN and the load step just prior to failure, 203 kN. As loading increases the tension and compression behavior of the inner and outer regions increase in magnitude, as visible in Figure 5.10

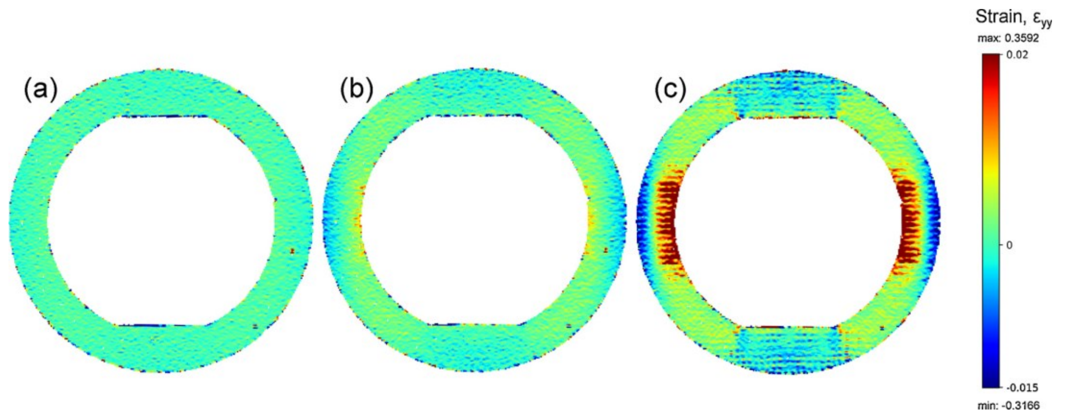

Figure 5.10 Test article 1 experimental wide-area digital image correlation (DIC) measurement of y-direction strain, ε_{yy}, at three different loadings: (a) 47 kN, (b) 84 kN, and (c) 203 kN.

More interesting results were obtained repeating the same procedure using the close-view DIC setup on the test subject 2. Figure 5.11 shows where the strains are concentrated. High tensile strains develop in ligaments near the inner diameter and are especially present in the corners of unit cells near ligament junctions in the 210 kN loading case just prior to failure. Both the test articles failed due to a crack originating at the ligament junction with the inner diameter skin and then propagating in the direction of the outer layer by jumping to adjacent vertically aligned high-stress ligaments junctions.

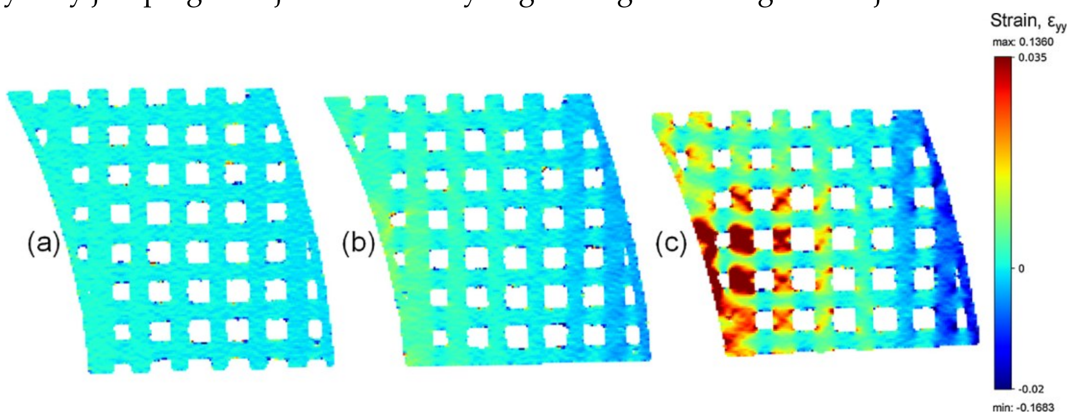

Figure 5.11 Test article 2 experimental high-resolution digital image correlation (DIC) measurement of y-direction strain, ε_{yy}, at three different loadings: (a) 47 kN, (b) 133 kN, and (c) 210 kN.

Figure 5.12 allow a comparison between the results obtained through the DIC analysis at the load step prior to failure and the predicted behavior at design load. The location in which the crack occurs is the one with the highest tensile stress in the FE model, and coincides with one of the highest areas of experimentally observed tensile strain.

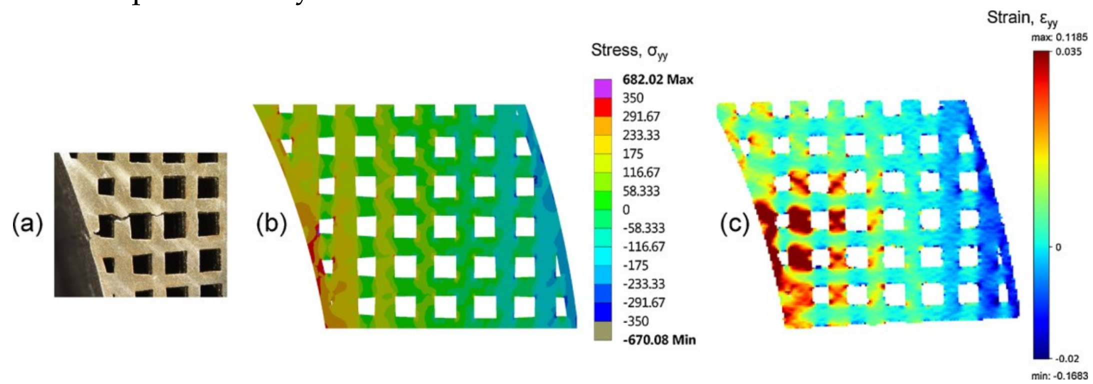

Figure 5.12 (a) Picture of failed portion of test article 2 (mirrored about x and y). (b) High-fidelity FE model prediction of stress (σyy) at design load (47 kN) in region of failure. (c) Test article 2 experimental high-resolution digital image correlation (DIC) measurement of y-direction strain, εyy, at load step just prior to failure (210 kN)

Ultimately the DIC analysis provided reliable numerical full field results, agreeing with both the high-fidelity FE model and the experimental data like gross displacement and strain gauge measurement.

5.2 Strain concentrations in microlattices

The behavior of microlattices under compressive load was investigated in [46]. While the design processes and FEM analysis are usually performed on the ideal meta-material, the geometry obtained by the AM process profoundly differs from the ideal one, with local geometrical irregularities producing local stress and strain localizations not present in the idealized structures.

A combination of digital image correlation and 3D tomography was used to assess the behavior of the real geometry.

The micro-lattice structure of the compressive sample is composed of BCC unit cells and it is manufactured with SLM of a pre-alloyed AlSi10Mg powder with average powder size of 30 μm.

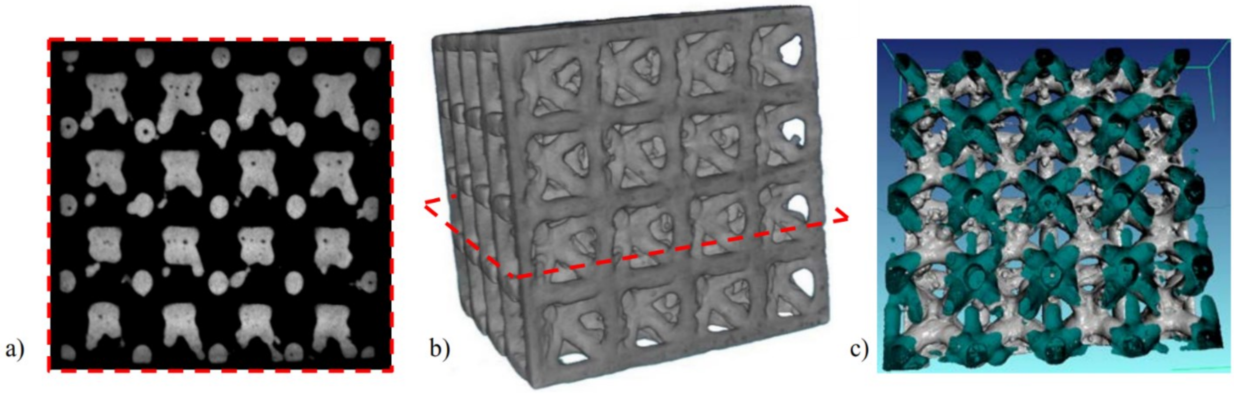

Figure 5.13 (a) Section of the printed sample (micro tomography image); (b) Real geometry of the specimen (micro tomography reconstruction) (c) external surface and pores of the specimen (micro tomography surface).

After the SLM process 3D tomography was used to obtain the real geometry of the "printed" sample.

Ideally all struts have a circular section, in the sample the cross section of the struts was found to be different, not only in circularity but in thickness to, with changes along the strut axis and generally bigger than the idealized. The external surface of this strut is irregular and multiple defects can be detected in the structure.

In order to measure continuously the displacement during the test, a deflectometer was used according the schematic proposed in Figure 5.14 (b).

A compression test was performed using an MTS Alliance RF/150 testing machine in displacement control at a rate of 0.1mm/min. Local and average strains in the sample were mapped and measured during the sample deformation.

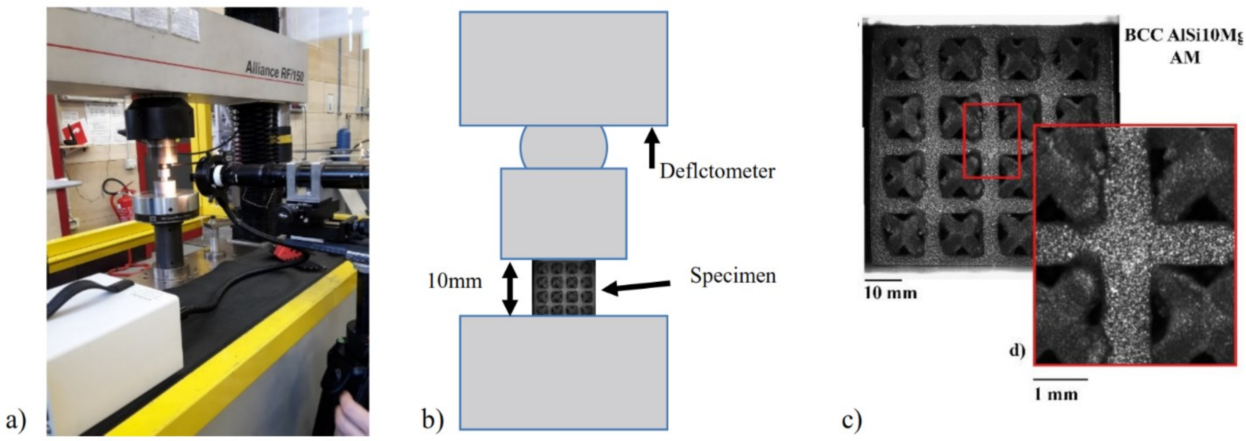

Figure 5.14 (a) Test machine and DIC camera; (b) Scheme of the experimental test; (c) Speckle pattern.

The test subject needed preparations to undergo DIC process. The speckle pattern must be plane and regular, so a flat surface must be created on the sample. The printing process of the sample create points with indentations or protrusions, so some of the struts material on the surface was removed by means of a polishing with abrasive papers. As a result, in the plane visible to the DIC camera the local buckling load was further decreased. This effect was however considered in the digital sample used for the FE simulations, as the 3D tomography of the specimen was performed after preparation, allowing a proper comparison between the simulation and the real test.

The speckle pattern was created in the front face of the specimen using a nitro black paint sprayed with an aerograph.

To map the entire sample surface and increase the strain resolution multiple images of the target specimen's surface were captured during the test. More specifically the surface of the sample was virtually divided in six parts and, in every load step, six images were manually captured at a resolution of approximately 2.34µm/px. The resulting images were stitched and correlated by a commercial software.

The nine load steps were performed interrupting the compressive test at 0 kN (before starting the test), 2kN, 4kN, 5kN, 6kN, 7kN, 8.8kN, 0 kN (after the final unload). The stress-strain curve was determined using the average strain measured on the DIC surface (orange line) and the displacements from the deflectometer (blue line). The curves are visible in Figure 5.15.

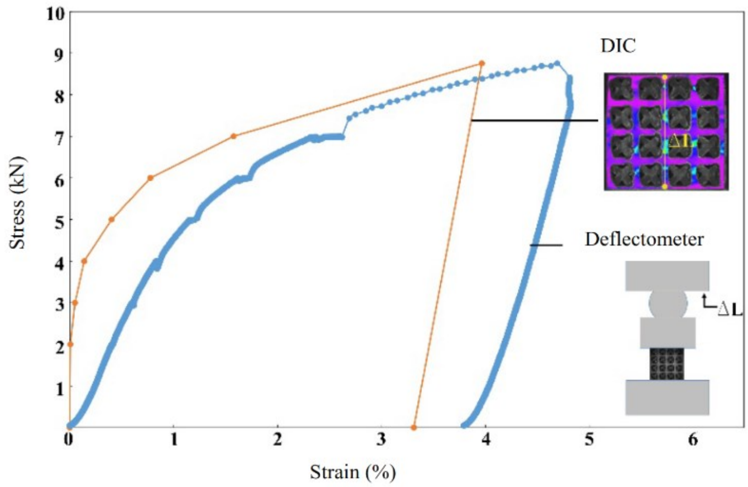

Figure 5.15 Resulting stress- strain curves

As visible in Figure 5.14 the deflectometer is not applied directly on the specimen but on the upper plate, and this creates the differences between the two curves visible in Figure 5.15.

The DIC analysis of the struts allow to identify three different families of defects, as visible in Figure 5.16, all leading to different strain concentrations in the microstructure.

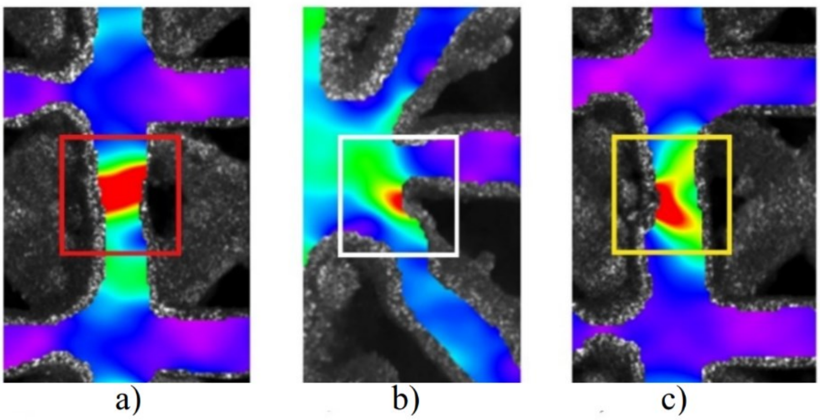

Figure 5.16 (a) Buckling defect; (b) geometrical defect; (c) printing defect

An estimation of the strain concentrations factor K_ε was then performed, as a ratio between the maximum axial strain adjacent to the defect and the average strain measured in the strut that contains the defect:

$$K_\varepsilon = \frac{\varepsilon_{local}}{\varepsilon_{strut}}$$

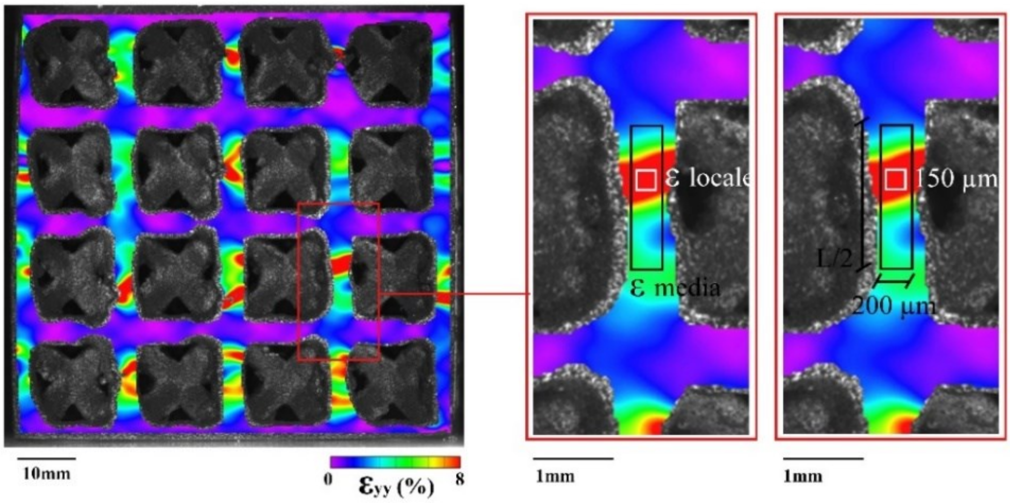

Figure 5.17 Local and average strains measurement.

The results from the experimental test and the DIC were compared with FE analyses. Two different models were used. One made of the ideal geometry of the sample, with regular struts, the other one of the real structures, acquired using micro-tomography. In the ideal geometry low strain localizations were detected, while in the acquired one multiple strain concentrations were observed, in locations qualitatively similar to the strain concentrations measured with the DIC.

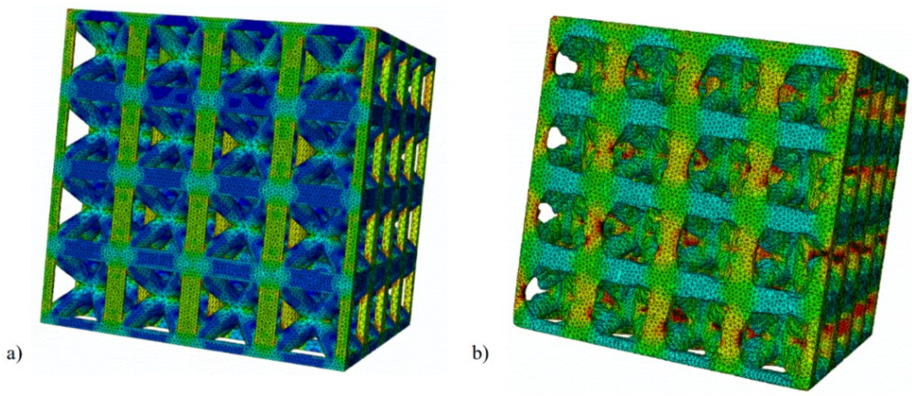

Figure 5.18 FE model with ideal geometry; (b) FE model with real geometry

DIC was used to evaluate the K_ε factor in every vertical strut. The results are illustrated in Figure 5.19 (first and second column from the left), with the K_ε values divided in two different groups based on the type of the defects that generate the strain concentration. A K_ε of 1.48 was measured for the strain localizations arising from the buckling defects, while for the printing defects 1.52, with a maximum factor of 1.91 for the printing defects and the 2.02 for bucking defects.

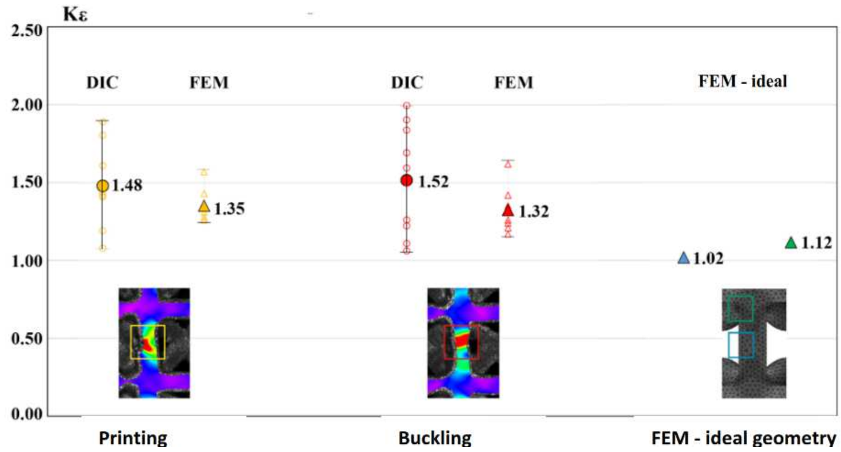

Figure 5.19 Strain concentration factor plot for the bcc micro-lattice geometry analyzed in this study.

In this work only strain localizations on the external surface were considered, having compared DIC and FE results. In the idealized geometry the K_ε was measured on the surface too. Unlike the acquired model in the ideal one there are no strain localizations in the vertical struts, so local strain and K_ε was measured in two positions, one considering local strain in a square area in the middle of the vertical struts on the external surface, the other on a square area at the intersection between vertical and horizontal struts, where the model has strain concentrations. The results are summarized in Figure 5.19 (right column)

From the results of the paper we obtained that, even if the FE model based on the real geometry was able to represent the mechanical behavior of the sample, there were differences between experimental and numerical results, with the numerical results being lower in amplitude. Strain localization occurs at the same regions where strain concentrations were observed in the experiments, so the overall behavior is the same, but the FE model carry some limitations. The FE analysis on the real structure does not model the plastic behavior of the material. This is particularly important in lattice components, since in the real structure local plastic strains arise even in the nominally elastic region of the stress-strain curve. Furthermore, it was not possible to run a convergence analysis or to adopt a mesh with quadratic elements, due to the computational burden of the geometrical reconstruction. So, the DIC analysis, where applicable, has been proven more reliable than the FEM simulation.

5.3 Strain maps and measurement of deformation heterogeneities

In [47] DIC was used to investigate at a fine scale the mechanical behavior of porous lattice materials for potential orthopaedic applications. The purpose of the paper is to illustrate how DIC can be put into practice in order to assess reliable, time-resolved evaluation of the strain heterogeneities at the surface of lattice materials.

Various specimens composed of three different mesostructures where tested in quasi-static compression up to failure.

In bioengineering lattice materials are useful because they can achieve specific stiffness to weight ratios, which in prosthetic design is used to promote long term stability of implants, achieved by having mechanical properties of the implants compatible with those of the bones. AM allow the mesostructure to be adjustable on demand, making possible to tailor the structural and functional characteristics of the produced part.

The purpose of the analyzed work is to show how Digital Image Correlation can be used to achieve quantitative assessment of various lattice geometries at the mesoscale level, to better understand the mechanisms that govern them.

The mesostructures investigated in the paper were: cubic, body-centered cubic reinforced by a central strut (also referred to as BCCZ) and diamond. The test pieces were fabricated in TA6V-ELI (a titanium alloy) using an EOS M280 Direct Metal Laser sintering system. Since those can have great influence on the mechanical properties of the specimen, to obtain comparable results the fabrication conditions, such as the energy deposition and the hatching configuration were kept constant.

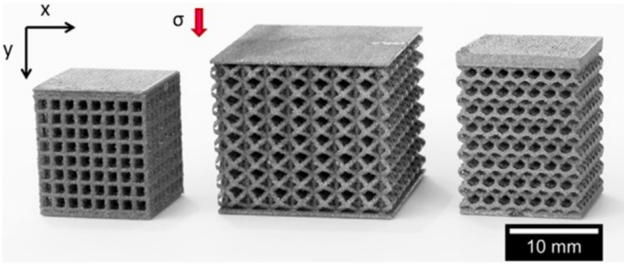

Figure 5.20 The three mesostructures: cubic, BCCZ and diamond (left to right)

Each specimen was designed to have a density of 75% with specified strut thickness of 500 μm, with the addition of 2 mm thick upper and lower plates perpendicular to the compression direction.

Two sets of tests were performed, one interrupted past the macroscopic elastic limit σ_{02}, the other continued until collapse of the structure. The tests were uniaxial quasi-static compression at strain rate 10^{-3} s^{-1}, with the specimen compressed with the loading direction perpendicular to the compression plate.

The force and displacement were recorded by the testing machine, an MTS Alliance RF/200, while the DIC measurement were carried out with a Manta G504-B monochrome camera. The camera was mounted on a carbon fiber tripod with a high precision head and a x-y micrometric stage.

The images had dimensions 2452x2056 pixels, resulting in 5-7 μm numerical resolution, depending on the specimen size. Giving the natural roughness of the specimen surface the speckle pattern was obtained applying a spray projection of mate white boron nitride, which enhanced the surface texture.

As discussed in Chapter 4 there are measure to take to reduce the errors of DIC results. The tests illustrated in the paper appear to consider those suggestions, using a telecentric lens, middle-position optical aperture and lighting of the specimen with a color that allow to exploit the optimal quantum efficiency of the camera sensor. In addition, the exposure time was adjusted to allow no more than 0.1% of saturated pixels in the images and a large distribution of gray levels. In Figure 5.21 is illustrated how the grey level histograms associated with the picture of the specimen change as the exposure time increases.

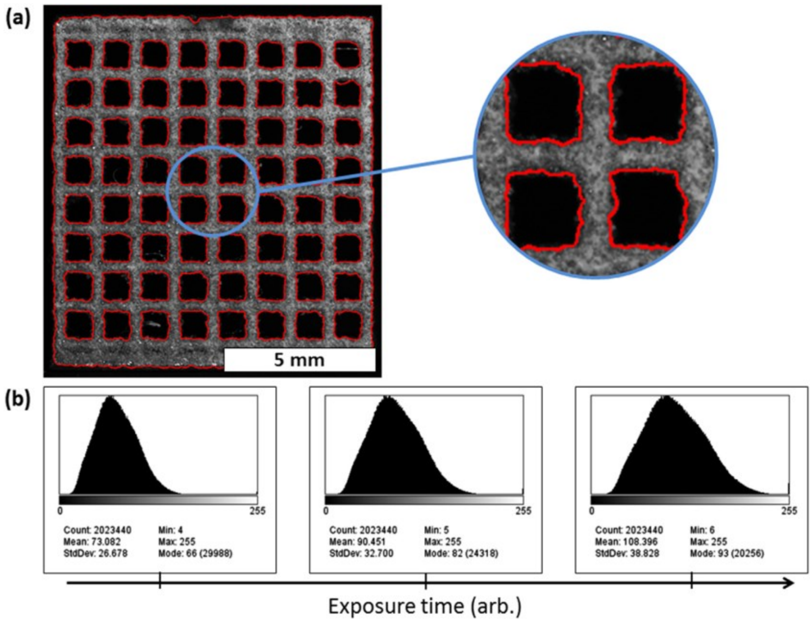

Figure 5.21 (a): Typical image of a cubic mesostructure specimen in the initial state with close-up view of the texture. The contour lines delineate the area processed by DIC. (b): Histograms showing the widening of the gray level distribution with exposure time.

It is noticeable the increase in saturated pixels (level 255) and the widening in the distribution. The behavior of both grey levels and percentage of saturated pixels are illustrated in Figure 5.22, showing that both increase linearly against exposure time.

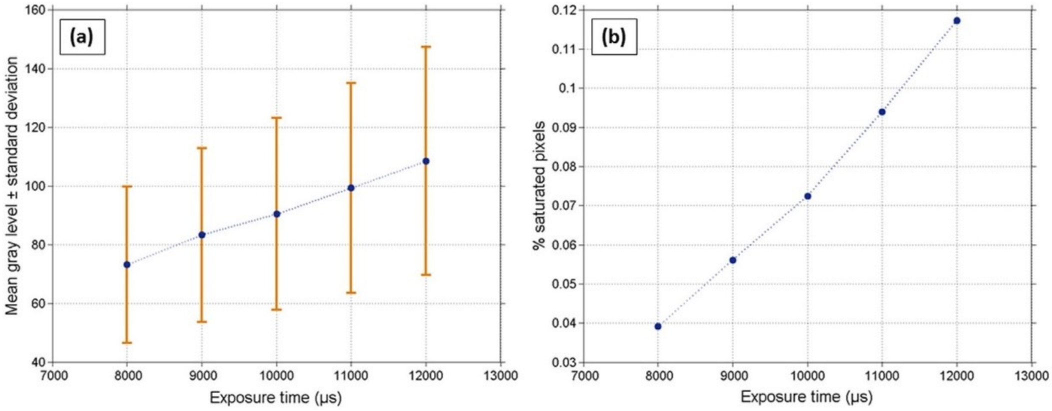

Figure 5.22 Influence of the exposure time on the image properties (specimen in Figure 5.21). (a): Average and standard deviation of gray levels vs exposure time, (b): Percentage of saturated pixels vs exposure time.

The analysis was performed using OpenDIC [48], which calculates the planar displacement fields between the initial image of the specimen and each image obtained at increasing compression steps.

Via OpenDIC the mesostructure of the specimen was selected as the zone of measurement, along with a subset size of 17 pixels, resulting in length of 75 to 100 µm with at least three gray level peaks. The measurement points were distributed as a square grid with a spacing of 7 pixels, or 35-50 µm. Being generally recommended, overlapping was allowed between neighboring subsets. These parameters resulted in a strain field of 275 x 250 pixel and 69000 measurement points. To quantify the quality of the measurements the zero normalized cross correlation value, ranging from -1 to 1, was used as parameter. This value indicates how two subsets, in the reference and deformed states, are similar. In the analyzed paper the threshold was set at 0.75, with values below considered unreliable and the corresponding displacement values replaced, using the average values of the nearest neighbors with ZNCC above 0.75.

These now corrected displacement fields were then smoothed spatially and temporally to reduce noise and numerical artifacts. A finite elements bilinear quadrilateral Q4 elements algorithm was then used to compute an analysis on the strain fields, with the help of the image analysis program Fiji [49]. The right exposure times and lighting conditions were established and then used execute the procedure to quantify the uncertainties.

Evaluation of the uncertainties due to the setup

To evaluate precision, or repeatability, and accuracy of the method the response of the system to specified inputs was measured. This is needed to evaluate the performance of the imaging acquisition chain.

The procedure, with the schematic illustrated in Figure 5.23, was the following: A specimen with cubic mesostructure was set in focus at a reference position and was translated laterally and axially by increments of 10 µm and 500 µm (± 2 µm), respectively. No actual deformation was imposed to the specimen, so the target strain values is zero, and every change in the results are then due to the errors related to the movements. Three parameters were evaluated: influence of loss of focus, accuracy and precision and the precision of the method. The influence of loss of focus was evaluated by measuring the strain fields between the reference and the axially translated images, the accuracy and precision by measuring the displacement and strain fields between the reference and lateral positions and the precision of the method by measuring the strain field between ten images taken at the reference position.

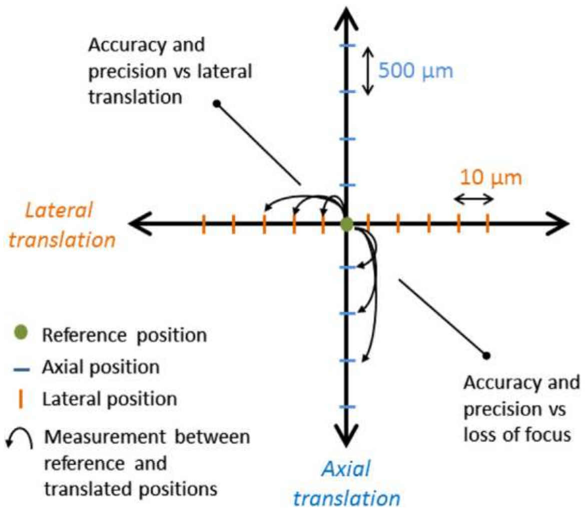

Figure 5.23 Validation of the DIC method by measuring displacement and strain field between a reference image and images of the same translated scene.

Being directly related to the reliability of the DIC method the results of these procedures are illustrated in the following paragraphs.

Precision at the reference point

This test allows to evaluate the errors due to noises in the acquired images. To do that nine strain measurements were performed while leaving the specimen at the reference position. This basically compare the results from different images of the same non-stressed conditions. Ideally the results should coincide with each other. In reality the results slightly differ because of the noise introduced by the acquiring device, with average values comprised between ± $5{\cdot}10^{-5}$. In [29] are specified as commonly accepted for DIC uncertainty above $1{\cdot}10^{-4}$, which means the noises of the setup are acceptable. The resulting standard deviation, of the order of $1{\cdot}10^{-3}$, means that the strain values exhibit moderate noise. These results, both average and standard deviation, are represented in Figure 5.24.

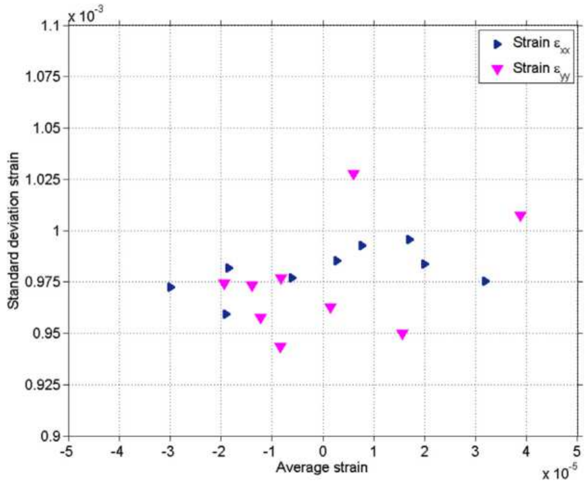

Figure 5.24 Average and standard deviations of strain maps ε_{xx} and ε_{yy} measured over ten images of the same specimen at the reference position.

Accuracy and precision vs lateral translation

To evaluate the influence of lateral translations 10 images were taken for each translated position, then the displacement fields between these and the reference in-focus image were calculated and averaged. The results were encouraging, showing good correspondence between the imposed and measured displacement values and moderate scattering, far lower than the estimated uncertainty over the imposed translation (2 μm, as mentioned before). Using the displacement fields the average strains were derived, obtaining an average bias for each measurement inferior of $1{\cdot}10^{-4}$ and the scattering of the same order of magnitude than the one associated with the acquisition noise, placed between $1{\cdot}10^{-3}$ and $2{\cdot}10^{-3}$.

These results are graphically illustrated in Figure 5.25 for better understanding.

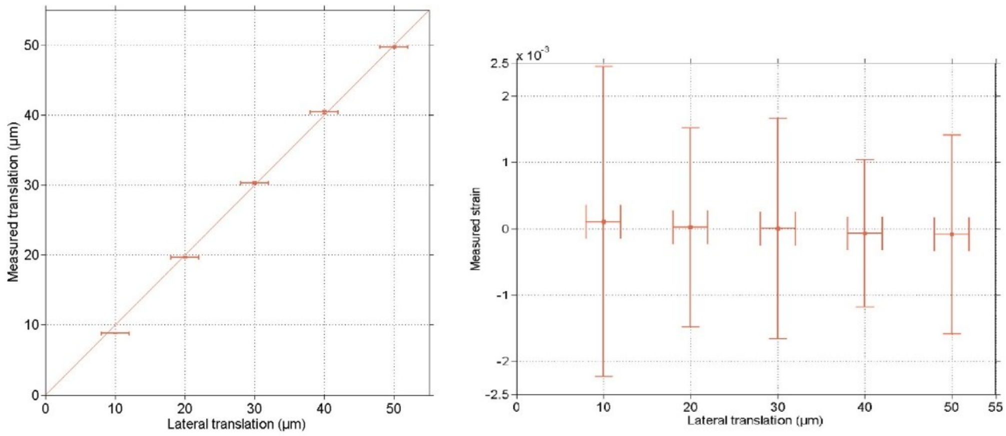

Figure 5.25 (Left) Measured displacement vs imposed lateral translation, with in horizontal the 2 μm physical uncertainty over translation. The first bisector is plotted for comparison. (Right) Variation of the measured strain versus the imposed lateral translation.

Accuracy and precision vs loss of focus

The evidence of loss of focus during the tests was evaluated taking images of the specimen at different distances from the camera without adapting the focus, for a total of 17 positions separated by 500 μm, with ten images recorded for position. The quality of focus was evaluated by the normalized variance of the intensity levels for each image, with the maximum of the curve corresponding to the position with the best focus (the in focus position), as shown in Figure 5.26.

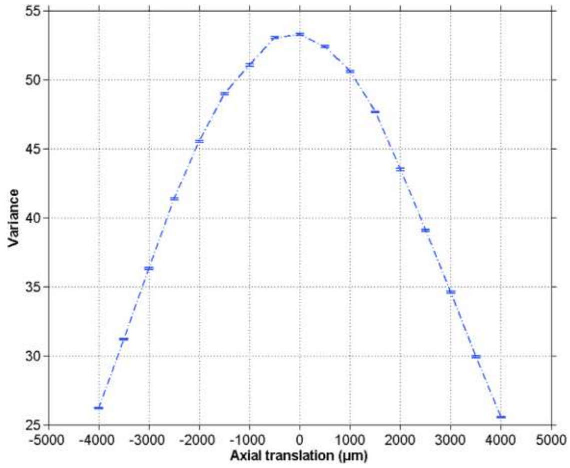

Figure 5.26 Variance of the gray levels in the images versus axial translation. The absolute values are characteristics of the imaging conditions used in [47].

After calculation of the strain fields between the focus position and the images for each translated position was observed that the apparent strain values are in compression when the sample is too far and in tension when too close. These results are due to an optical effect, since specimens appears larger at close distance and smaller at far distance relative to the focus point. Even if the scattering of the values increases with the loss of focus, they remain moderate even for large axial displacement (the test went up to 2 mm). For the specimens tested in the paper, due to the lattice dimensions, the out-of-plane displacements cannot exceed 500 μm, even at failure, so the strain uncertainty associated with these displacements will be of the order of $1 \cdot 10^{-3}$.

Compression tests on the three mesostructures

During the compression tests of the specimens both the stress-strain curves and the strain maps were analyzed. In addition, the use of DIC allowed an advanced analysis, performed on the cubic mesostructure.

In Figure 5.27 is represented the raw macroscopic compressive stress-strain curves for every specimen. While every mesostructure shows different behavior, as denoted by the curves being superimposed, the test has high reproducibility, with failure patterns varying according to the mesostructured, with the cubic specimens failing on an entire row perpendicular to the loading direction, the BCCZ concentrate deformation on diagonal bands and diamond specimens fail with a diffuse crushing pattern.

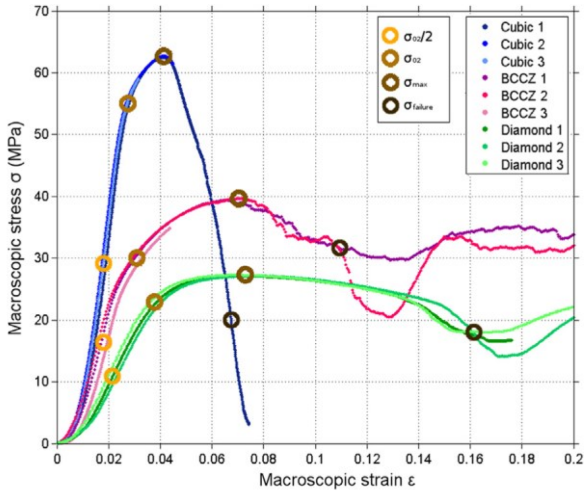

Figure 5.27 Raw compressive stress-strain curves for the cubic, BCCZ and diamond specimens. The circles correspond to the approximate values of stresses at which the images used to compute the strain maps in Figure 5.29 were taken.

In Figure 5.27 should be noted that all the curves presents a concave part at the beginning of the test, due to the data being derived from the machine sensor and not from an extensometer placed on the specimen. The curves then comprise the initial adjustment of the specimen to the compressive anvils and the deformation of the machine itself in addition of the deformation of the specimen.

The actual deformation of the specimens can be directly obtained from the DIC data, with the correction acting like an optical extensometer measuring the translation of two reference points separated by a known distance.

The procedure to obtain the engineering strain of the sample alone $\Delta L/L_0$, illustrated in Figure 5.28, is the following: the average vertical displacements of two linear zones located at the top and bottom of the sample are calculated over time, then subtracted and divided by their initial distance. In Figure 5.28(d) is clearly showed how the concavity at the beginning of the curve is corrected, resulting in a much higher apparent Young's modulus for the specimen.

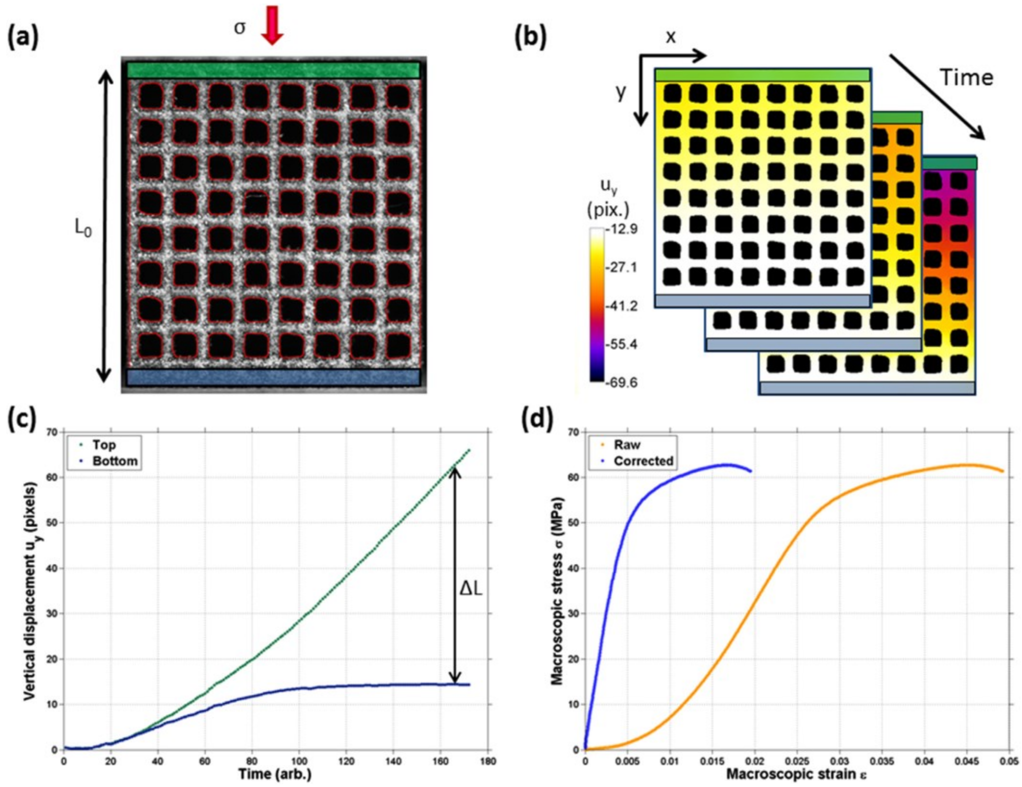

Figure 5.28 Correction of the raw stress-strain curves. (a): Position of the measurement zones at the top and bottom of the sample, (b): Vertical displacement fields at increasing times, (c): Vertical displacement values measured at the top and bottom zones, (d): Correction of the raw stress-strain curve for cubic specimen number 3.

As extensively mentioned before, being a full-field optical method DIC allow to obtain the strain map of the specimen. Using these is possible to analyze the strain heterogeneities inside the specimen itself (or at least on its surface, for 2-D DIC). In Figure 5.29 are showed the strain maps of one specimen for geometry, with the strain component parallel to the vertical loading direction (ε_{yy}) used to map the strain heterogeneities. The resulting maps are between 300 and 350 pixels in width and height, with values of ε_{yy} comprised between 0 and -0.15 (dark shades corresponding to higher compressive strains). The calibration is the same of all the specimens.

The results are realistic shape of strain localization at failure, matching the sample final configuration. The exact strain values within the failure pattern cannot be considered completely accurate, since considerable deformation and possibly loss of continuity of the material have occurred.

Another notable result is the evidence of drastically different behavior of each mesostructures, with every one accumulating strain differently. In the cubic sample the struts aligned with the compression direction sustain most of the strain, with the strain not evenly distributed among them, and a clearly defined area of collapse is visible.

BCCZ specimen has big heterogeneities in the strain behavior at failure, with the vertical struts of the main diagonals undergoing most of the deformation. While in the macroscopic elastic region the strain is more homogeneously distributed than the cubic specimen. The vertical struts located in the other diagonal underwent more strain than the rest of the struts, annunciating a second symmetrical failure event. This observation would not be so easy to make without DIC.

The diamond specimen exhibits diffuse strain localization throughout the entire deformation process, mostly localized at the nodes between the inclined struts, with more or less the same strain levels measured in all the struts where the strain localized. The diffuse pattern is present even at failure, as damage can be found all over the surface.

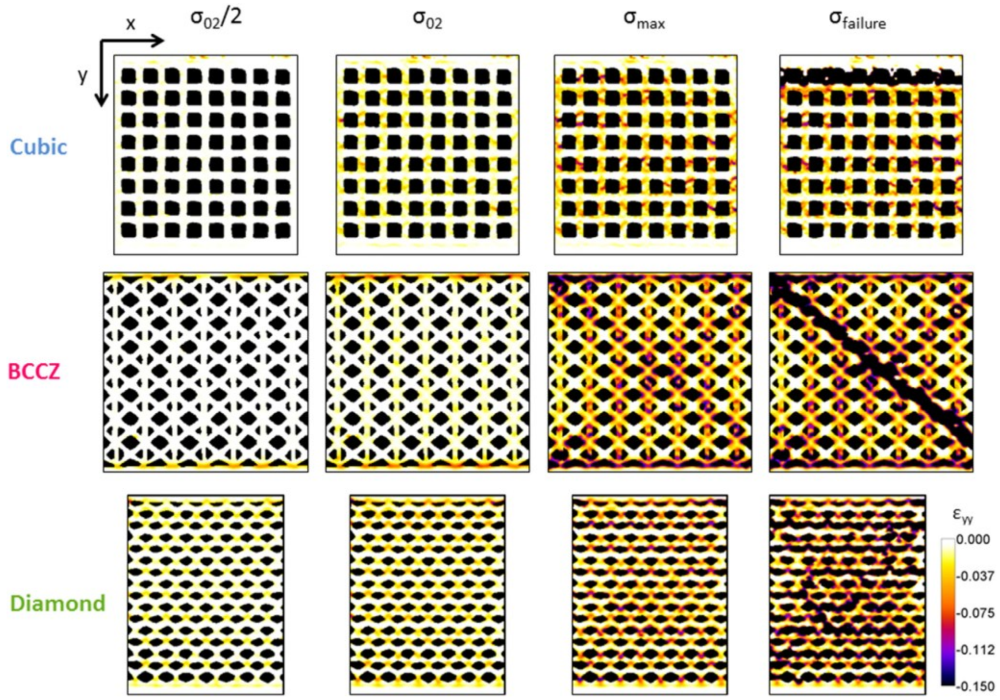

Figure 5.29 Strain maps at increasing macroscopic stress levels for 3 geometries. Strain component εyy aligned with the vertical load, same scale for all maps.

The strain variability over the specimen can be quantified by the standard deviation of the field during the compression test. This is made possible by DIC, having a set of images taken during the experiment at different level of deformation. The standard deviation can be calculated by measuring the intensity histogram of the images, having that heterogeneously deforming specimens should display high standard deviations, while homogeneously deforming specimens should show low values. This analysis provides general data regarding the entire surface, resulting in an evaluation on how scattered the strain values are. In Figure 5.30 is illustrated the standard deviation of ε_{yy} for every image taken during the test, resulting in curves of standard deviation vs macroscopic strain. The standard deviations are relatively large and they steadily increase as the sample undergoes larger global deformations, with the same behavior for specimen of the same family, and some consistency for the diamond structure. The cubic specimens show high standard deviations, even greater than the macroscopic strain. This behavior is understandable, looking at the strain fields shown in Figure 5.29, with the cubic specimen having sharp localization on a few struts with high values, resulting in the high scattering of the strain values considered all together.

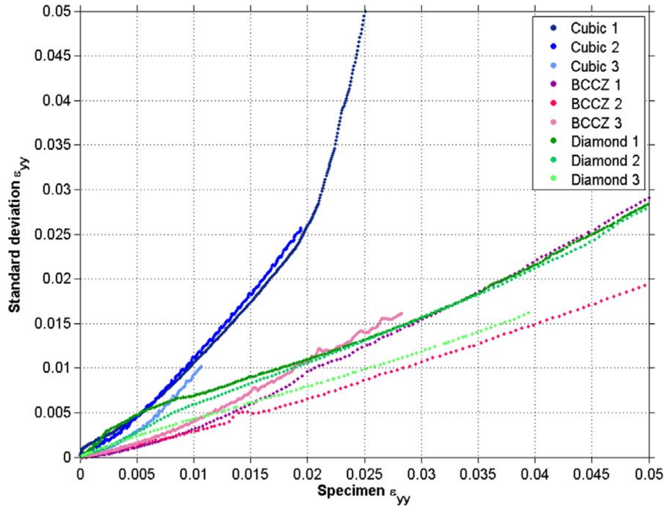

Figure 5.30 Standard deviation of the strain field values vs macroscopic strain

The strain maps allow to analyze the post failure behavior of the non-critical zones of the specimens, shown in Figure 5.31, displaying information on the locations of the structures remained less deformed. The ability to investigate the behavior of these areas after the specimen failed provide the opportunity to assess the remaining integrity of the specimen itself. This analysis is conducted measuring the evolution of the average local strain with applied stress in regions that do not fracture.

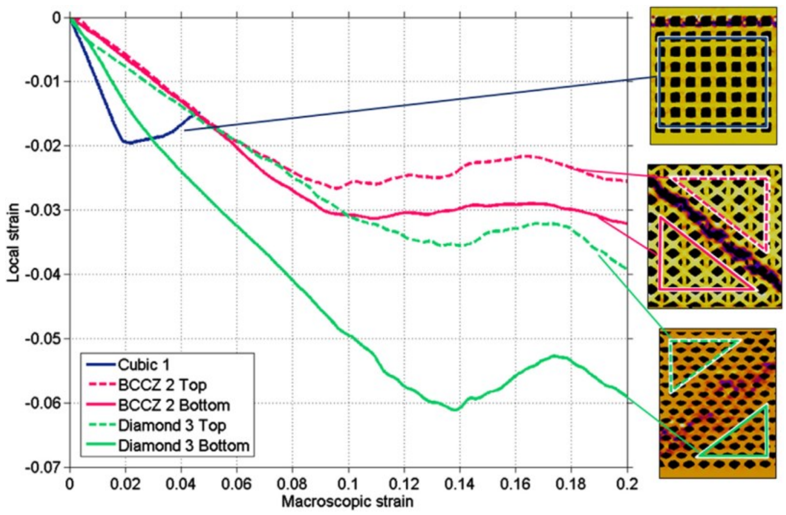

Figure 5.31 Strain evolution in non-critical zones for cubic specimens.

The increase of the curves for the cubic and BCCZ mesostructures means that elastic energy is released as the critical part concentrates strain and continues to accommodate the applied deformation.

Advanced DIC analysis on the cubic mesostructure

As shown before the cubic mesostructure specimen has exhibit a failure behavior of particular interests, giving the collapse of the upper row of struts, below the contact plate. The paper evaluates up to what extent the DIC technique can provide spatially resolved results to investigate said behavior. In Figure 5.32 is plotted the strain profile along a vertical row of the specimen's struts, showing that most of the strain is supported by the vertical struts. Strain concentrations are also clearly visible.

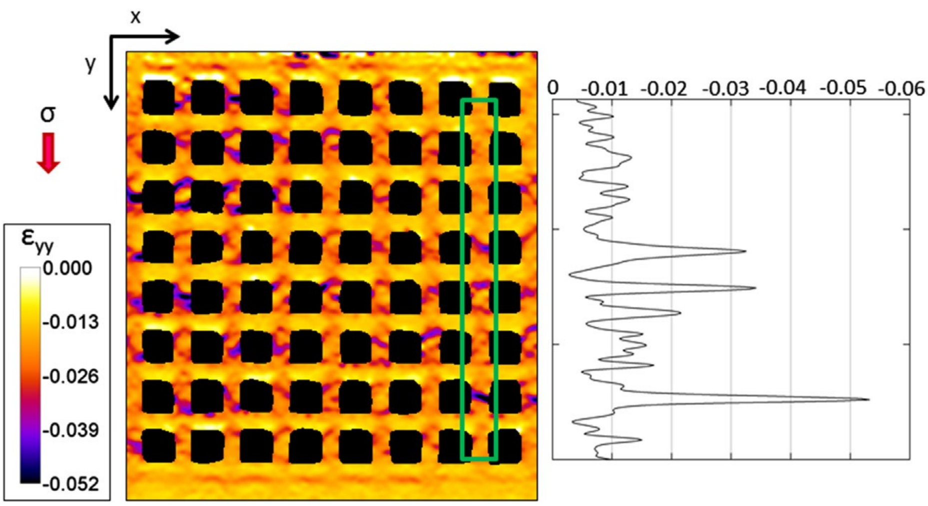

Figure 5.32 Profile plot on a row parallel to the vertical compression direction at macroscopic strain 0.85%

The strain maps allow also to isolate and select specific areas of the maps to investigate their behavior. In Figure 5.33 the behavior of the vertical struts was investigated, plotting the mean strain values of each row perpendicular to the compression direction against the macroscopic strain of the sample. The absolute strain values of the critical row are not necessarily reliable due to the nucleation of discontinuities and out-of-plane displacement, but is made clearly visible that behaviors of the bottom and top rows are significantly different from the intermediate rows.

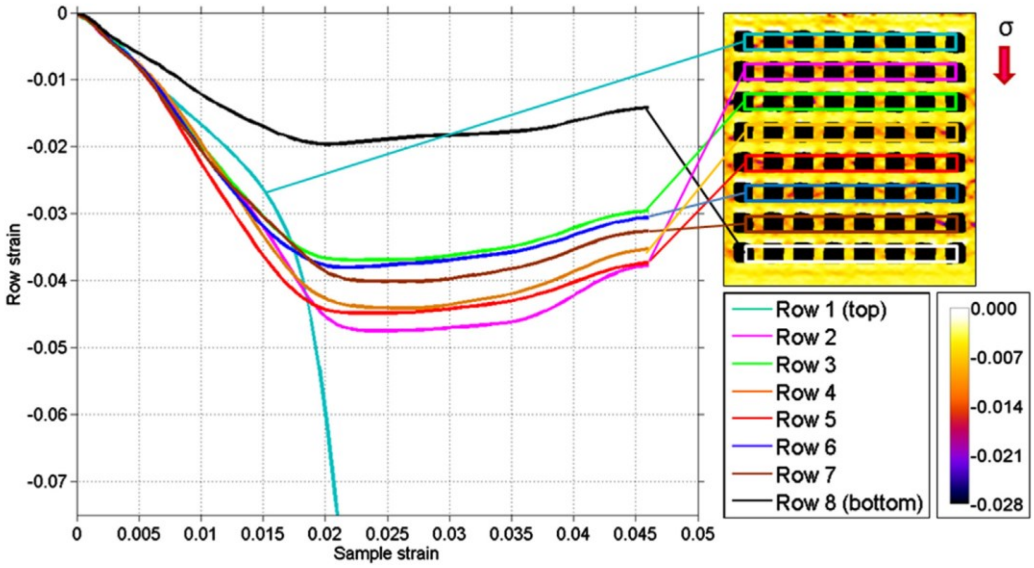

Figure 5.33 Average strain of the rows perpendicular to the loading direction vs macroscopic strain. Strain map on the right displayed as an example (strain 0.01).

Even the behavior of each individual strut can be investigated. The 56 vertical struts (excluding the struts on the edges) belonging on the face under observation were extracted from the image and the average strain for each strut was plotted against the macroscopic sample strain, as showed in Figure 5.34. The image show that the strain values of the struts differ greatly, even in a single row, while all the struts forming the critical row follow a similar evolution.

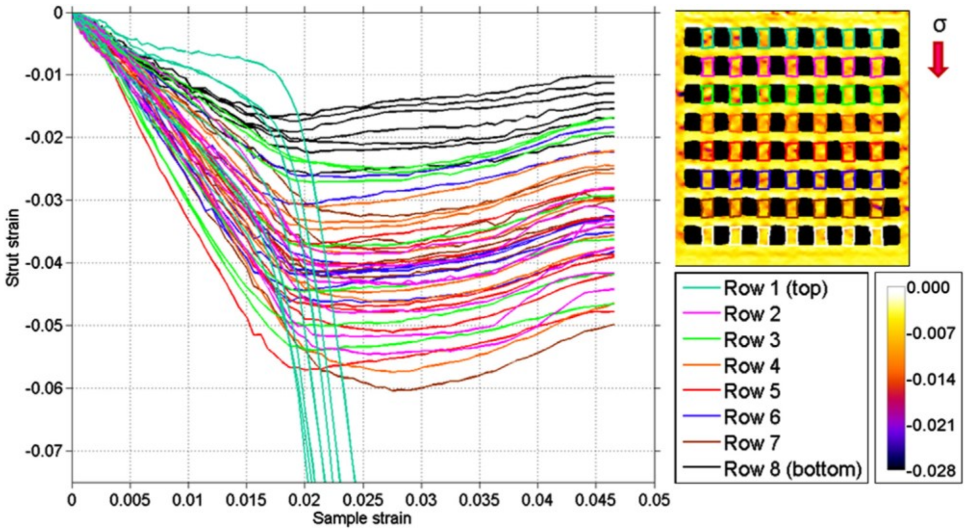

Figure 5.34 Analysis of 56 struts parallel to the compression direction. Colors correspond to rows. Strain map on the right displayed as an example (strain 0.01).

The DIC and test setup used for the tests lead to resulting strain measurements accurate and reproducible with respect of noise, in-plane and out-of-plane displacement, as shown by the evaluation of the uncertainties previously carried out. This should not be taken for granted, and every setup should be evaluated, with an uncertainty assessment procedure carried out for each new setup and specimen type. This is especially true for structures with long struts length, which can present significant out-of-plane displacements at failure. This family of specimens can benefit from the use of 3-D DIC setup. Once taken in consideration this peculiarity, it should be noted that the ability to perform analysis of the strain maps provide a great amount of data on the mechanical behavior of the mesostructures, even with 2-D DIC, which only covers the front face of the specimen.

In addition, the strain heterogeneities can be quantified both spatially and temporally, allowing the study of the evolution of the strains. These are mainly resulting from the geometry of the mesostructures of the specimens, which lead to specific deformation patterns, much more than from the defects caused by the AM process, which play a role at a fine scale. This is particularly visible with the cubic specimen, in which theoretically identical struts have behaviors completely different.

Furthermore, DIC allows to perform time-resolved analysis of the strain maps, which showed that strain localizations occurred very early in the process of compression, some as early as half of the macroscopic elastic limit of the structure, which imply that the absence of damaging in the specimen cannot be assessed by visual observation.

Giving the three-dimensional arrangement of the lattice structures some behaviors of difficult explanation observed from the struts of the specimen's surface could be explained by the strains in the struts inside. Further tests with cubic mesostructures having various dimensions and carried out using X-ray micro-tomography should be performed to investigate these behaviors.

The analyzed paper showed how DIC methods can provide significant insight into the local behavior of lattice materials. It proposed a series of procedures for optimizing the measurement, and to assess their validity, looking to the imaging conditions and surface preparation. Once all the conditions are fulfilled the results are reliable, accurate and reproducible.

The technique was used to compute the mechanical behavior of specimens made of three different families of lattice structures, and provided the actual stress-strain curves, the strain fields and their heterogeneities, the elastic energy release and the individual compression curves for the vertical struts in the cubic specimen.

The actual stress-strain curves can be derived using the DIC data to create a virtual extensometer between the top and bottom of the specimen, and this method is recommended to adequately document the apparent Young's modulus of lattice structures.

The strain fields allow to evaluate heterogeneities in the stress in the specimen even if do not present extensive deformation up to the maximal stress, and the temporal evolution of the strain fields are computable too.

The elastic energy release that occurs across the specimen at failure can be qualitatively documented, but higher precision in the DIC measurements are required to evaluate to what extent this decrease is related to the geometry and main orientation of the struts.

Selecting the appropriate subsets in the images the individual compression curves for the vertical struts in the cubic specimen can be derived, resulting in the discovery that some critical struts are less deformed than the others until they collapse. This shows that the early plastic behavior of the surface struts does not anticipate the failure location, so a statistical approach should be used to assess how the load was carried out inside the structure for this row.

It should also be always remembered that only one observed surface is analyzed, and the statistical significance of this observations over the whole volume must be questioned.

5.4 Plastic deformation behavior of different lattice structures

The paper referenced in [17] illustrate the study of two different lattice structures to investigate their plastic deformation behavior under tension, compression and cyclic testing. The specimens, made of stainless steel AISI 316L/1.4404 for its high corrosion resistance and weldability, exhibited a relative density of 33% compared to bulk samples.

The main focus of the study was on the plastic deformation behavior and the corresponding mechanical properties, especially tensile strength, compression strength, energy absorption and fatigue strength.

Two geometrically distinctly different unit lattice cells were produced. The first was a face-centered cubic lattice cell, called f2cc,z lattice, the second a hollow spherical lattice cell, both with the same relative density. With the term unit cell is identified the smallest group of struts/spheres and nodes that is repeatedly built up to produce lattice structures.

Figure 5.35 shows the CAD illustrations of the structure of the specimens analyzed in the paper, starting from both the unit cells (a, e) and their dimensions and configurations (b, f), to the final specimens obtained merging five unit cells in x,y and z directions (c, g), and lastly their cross sections (d, h).

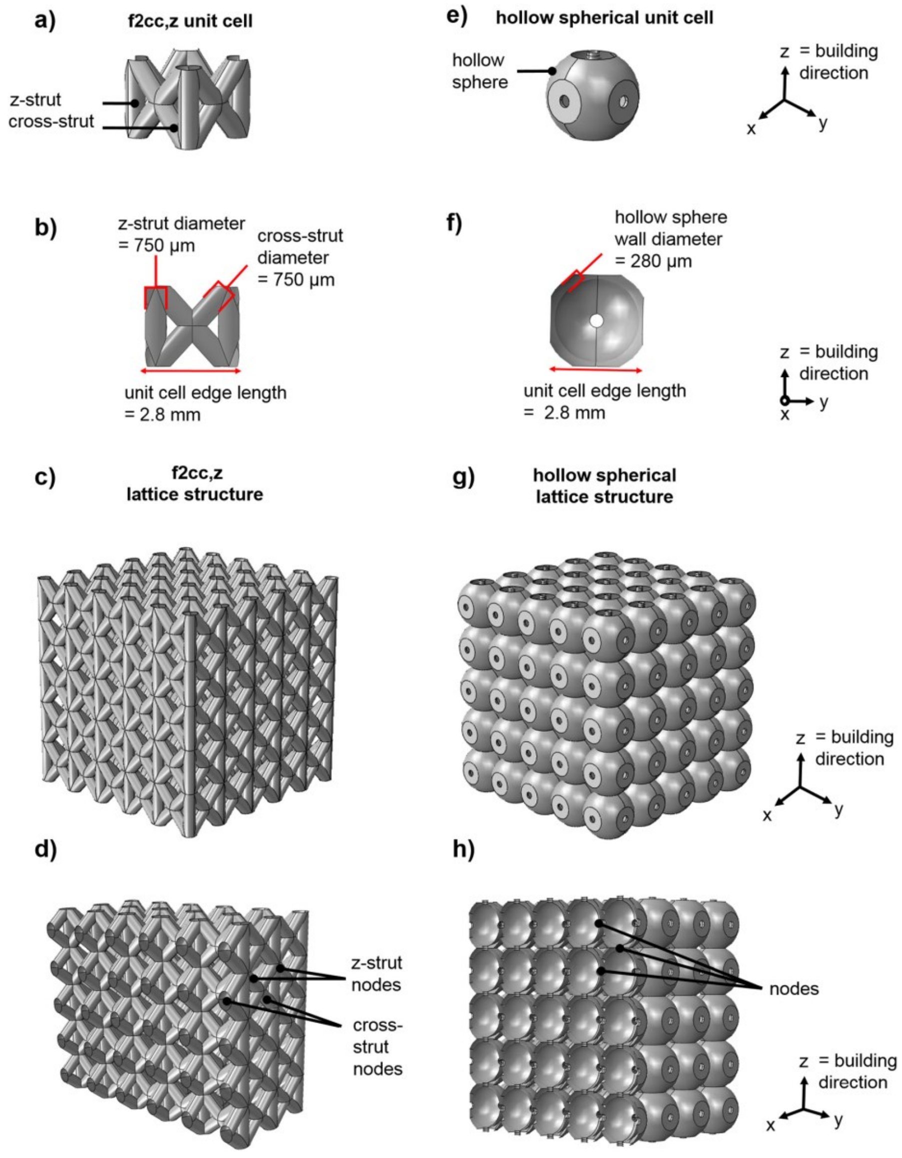

Figure 5.35 CAD illustrations of (a, b) the face-centered cubic f2cc,z unit cell and (e, f) the hollow spherical unit cell with a relative density of 33% referred to fully dense bulk specimens. By merging five unit cells in x-, y- and z-directions, a c) f2cc,z lattice structure and g) a hollow spherical lattice structure for compression testing were created.

The two analyzed unit cells configurations are very dissimilar, so a strongly different deformation behavior is expected in the specimens. To obtain a comprehensive picture of both the influence of the cell configurations as well as the influence of SLM-process inherent characteristics on the defect density, microstructure and element distribution, light scanning electron microscopy (SEM) in combination with energy dispersive X-ray spectrometry (EDS) were used. To obtain the mechanical properties tensile, compression and fatigue tests were carried out, with the tensile testing performed on both the SLM-produced lattice specimens and on the SLM-produced bulk one, and the results were then compared both between them and with the conventionally produced reference specimens.

DIC was used to assess local deformation behavior in compression and tension tests, since the paper reported that at the time in which was wrote no other combined analysis of the local strain distribution of SLM-produced lattice structures in tensile and compression tests had been reported in previous studies. This lack of studies was also found for the comparative analysis of lattice structures and bulk specimens regarding microstructure, defect density, fatigue behavior and energy absorption capacity. The paper aim at the analysis of the plastic deformation behavior of the two lattice structures, by considering geometrical and microstructural aspects.

The reference material for the conventionally produced specimens was hot rolled and solution annealed, while to obtain the prealloyed powder metal the material was first ingot-casted and then atomized using the EIGA-technique, with argon as atomizing medium. The resulting powder had spherical shape with average size of 40 μm, within a range between 25 μm and 50 μm. The overall quality was deemed good, giving that hollow powder particles and significant satellites were not detected.

Both the lattice and bulk specimens were produced using a SLM 280 HL device from SLM Solutions GmbH, equipped with two Yb:YAG-lasers (400 W and 700 W). The optimized processes parameters for the builds were identified studying various previous builds.

To investigate the influence of additional heat treatment on both mechanical properties and microstructure some f2cc,z specimens were annealed at 900 °C for one hour in an air furnace, followed by water quenching.

Figure 5.36 shows the CAD rendering of the specimens, formed by the lattice structures and the screw threads on both sides of the reticular section for the connection to the testing machine.

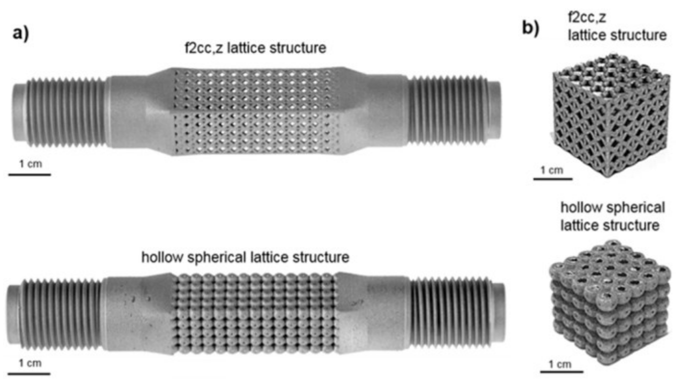

Figure 5.36 a) SLM-produced, cuboid-shaped specimens with drilled screw threads for tensile and fatigue testing. b) SLM-produced cubic specimens.

Some of the macroscopical characteristics, such as elongation and yield and tensile strength of both the bulk and lattice structures specimens were evaluated by uniaxial tensile testing, using a Z100 universal tensile testing machine manufactured by Zwick/Roell, measuring the strain using an optical extensometer called videoXtens produced by the same manufacturer. The same goes with the applied force, determined by a Zwick/Roell load cell.

The elastic modulus, strength and energy absorption were determined by compression tests, performed on a Schenk servo-hydraulic universal mechanical testing machine equipped with a 400 kN load cell, and the lattice structures unconstrained by any face sheets. Both compressive and tensile tests were performed using three bulk and three lattice structure specimens for each loading case.

DIC analysis was performed on the specimens using an Aramis camera system, made by GOM International AG, with Aramis Professional Software as data processor, to investigate the local strain concentrations generated in the lattice structures with respect to nominal compression/tensile strain levels. The nominal strain of the lattice structures was determined by the calculation of the quotient of the traverse path of the lower crosshead of the servo-hydraulic universal mechanical testing machine during the compression test and the initial gauge length. The analyzed pictures were acquired with different parameters and equipment for compression and tensile testing, at 1 Hz using a 6 Megapixel camera with 50 mm and 12 Megapixel camera using a 100 mm lenses respectively. The speckle pattern was sprayed on the surface of the lattice structures before testing.

A fatigue strength and endurance limit test were performed, using a total of 15 specimens per condition (f2cc,z, annealed f2cc,z and hollow spherical lattice structures) for determination of the F-N curves, 5 specimens for force amplitude. Three additional specimens were used for the determination of the endurance limit of the SLM- produced f2cc,z lattice structure.

The specimen's preparation involved mechanical grinding with sand paper followed by mechanical polishing with diamond suspension, to allow the optical detection of material defects and the determination of average density of bulk and lattice structures specimens by image analysis of optical micrographs.

The researchers performed a microstructure analysis, with results coherent with the existing literature.

Using optical microscopy, a density analysis was performed at several cross sections of struts. SLM-produced lattice structures achieved a lower average density than the SLM-produced bulk specimen.

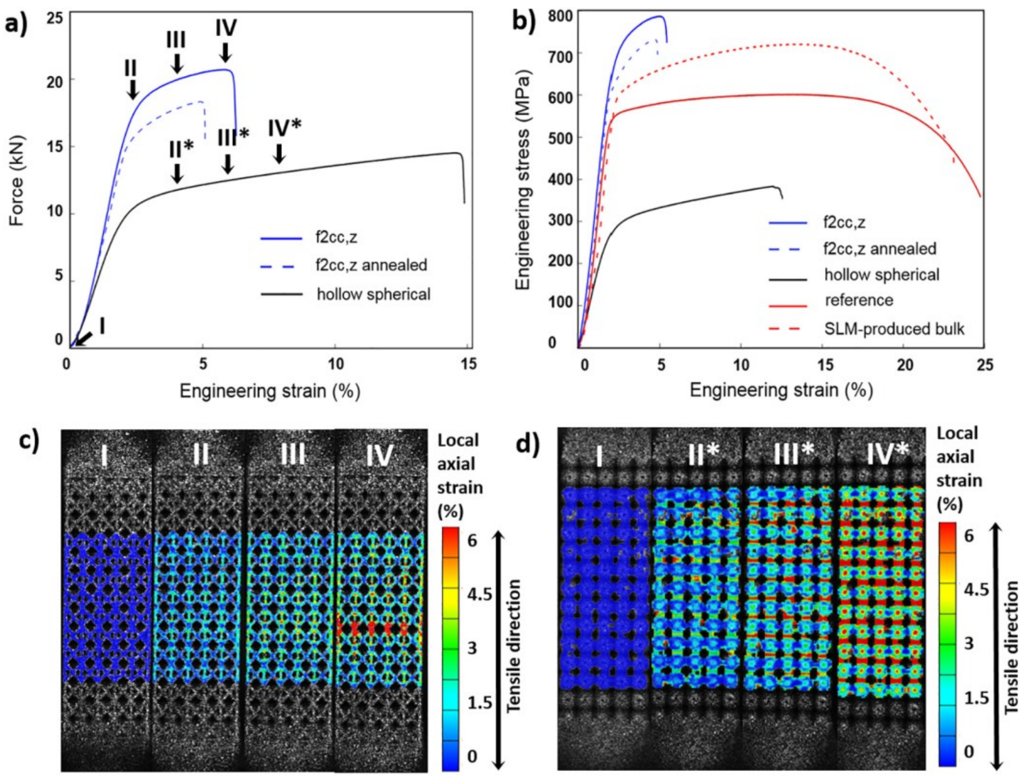

Figure 5.37 Tensile force-engineering strain curves of a) f2cc,z and hollow spherical lattice structures and b) engineering stress-strain curves of lattice structure and bulk specimens. Results of DIC analysis for tensile testing of the c) f2cc,z and d) hollow spherical lattice structures revealing strain localization at the nodes perpendicular to the tensile direction.

In Figure 5.37 a) is pictured a comparison between the three families of specimens. The annealed f2cc,z showed lower maximum force and elongation compared to the non-treated one, while the spherical lattice structure exhibited a lower maximum force and a 150% higher total elongation compared to the other.

The cross-sectional area of the nodes perpendicular to the tensile direction was used for calculation of the engineering stress of the lattice structures, as a result of both DIC analysis, illustrated in Figure 5.37 c) and d), and fractographic analysis, that showed that the samples failed and the highest stresses occurred at the nodes. To complete the illustration of the resulting mechanical properties the stress strain curves of lattice structure and bulk specimens are shown in Figure 5.37 b).

As a result of the analysis, for the f2cc,z specimens axial strain was mainly localized at the z-struts and z-struts nodes, with great intensification detected at one specific plane of z-struts nodes after approximately 3% nominal engineering strain, as visible in Figure 5.37 c), stage III. This localized intensification lead to necking and subsequent fracture at nominal engineering strain of 5.8% (Figure 5.37 c), stage IV).

For the hollow spherical lattice structures no axial strain localization at a specific plane of the lattice structure occurred, as visible in Figure 5.37 d) III* and IV*, but axial strain was localized at the nodes perpendicular to the direction of tensile loading.

Figure 5.37 b) allow to compare the yield strength of the SLM-produced bulk specimen against the traditionally manufactured one (named reference). Whilst the elongation of the f2cc,z lattice structure was significantly reduced compared to the bulk specimens, the ultimate tensile strength was higher.

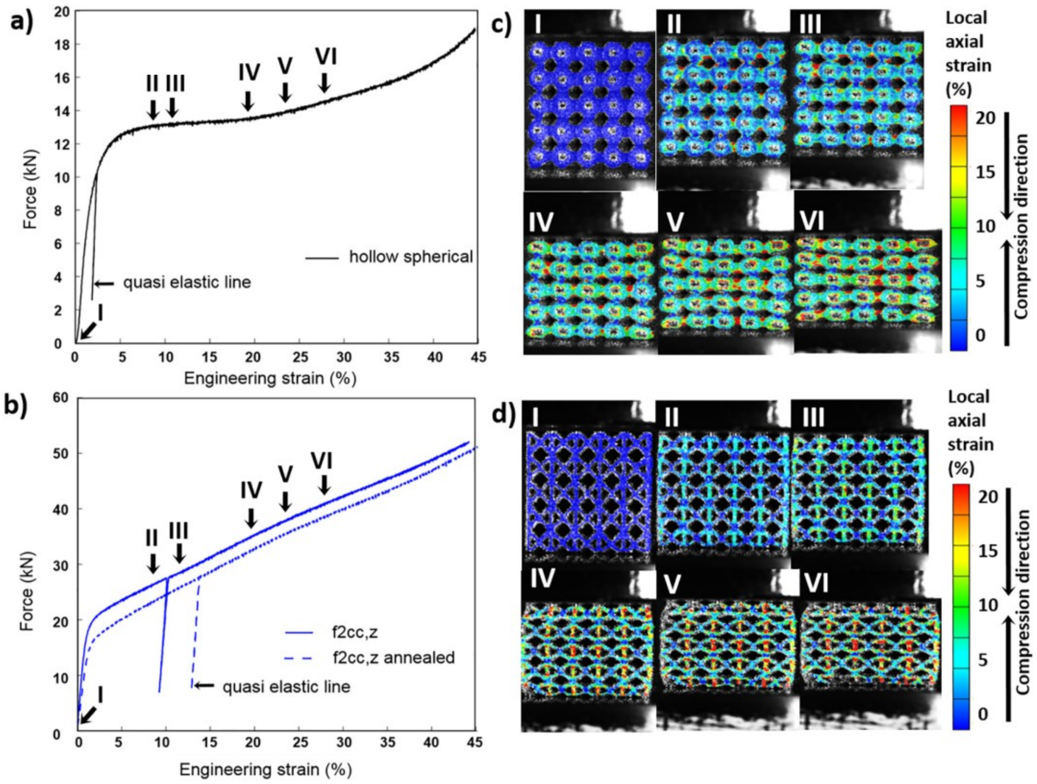

Figure 5.38 Deformation behavior of the specimens. Left images (a, b) show the compression force-engineering strain curves. The local axial strain of the c) hollow spherical and d) SLM-produced f2cc,z lattice structures with increasing nominal compression strains from 0% to 28%.

The hollow spherical and f2cc,z lattice subjects behaviors are illustrated in Figure 5.38. In c) and d) are shown snapshots of the DIC analysis of the specimens subjected to compression strains of 0% to 28%. As visible the f2cc,z lattice specimen shows a steep linear increase of the force-engineering strain curve. The hollow spherical lattice structure shows a plateau between 5% and 20% and slightly increasing slope between 20% and 35%, with a lower yield force and a minimum compression force.

To determine the elastic modulus was calculated the slope of the quasi elastic line of the stress strain curve, following the DIN 50134:2008. The elastic modulus of the SLM-produced f2cc,z lattice structure was about 50% higher compared to the hollow spherical lattice structure. The energy absorption was calculated by integration of the force-strain curve until an engineering strain of 40%. The quotient of energy absorption and weight defines the specific energy absorption (SEA).

Figure 5.39 shows three DIC maps of the local strain distribution after 20% nominal compression strain for the SLM-produced f2cc,z (a), hollow spherical lattice structures (b). The third image (c) shows the behavior of the SLM-produced f2cc,z lattice structures after 30% nominal compression strain.

For the SLM-produced f2cc,z lattice structure, the strain partitioning can be categorized into four zones, marked 1 to 4 in the pictures. The zone number 1 is the most critical, and therefore will be discussed in detail later. Is the zone constituted the z-strut nodes with a deformation higher than 20%. The second zone is placed in the middle of the z struts between two strut nodes with deformation around 15%. The zone number 3 is defined by the cross struts with lower strains (from 5% to 10%). The lowest deformation between 0% and 5% define the fourth zone, the cross strut nodes.

From Figure 5.39 c) shows the local axial strain at the z-strut nodes, calculated in the range of 35% to 50% for a nominal compression strain of 30%. Comparing a) and c) is safe to assume that higher nominal compression strains results in increased localization of axial strains at the z-strut nodes.

For the hollow spherical lattice structure, the strain partitioning can be categorized in three zones. The first zone, with a deformation between 15% and 20%, is constituted by the connection between hollow spheres (nodes) in the x-y plane. The second zone with strains ranging from 5% to 15% is located at the area between nodes in x- and y-direction. The zone number 3, defined by the nodes in z-direction, experienced strains between 0% and 5%.

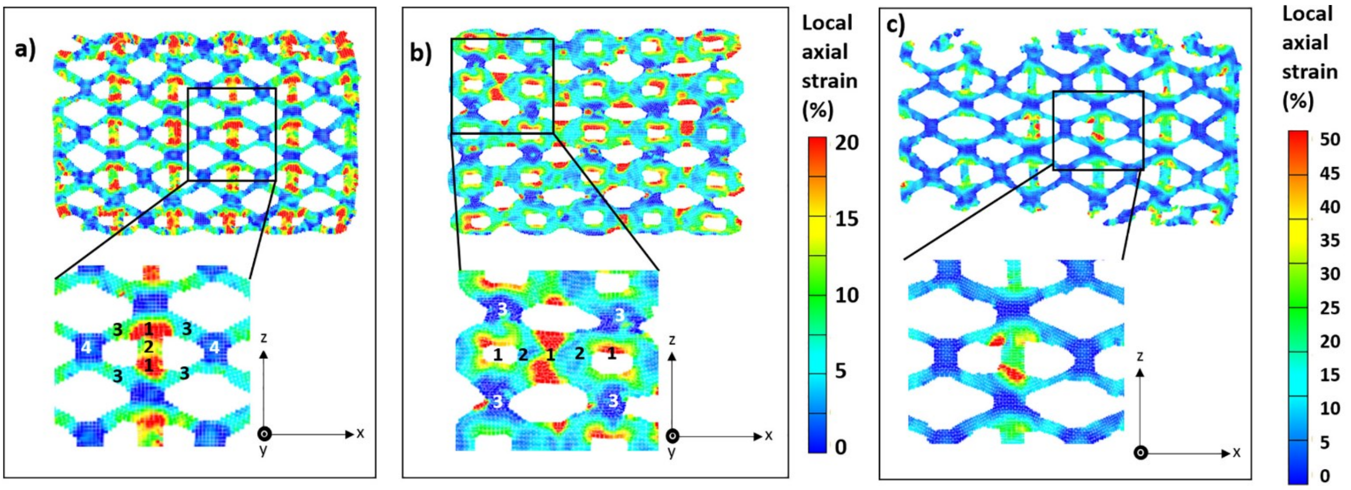

Figure 5.39 DIC maps of the local strain distribution for a) and c) SLM-produced f2cc,z and b) hollow spherical lattice structure revealing the localized strain distribution into different zones. The DIC maps a) and b) show the local strain distribution after 20% and c) after 30% nominal compression strain. Z-axis is parallel to the compression direction.

Mechanical properties of lattice structures

The general deformation behavior of lattice structures during compression testing can be classified into three stages: 1) linear elastic deformation, 2) plastic deformation 3) compacting.

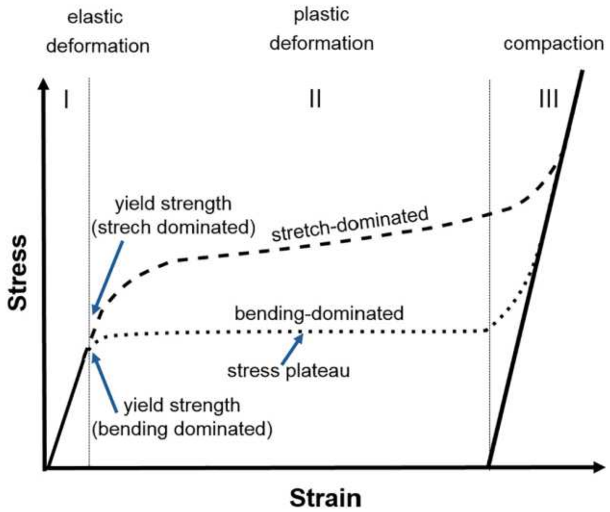

Figure 5.40 Schematic compression stress-strain curves of a bending dominated and a stretch dominated lattice structure, modified from [50].

In Figure 5.40 are schematically illustrated, on a stress-strain diagram, the deformation modes defining the deformation behavior that can happen within the plastic deformation regions. These are either stretch dominated or bending dominated. Comparing the experimental results in Figure 5.38 with the schematic in Figure 5.40 it can be said that the hollow spherical lattice structure deformed bending dominated with a lower yield strength, a stress plateau and therefore a lower specific energy absorption compared to the f2cc,z lattice structures. The presence of the z-struts in the f2cc,z lattice structures was the cause for the stretch dominated deformation behavior. In this lattices configuration with the increase of the load the highest localized deformation were found at the connection between z-struts and cross-struts, in line with Gibson’s deformation model of cellular structures [50], that predict the beginning of plastic deformation of cellular structures with the formation of “plastic hinges”, are defined as areas with localized deformation which are oriented perpendicular to the applied stress. This was clearly visible in the DIC analysis, in which, for a nominal compression of 30%, were measured local axial strains between 35% and 50% at these “plastic hinges”.

The presence of defects, such as pores, was the reason behind the strongly reduced total elongation of the tensile specimens. This caused a geometrically induced stress localization at the z-strut nodes, which was much higher in magnitude during tension than during compression. The defects within the z-strut nodes were closed under compression conditions, and opened during tension. Hence, structure-inherent notch effects at z-strut nodes were further increased due to these defects during tensile testing and caused highly localized stresses in these regions. The stress concentrations due to the porosity and notch effects at z- and cross struts are the cause of a strongly reduced tensile elongation obtained for both lattice structures compared to the bulk specimens.

As previously mentioned, an important application of lattice structures is their energy-absorption capability, knowing that the energy absorption curves of lattice structures are monotonically increasing functions of the relative density [51]. This is in line with the obtained results, as illustrated in Figure 5.41. It should be noted that the f2cc,z lattice structure showed a higher SEA compared to the hollow spherical structure.

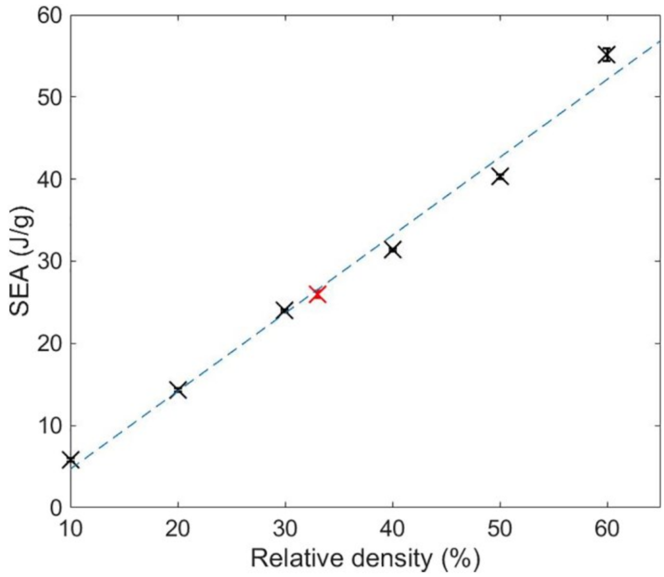

Figure 5.41 SEA of f2cc,z lattice structures after 40% compression with relative densities in the range between 10% and 60%.

Annealing of the 1.4404 f2cc,z lattice structure had no beneficial effect on the tensile and fatigue strength.

The study proved the validity of the use of lattice structures for their high specific energy absorption characteristics, with the f2cc,z structure being superior for static compression-loaded lightweight parts with an energy absorption function compared to the hollow spherical structure. This is also true if compared to the bulk material, since the energy absorption was similar, with the added features derived from its geometrical design, such as vibration damping, acoustic insulation and enhanced thermal isolation. Lattice structures shows their limit working under cyclic loading conditions, because of the resulting low force amplitude during fatigue testing. These characteristics are strongly influenced by the AM production process, with the irregularities created by the melting of powder metal. An optimization of the process parameters is needed, for instance smoother contours and a surface finish at the z-strut nodes will result in better mechanical properties, especially fatigue strength, by reducing notching effects.

5.5 Stiffness prediction model validation

The focus of the paper mentioned in [52] is the study of the behavior of lattice structure specimens under compression fatigue loads. The fatigue properties under compressive loads of three different micro-lattice structures, manufactured from AlSi7Mg powder by SLM process, were analyzed. The specimens were composed of two stretch dominated cells (body-centered and face-centered cubic) and bending dominated cell (cubic structure rotated of 45°).

In doing so the researchers used, among other techniques, DIC to validate a model to evaluate stiffness of lattice structures specimens. Giving the topic of this work only the section related to the model validation and the related informations will be presented.

Monotonic tests in compression on lattice structures were conducted for evaluating the non-uniform stress/strain distribution in the specimen height resulting from a non-perfect contact between the compression plates of the testing machine and the specimen. Since the mechanical properties of micro-lattice structures are affected by several factors, such as process parameters and material characteristics, to study those properties of the bulk material in the same printing condition several monotonic tensile tests have been performed, analyzing specimens manufactured using the same printing parameters used for the lattice microstructures.

To obtain the monotonical mechanical properties three tensile tests were carried out on standard specimens, conducted following the ISO-6892 standard on round specimen, obtained by machining a bar printed using the same set of parameters used for producing the lattice specimens. Giving the usual rectangular sections of the lattice structures, additional tensile monotonic tests were carried out on dog-bone specimens with a rectangular cross-section. To assess the effect of the surface roughness on the monotonic tensile properties these latter were tested in an as-manufactured condition.

The tests were performed on a Deben Microtest machine with a crosshead speed of 0.3 mm/min in displacement control. The longitudinal strain was measured by means of an axial extensometer with a gauge length of 3 mm. The mechanical properties of thin specimens, as regards of yield strength, are different from those of standard specimens, so considering the size of the struts of lattice structures the mechanical properties of small specimens have been used for finite element analysis and for predicting fatigue strength.

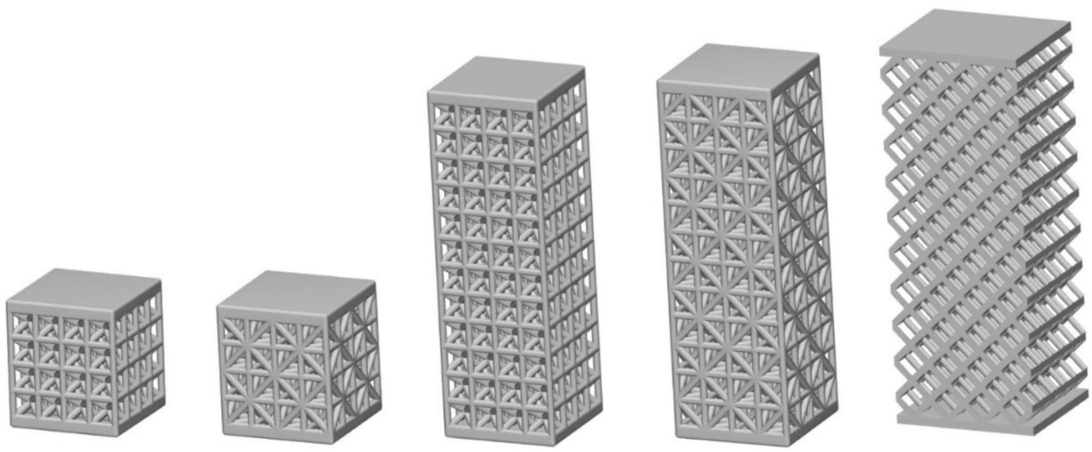

(a) SC-BCC $4 \times 4 \times 4$ (b) SC8-FCC $4\times4\times4$ (c) SC-BCC $4 \times 4 \times 12$ (d) SC8-FCC $4\times4\times12$ (e) SC $4 \times 5 \times 10$

Figure 5.42 Micro-lattice specimens shape and geometry.

The specimens were formed by a combination of Simple Cubic (SC), Body-Centered Cubic (BCC) and Face-Centered Cubic (FCC) lattice structures, composed in three different configurations, one a combined SC-BCC, resulting in a cubic cell with 16 struts, the second one a combined SC8-FCC, a truss formed by combination of octet-truss and cubic truss and the third was based on a SC unit cell made of 12 struts, which was rotated by 45° compared to the horizontal place.

In Figure 5.42 are illustrated some of the specimens configurations, two smaller cubic specimens (4x4x4) with 4 cubic unit cells on each side and higher ones (4x4x12) with 4 unit cells on each side of the cross section and 12 on the height. The SC specimens had 4 cubic cells on one side of the cross section, 5 cubic cells on the other side and 10 unit cells at the height of the specimen. To obtain a better alignment between the compression plates, and to distribute the load uniformly, every specimen has been provided with a thin skin of solid material (0.6 mm).

The samples were manufactured using a Renishaw AM250 SLM system, with a gas atomized AlSi7Mg gas atomized powder, with spherical particle size ranging from 10 μm to 63 μm. The machine is equipped with a single mode fiber laser of maximum power set at 200W with a point distance equal to 75 μm. The exposure time was variable, higher for borders and up skin (140 μs) and lower for other areas (50 μs). The layer thickness was 25 μm. The specimens were rotated inside for the printing process in order to minimize for all the struts the printing angle compared to the vertical direction, obtaining a better quality. This resulted in a rotation of 22.5° compared to the vertical direction for the SC-BCC and SC8-FCC specimens and 45° for the SC specimens.

To calculate the stiffness of the specimens loading/unloading ramps were performed during several static monotonic compression tests. These were run on the Instrom E10000 electrodynamic testing machine, in displacement control with a rate of 0.5 mm/min. Two laser transducers were applied on two opposite sides of the compression plates to measure the displacement during the tests. These displacements were then compared with the displacements measured by the Linear Variable Displacement transducer (LVDT) of the testing machine. The force/displacement graphs of 4x4x4 SC-BCC specimens are illustrated in Figure 5.43, in which is visible a difference between the LVDT and the two laser transducers results. This is due to the stiffness of the testing machine K_m, measured by the LVDT.

The value of K_m was estimated by considering the testing machine and the specimen as a system of two springs in series with a stiffness equal to K_m and K_s respectively. Using the data provided by every specimen ad each loading/unloading ramp the value of the stiffness of the testing machine was calculated as a constant value of approximately 10^5 N/mm. To calculate the displacement of the specimens using the applied force and the displacement provided by the LVDT the following formula can be used

$$\delta_S = \delta_{LVDT} - \frac{F}{K_m}$$

The curves illustrating the results are represented in Figure 5.43.

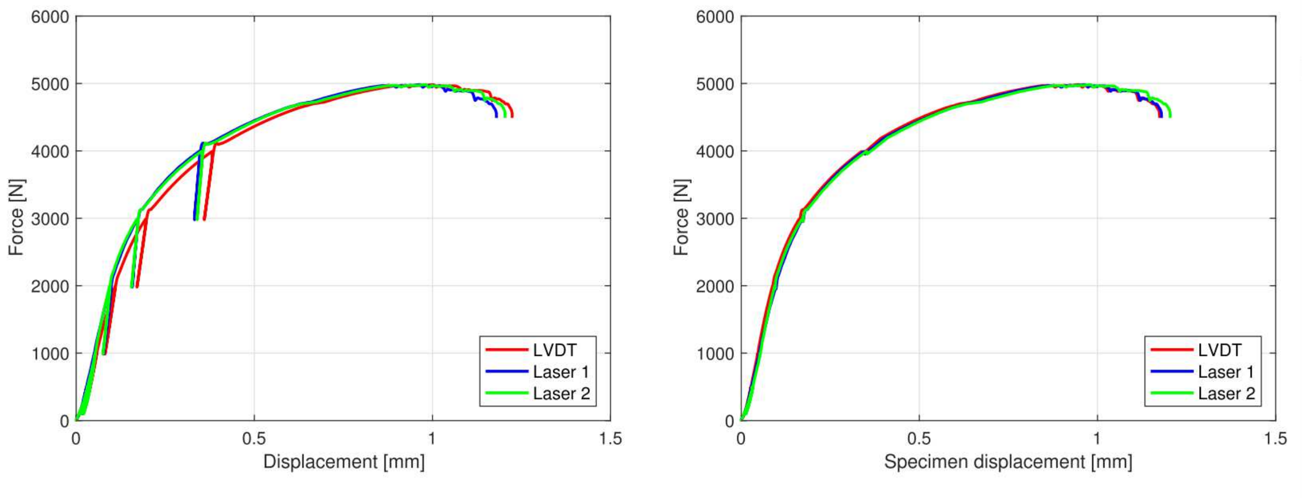

(a) (b)

Figure 5.43 Monotonic test on SC-BCC1 (4x4x4) specimen. (a) Force-displacement curve obtained with different transducers: LVDT and laser transducers. (b) Force displacement curve obtained considering the stiffness of the testing machine.

To evaluate the changes in the specimen stiffness as a function of the applied force the loading/unloading ramps in the monotonic compression tests were used. The results showed that the total specimen stiffness K_s is not constant but it increases with the load level were the loading/unloading ramps have been performed. In addition, the ratio *a* between the stiffness of a 4x4x12 and a 4x4x4 specimen is different from the theoretical value of 1/3, which is achieved only in the last loading/unloading ramp at the maximum load level. The cause of this behavior may be due to the presence of a non-linear region in the curve. This region is caused by the specimen adapting its irregular shape to the compression plates of the testing machine, at lower load levels, and this behavior have more relative weight in the 4x4x4 specimen, as visible in the curves pictured in Figure 5.44

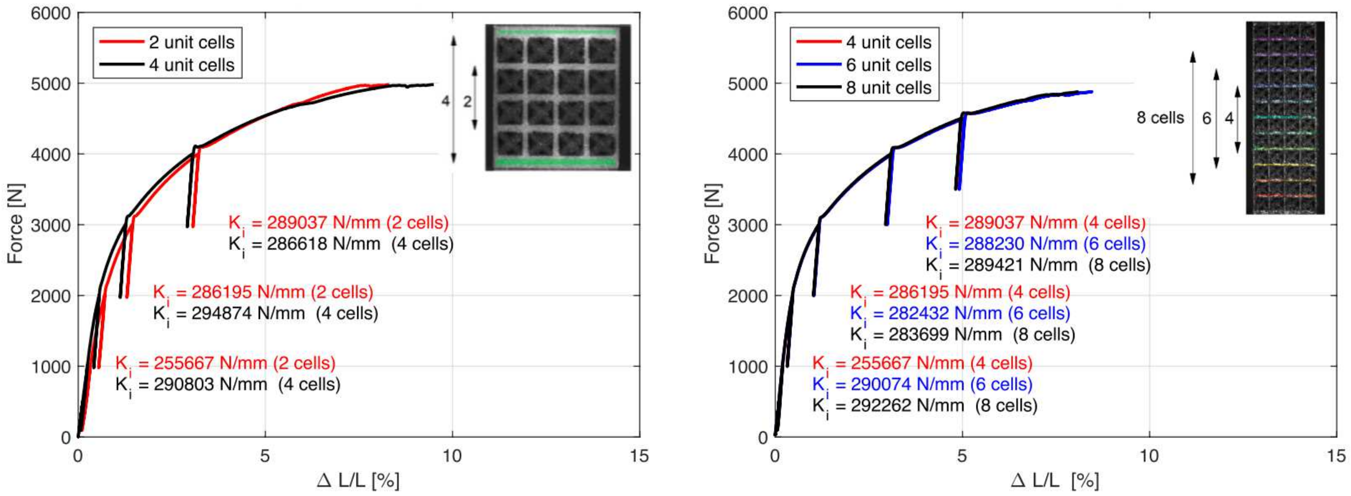

(a) SC-BCC1 4 × 4 × 4 specimen (b) SC-BCC7 4 × 4 × 12 specimen

Figure 5.44 Evaluation of stiffness by means of DIC.

To obtain reliable results this effect of contact must be described and accounted for. To do so a model based on springs in series can be adopted, with the main hypothesis being that the central part of the specimen has the same stiffness regardless of the number of cells along the height.

The following two equations describe the total specimen stiffness, as evaluated by the slope of the force-LVDT displacement curve:

$$\frac{1}{K_{s(4)}} = \frac{2}{K_c} + \frac{2}{K_i}$$

$$\frac{1}{K_{s(12)}} = \frac{2}{K_c} + \frac{10}{K_i}$$

With $K_{s(4)}$ and $K_{s(12)}$ the total stiffness of the 4x4x4 specimen and the 4x4x12 specimen respectively.

For both structures the stiffness K_c for both the the first and last row of cubic cells, the ones closer to the outside skin, have been assumed as equal between them, and different from the value K_i of the generic row in the central area.

Solving the system of the above-mentioned equations is possible to obtain the value of stiffness K_i as:

$$K_i = \frac{8K_{s(12)}}{1-a} = \frac{8aK_{s(4)}}{1-a}$$

Using the experimental stiffness ratio, the real stiffness in the central part of the specimen can be obtained independently from the applied load level.

This model has been validated using a full-field DIC analysis performed on some of the specimens.

The speckle pattern was applied using an airbrush, with no additional specimen preparation, to guarantee the original micro-lattice geometry as obtained from the AM process.

The setup consisted in a set of Optem lens mounted on a tripod and three linear manual precision linear stages for accurate positioning. An ALLI Manta camera was used to acquire the images at a resolution of 1624 x 1624 pixel and a frame rate of 30 fps. A laptop computer equipped with a LabView software integrating the frame acquisition process and the signals record from the load frame (load and displacement) was connected to the DIC system. The use of that specific lens system allowed to adopt different visual fields depending on the size of the specimen under investigation. The visual field for the rectangular microlattices was approximately 30 mm x 23 mm, resulting in a resolution of 18.5 μm/px, while the basic cubic cells with a visual field of approximately 12 mm x 15.4 mm resulted in a resolution of 9.5 μm/px.

After the test every frame of the video was correlated with the refence image, captured before application of the load. The correlation was performed using the VIC-2D software selecting only the regions of the micro-lattices. The strains were calculated by positioning virtual extensometers at specific cell positions, while the DIC measurements were performed targeting only the displacement measurements, giving that the speckle pattern was deposited on the as-manufactured geometry.

Following this procedures DIC allowed to obtain and measure local cell elastic modulus and bulk micro-lattice elastic modulus. Using the elastic modulus, it was made possible also to determine the value of the K_i stiffness in each row of cubic cells in the micro-structures considering the displacements of each points in of the target surface.

These observations allowed to validate the above introduced "spring in series" model, since the results showed that the inner rows of cubic cells in the specimens are uniformly loaded and have the same stiffness K_i. DIC analysis resulted in a mean value of K_i of 2.8-2.9 x 10^5 N/mm, close to the values resulted from the analytical model showed in Figure 5.43, which gave a value of K_i placed between 2.75 x 10^5 N/mm and 2.85 x 10^5 N/mm.

6 Results

The aim of this paper is to study the application of Digital Image Correlation techniques on metallic lattice components produced using powder bed fusion metal additive manufacturing technologies.

These components, especially if their struts are small in size, are characterized by having a real geometry being very different from the ideal one, because of the inherent limits of the powder bed fusion processes. Traditional monitoring techniques are limited to the study of the macroscopic behavior of the components. The DIC has therefore proved to be an extremely effective tool for the study of these components, precisely because of its characteristic of being a full-field method, allowing knowledge of the behavior of the specimen along its entire height.

The main results of the analysis are illustrated below:

- DIC has proven to be an appreciated and widely used method for the study of lattice components.
- It allows to obtain information on both the behavior of the entire component as well as of the single strut, a crucial feature since, as seen, different structural configurations can lead to failures of dramatically different nature. Strain variability over the specimen are consequently quantifiable and their location identifiable.
- The data collected using DIC methods agree, qualitatively and quantitatively, with those collected by different measurement methods.
- If the data acquisition and setup procedures are planned and executed correctly DIC allows to obtain results with measurement uncertainties less than or comparable to those inherent of the test conditions. In some cases, it can provide more reliable results compared to traditional measurements, allowing to eliminate the influence of some boundary conditions.
- Several precautions must be taken to ensure precise results to be obtained. For lattice structures specimens of small dimensions however, the out-of-plane error typical of 2-D DIC due to deformation of the specimen itself is usually negligible. Uncertainties should be assessed for every setup and test configuration.
- DIC is considered a reliable technique, to the point of being used for the validation of FE models. Given the limitations imposed by the processing ability of workstations, the DIC can provide more precise results than the FE models.

The application of 2-D DIC is limited by the nature of the method, since the analysis is performed only on the surface of the specimen.

List of figures

References

[1] C. Yan, L. Hao, A. Hussein e D. Raymont, «Evaluations of cellular lattice structures manufactured using selective laser melting,» *International Journal of Machine Tools & Manufacture,* vol. 62, n. 6, pp. 32-38, 2012.

[2] S. H. Huang, P. Liu, A. Mokasdar e L. Hou, «Additive manufacturing and its societal impact: a literature review,» *The International Journal of Advanced Manufacturing Technology,* vol. 67, n. 10, pp. 1191-1203, 2013.

[3] A. R. Catalano, V. Lunetto, P. Priarone e L. Settineri, «A Survey on Energy Efficiency in Metal Wire Deposition Processes,» in *International Conference on Sustainable Design and Manufacturing*, Budapest, 2019.

[4] D. Sher, «Italian hospital saves Covid-19 patients lives by 3D printing valves for reanimation devices,» 3D Printing Media Network - 3dpbm, 14 March 2020. [Online]. Available: https://www.3dprintingmedia.network/covid-19-3d-printed-valve-for-reanimation-device/. [Consultato il giorno 16 March 2020].

[5] C. Fracassi, «Valvole per respiratori stampate 3d,» 14 Marzo 2020. [Online]. Available: https://www.facebook.com/photo.php?fbid=10222328772076302&set=a.1280709025953&type=3&theater. [Consultato il giorno 16 Marzo 2020].

[6] M. Temporelli, «Valvole per respiratori stampate 3d - Prima serie,» 13 Marzo 2020. [Online]. Available: https://www.facebook.com/massimo.temporelli/posts/10219716100146800. [Consultato il giorno 16 Marzo 2020].

[7] T. S. Douglas e G. W. Stanley, «Costs and Cost Effectiveness of Additive Manufacturing: A Literature Review and Discussion,» National Institute of Standards and Technology, 2014.

[8] B. Esmaeilian, S. Behdad e B. Wang, «The evolution and future of manufacturing: A review,» *Journal of Manufacturing Systems,* vol. 36, n. 4, pp. 79-100, 2016.

[9] T. D. Ngo, A. Kashani, G. Imbalzano, K. T. Nguyen e D. Hui, «Additive manufacturing (3D printing): A review of materials, methods, applications and challenges,» *Composites Part B: Engineering,* vol. 143, n. 6, pp. 172-196, 2018.

[10] European Space Agency, «3D-printed thrust chamber passes first tests for Vega evolutions,» European Space Agency, 03 March 2020. [Online]. Available: https://www.esa.int/Enabling_Support/Space_Transportation/3D-printed_thrust_chamber_passes_first_tests_for_Vega_evolutions. [Consultato il giorno 10 March 2020].

[11] Avio S.P.A., «First full scale M10 engine thrust chamber test firing successfully completed,» 03 March 2020. [Online]. Available: https://www.avio.com/news-events/first-full-scale-m10-engine-test-firing-successfully-completed. [Consultato il giorno 14 March 2020].

[12] T. R. Walter, «Structural architecture of the 1980 Mount St. Helens collapse: An analysis of the Rosenquist photo sequence using digital image correlation,» *Geology,* vol. 39, n. 8, p. 767–770., 2011.

[13] T. D. Ngo, A. Kashani, G. Imbalzano, K. T. Nguyen e D. Hui, «Additive manufacturing (3D printing): A review of materials, methods, applications and challenges,» *Composites Part B: Engineeering,* vol. 143, n. 06, pp. 172-196, 2018.

[14] I. Gibson, D. Rosen e B. Stucker, Additive Manufacturing Technologies, New York: Springer-Verlag New York, 2015.

[15] M. Burns, Automated fabrication : improving productivity in manufacturing, Englewood Cliffs, N.J: PTR Prentice Hall, 1993.

[16] T. T. Wohlers, «Wohlers report 2009: rapid prototyping & tooling state of the industry.,» Wohlers Associates, Detroit, 2009.

[17] P. Köhnen, C. Haase, J. Bültmann, S. Ziegler, J. H. Schleifenbaum e W. Bleck, «Mechanical properties and deformation behavior of additively manufactured lattice structures of stainless steel,» *Materials & Design,* vol. 145, n. 5, pp. 205-217, 2018.

[18] J.-P. Kruth, P. Mercelis, J. Van Vaerenbergh, L. Froyen e M. Rombouts, «Binding mechanisms in selective laser sintering and selective laser melting,» *Rapid Prototyping Journal,* vol. 11, n. 1, pp. 26-36, 2005.

[19] Y. Yongnian, Z. Renji, L. Qingping e D. Zhaohui, «Study on multifunctional rapid prototyping manufacturing system,» *Integrated Manufacturing Systems,* vol. 9, pp. 236-241, 1998.

[20] D. Larcombe, «Fiber versus CO2 laser cutting,» *Industrial Laser Solutions* , Novembre 2013.

[21] D. Chauveau, «Review of NDT and process monitoring techniques usable to produce high-quality parts by welding or additive manufacturing,» *Welding in the world,* vol. 62, n. 5, pp. 1097-1118, Settembre 2018.

[22] The American Society for Nondestructive Testing, «Introduction to Nondestructive Testing,» The American Society for Nondestructive Testing, 2019. [Online]. Available: https://www.asnt.org/MinorSiteSections/AboutASNT/Intro-to-NDT. [Consultato il giorno 12 Luglio 2019].

[23] S. K. Dwivedi, M. Vishwakarma e A. Soni, «Advances and Researches on Non Destructive Testing: A Review,» *Materials Today: Proceedings 5 (2018) 3690–3698,* n. 5, pp. 3690-3698, 2018.

[24] J. Waller, «Nondestructive Evaluation of Additive Manufacturing State-of-the-Discipline Report,» NASA, 2014.

[25] H. Rieder, A. Dillhöfer, M. Spies, J. Bamberg e T. Hess, «Online Monitoring of Additive Manufacturing Processes Using Ultrasound,» in *11th European Conference on Non-Destructive Testing (ECNDT 2014)*, Prague, Czech Republic, 2014.

[26] M. A. Sutton, J.-J. Orteu e H. W. Schreier, Image correlation for shape, motion and deformation measurements, New York: Springer, 2009.

[27] I. D. I. C. S. E. Jones e M. Iadicola, «A Good Practices Guide for Digital Image Correlation.,» International Digital Image Correlation Society, 2018.

[28] M. Aydin, X. Wu, K. Cetinkaya, M. Yasar e I. Kadi, «Application of Digital Image Correlation technique to Erichsen Cupping,» *Engineering Science and Technology, an International Journal,* vol. 21, pp. 760-768, 2018.

[29] B. Pan, K. Qian, H. Xie e A. Asundi, «Two-dimensional digital image correlation for in-plane displacement and strain measurement: a review,» *Measurement science and technology,* vol. 20, n. 6, 2009.

[30] W. LePage, «A practical Guide to DIC,» [Online]. Available: https://digitalimagecorrelation.org/.

[31] Creative Commons, «Attribution 4.0 International (CC BY 4.0),» [Online]. Available: https://creativecommons.org/licenses/by/4.0/. [Consultato il giorno 16 02 2020].

[32] J. Stinville, M. Echlin e D. Texier, «Sub-Grain Scale Digital Image Correlation by Electron Microscopy for Polycrystalline Materials during Elastic and Plastic Deformation,» *Experimental Mechanics,* vol. 56, n. 2, pp. 197-216, 2016.

[33] M. Sutton, J. Yan, V. Tiwan, H. Schreier e J. Orteu, «The effect of out-of-plane motion on 2D and 3D digital image correlation measurements,» *Optics and Lasers in Engineering,* vol. 46, n. 10, pp. 746-757, 2008.

[34] P. L. Reu, «All about Speckles: Aliasing,» *Experimental Techniques,* vol. 38, n. 5, 2014.

[35] P. L. Reu, «All about speckles: Speckle Size Measurement,» *Experimental Techniques,* vol. 38, n. 6, 2014.

[36] P. Reu, «All about Speckles: Edge Sharpness,» *Experimental Techniques,* vol. 39, n. 2, 2015.

[37] W. S. LePage, J. A. Shaw e S. H. Daly, «Optimum Paint Sequence for Speckle Patterns in Digital Image Correlation,» *Experimental Techniques,* vol. 41, n. 5, pp. 557-563, 2017.

[38] P. L. Rieu, «Points on Paint,» *Experimental Techniques,* vol. 39, n. 4, 2015.

[39] K. N. Jonnalagadda, I. Chasiotis e S. Yagnamurty, «Experimental Investigation of Strain Rate Dependence of Nanocrystalline Pt Films,» *Experimental Mechanics,* vol. 50, pp. 25-35, 2010.

[40] A. H. Cannon, J. D. Hochhalter, G. F. Bomarito e T. Ruggles, «Micro Speckle Stamping: High Contrast, No Basecoat, Repeatable, Well-Adhered,» in *Conference Proceedings of the Society for Experimental Mechanics Series*, 2017.

[41] E. M. Jones e P. L. Reu, «Distortion of Digital Image Correlation (DIC) Displacements and Strains from Heat Waves,» *Experimental Mechanics,* vol. 58, p. 1133–1156, 2018.

[42] W. S. LePage, S. H. Daly e J. A. Shaw, «Cross Polarization for Improved Digital Image Correlation,» *Experimental Mechanics,* vol. 56, p. 969–985, 2016.

[43] B. Pan, «Thermal error analysis and compensation for digital image/volume correlation,» *Optics and Lasers in Engineering,* vol. 101, pp. 1-15, 2018.

[44] P. L. Reu, «A Realistic Error Budget for Two Dimension Digital Image Correlation,» in *Conference Proceedings of the Society for Experimental Mechanics Series*, Costa Mesa, CA, 2016.

[45] M. E. Lynch, M. Mordasky, L. Cheng e A. To, «Design, testing, and mechanical behavior of additively manufactured casing with optimized lattice structure,» *Additive Manufacturing,* pp. 462-471, 2018.

[46] L. Boniotti, S. Beretta, S. Foletti e L. Patriarca, «Strain concentrations in BCC micro lattices obtained by AM,» *Procedia Structural Integrity,* pp. 166-173, 2017.

[47] N. Vanderesse, A. Richter, N. Nuño e P. Bocher, «Measurement of deformation heterogeneities in additive manufactured lattice materials by Digital Image Correlation: Strain maps analysis and reliability assessment,» *Journal of the Mechanical Behavior of Biomedical Materials,* vol. 86, n. 10, pp. 397-408, 2018.

[48] N. Vanderesse, M. Lagacé, F. Bridier e P. Bocher, «An Open Source Software for the Measurement of Deformation Fields by Means of Digital Image Correlation.,» in *Microscopy and Microanalysis*, Indianapolis, IN, USA, 2013.

[49] J. Schindelin, I. Arganda-Carreras e E. Frise, «Fiji: an open-source platform for biological-image analysis.,» *Nature Methods,* vol. 9, n. 7, pp. 676-682, 2012.

[50] L. J. Gibson e M. F. Ashby, Cellular Solids: Structure and Properties, Cambridge: Cambridge University Press, 1999.

[51] T. Tancogne-Dejean, A. B. Spierings e D. Mohr, «Additively-manufactured metallic micro-lattice materials for high specific energy absorption under static and dynamic loading,» *Act Materialia,* vol. 116, n. 09, pp. 14-28, 2016.

[52] L. Boniotti, S. Beretta, L. Patriarca e S. Foletti, «Experimental and numerical investigation on compressive fatigue strength of lattice structures of AlSi7Mg manufactured by SLM,» *International Journal of Fatigue,* vol. 128, n. 09, 2019.

[53] W. Boyes, Instrumentation Reference Book, 4 a cura di, W. Boyes, A cura di, Elsevier Science & Technology, 2010, pp. 567-592.